



**UNIVERSITAT POLITÈCNICA
DE CATALUNYA
BARCELONATECH**

DEPARTMENT OF ELECTRICAL ENGINEERING

PH.D. IN ELECTRICAL ENGINEERING

PH.D. THESIS

**Development of a VHF broadband interferometer
to investigate unsolved lightning phenomena:
high-energy radiation from lightning strikes and
multi-stroke positive cloud-to-ground flashes**

SUPERVISOR:

PROF. JOAN MONTANYÀ

CANDIDATE:

MICHELE URBANI

CO-SUPERVISOR:

DR. OSCAR VAN DER VELDE

BARCELONA, SEPTEMBER 2022



**UNIVERSITAT POLITÈCNICA
DE CATALUNYA
BARCELONATECH**

DEPARTMENT OF ELECTRICAL ENGINEERING

PH.D. IN ELECTRICAL ENGINEERING

PH.D. THESIS

**Development of a VHF broadband interferometer
to investigate unsolved lightning phenomena:
high-energy radiation from lightning strikes and
multi-stroke positive cloud-to-ground flashes**

THESIS BY COMPENDIUM OF PUBLICATIONS

SUPERVISOR:

PROF. JOAN MONTANYÀ

CO-SUPERVISOR:

DR. OSCAR VAN DER VELDE

CANDIDATE:

MICHELE URBANI

Barcelona, September 2022

To my Family

“L’amor che move il sole e l’altre stelle”

Dante, Paradiso XXXIII

Contents

| | |
|---|-----------|
| List of Figures | 1 |
| <i>Abstract</i> | i |
| <i>Resumen</i> | i |
| <i>Acronyms</i> | i |
| 1 Introduction | 1 |
| 1.1 Relevance and motivation | 1 |
| 1.2 Objectives | 3 |
| 1.3 Thesis structure. | 4 |
| 2 State of the art | 5 |
| 2.1 Lightning interferometry | 5 |
| 2.1.1 VHF lightning mapping | 6 |
| 2.1.2 Basics of VHF lightning interferometry | 6 |
| 2.1.3 VHF Broadband Interferometry | 8 |
| 2.1.4 Generalized cross-correlation technique | 10 |
| 2.1.5 Comparison between a Lightning Mapping Array and a VHF Broadband Interferometer | 11 |
| 2.2 High-energy radiation from thunderstorms | 13 |
| 2.2.1 Terrestrial Gamma-ray Flashes | 14 |
| 2.2.2 Space observations | 14 |
| 2.2.3 Ground-based observations | 15 |
| 2.2.4 Review of high-energy radiation mechanisms | 18 |
| 3 Urbani et al. (2021): High-energy radiation from natural lightning observed in coincidence with a VHF Broadband Interferometer . . | 21 |
| 3.1 Abstract | 21 |
| 3.2 Plain Language Summary | 22 |

| | | |
|----------|---|-----------|
| 3.3 | Introduction | 22 |
| 3.4 | Instrumentation and Methodology | 24 |
| 3.4.1 | VHF Broadband Interferometry System | 25 |
| 3.4.2 | High-energy detector | 28 |
| 3.4.3 | LINET | 29 |
| 3.5 | Observations and Analysis | 29 |
| 3.5.1 | Overall data analysis | 29 |
| 3.5.2 | Negative Downward Leaders: 2019-11-11 06:39:06 | 32 |
| 3.5.3 | Dart Leader: 2019-11-11 06:39:06 | 42 |
| 3.5.4 | Negative Downward Leaders: 2019-11-11 06:38:16 | 44 |
| 3.6 | Discussion | 46 |
| 3.6.1 | Implications on the origin of the most intense VHF pulses | 48 |
| 3.6.2 | Implications on the origin of the high-energy radiation | 49 |
| 3.6.3 | Implications on the origin of the TGFs | 50 |
| 3.7 | Conclusions | 51 |
| 4 | Urbani et al.(2022): Multi-stroke positive cloud-to-ground lightning sharing the same channel observed with a VHF Broadband Interferometer | 53 |
| 4.1 | Abstract | 53 |
| 4.2 | Plain Language Summary | 54 |
| 4.3 | Introduction | 54 |
| 4.4 | Instrumentation and Methodology | 55 |
| 4.4.1 | VHF Broadband Interferometer | 55 |
| 4.4.2 | Colombia Lightning Mapping Array | 56 |
| 4.4.3 | Quasi-3D conversion | 56 |
| 4.5 | Observations and Analysis | 56 |
| 4.5.1 | Multi-stroke +CG flash: 2019-10-27 11:15:06 | 56 |
| 4.5.2 | Initiation of the subsequent positive leader along the previous channel | 60 |
| 4.5.3 | Comparison between the first positive stroke and the subsequent stroke. | 63 |
| 4.6 | Discussion | 65 |
| 5 | Conclusions and future perspective | 67 |
| 5.1 | Future perspectives | 69 |
| | Appendices | 71 |
| A | Urbani et al (2021): Supporting Information | 73 |
| A.1 | Table of Event: 2019-11-11 06:39:06 | 74 |

| | | |
|----------|---|------------|
| A.2 | Description of the algorithm to compute t_0 | 75 |
| A.3 | Imaging efficiency | 76 |
| A.4 | Temporal correspondence between high-energy emissions and most intense VHF pulses | 79 |
| A.5 | X-ray and gamma-ray spectrum | 84 |
| B | Urbani et al (2022): Supporting Information | 85 |
| B.1 | Charge structure | 86 |
| B.2 | Angular resolution of the VHF broadband interferometer | 88 |
| B.3 | First DPL spatial and temporal origin in flash 2019-10-27 11:15:06 (UTC). | 89 |
| B.4 | Spectral power density of the two DPLs | 91 |
| B.5 | Analysis of the first downward positive leader propagation in VHF radio band | 92 |
| B.6 | Quasi-3D conversion | 95 |
| B.7 | Initiation of the second DPL along a previous channel to ground, flash (1) | 96 |
| | Bibliography. | 99 |
| | <i>Acknowledgments</i> | <i>111</i> |

List of Figures

| | | |
|-----|---|----|
| 1.1 | Sketch of the measurement technique. The lightning leader propagation is mapped by the VHF broadband Interferometer (INTF) and simultaneously the X-ray emissions are detect by the high-energy detector. (Image not in scale) | 2 |
| 2.1 | A) Phase delay due to geometry. B) Coordinate system for three antennas. C) The $\cos\alpha$ vs $\cos\beta$ plane. (Figure adapted from Stock, 2014) | 7 |
| 2.2 | Phase ambiguity problem: the same phase difference $\Delta\phi$ measured by the two antennas corresponds to different θ_j . Therefore for a monochromatic wave ω we have an ambiguous location of the source. | 8 |
| 2.3 | Conceptualization of the broadband strategy (real data). The phase ambiguity is solved by the contribution of multi-narrowband frequencies. The correct unambiguous broadband solution in red color, the multi-narrowband frequencies solutions in black color. The arrow shows the combined solution. | 9 |
| 2.4 | Quasi-3D conversion of the INTF data and superposition of the LMA sources over the INTF data. | 12 |
| 2.5 | Geographic distribution of all TGFs detected by BATSE (yellow), RHESSI (green), AGILE (red) and Fermi (blue). (Figure from URSI et al. 2017) | 15 |
| 2.6 | <i>Left:</i> X-rays from NaT-PMT detectors (top panel) and electric field waveforms (bottom panel) for a natural cloud-to-ground lightning flash at the ICLRT. As can be seen the x-ray pulses are closely associated with the step leader formation. Dwyer et al. (2005) <i>Right:</i> Simultaneous measurements of a X-ray emission and microwave RF power peak in a negative return stroke -25 kA (t=388 ms). Montanyà et al. (2014) | 16 |

| | | |
|-----|---|----|
| 2.7 | a) The Telescope Array in Utah (USA) b) An example of a downward TGF detected from the TA in Utah. (Figure from Belz et al. 2020) | 17 |
| 2.8 | The effective frictional force experienced by a free electron (or positron) moving through air at STP as a function of kinetic energy. (Figure from Dwyer, Smith & Cummer 2012) | 18 |
| 2.9 | Schematic Comparison between the Wilson's runaway electron mechanism, the RREA mechanism, and the relativistic feedback mechanism. (Figure from Dwyer, Smith & Cummer 2012) | 20 |
| 3.1 | a) Instrumentation deployment on the UIS roof in Barrancabermeja (Colombia). Two lightning interferometers (INTF), a flat plate antenna for E-field measurements and an X-ray detector. b) Conceptual scheme and basic geometry of the lightning interferometer. A single interferometer provides a 2D imaging of the lightning in angular coordinates: elevation and azimuth. | 25 |
| 3.2 | The map shows the LINET lightning location recorded during the observational campaign at the Universidad Industrial de Santander (UIS) campus of Barrancabermeja (Colombia) in autumn 2019. The map is centered in the INTF location. Lightning events observed by the INTF in coincidence with an X-ray burst were colored in blue, lightning events observed by the INTF without X-ray detection were colored in red, lightning events not recorded were colored in gray. | 30 |
| 3.3 | a) Energy distribution of the X-ray detected during the bursts observed. The highest energy values can be real or overestimated due to a pile-up effect. The nominal time resolution to excluding pile-up is $0.5 \mu s$. b) Time distribution of the X-ray pulses detected during the bursts observed in negative downward leaders before the return stroke. | 32 |
| 3.4 | Negative downward leader associated with the detection of an X-ray burst. The lightning map is obtained with the VHF broadband lightning interferometer INTF-1. The image is colored by time and the most likely locations of the X-ray sources is marked with black stars. The gray image is related to another simultaneous leader branch likely farther away from the interferometer. | 33 |
| 3.5 | Negative downward leader associated with the detection of an X-ray burst. The lightning map is obtained with the VHF broadband lightning interferometer INTF-1. The image is colored by time and the most likely location of the X-ray sources is marked with black stars. | 34 |

| | | |
|------|--|----|
| 3.6 | a) Electric field from the flat plate antenna and high-energy detector signal in the last 1 ms before the return stroke. b) VHF sources and VHF pulses amplitude in the last 3 ms before the return stroke. The red line and the blue line represent the VHF pulses median and the third quartile respectively, which define the most intense VHF pulses. | 35 |
| 3.7 | a) Density plot of all the VHF sources that can be related to the high-energy emission in a time interval δt of $\pm 1 \mu s$ with respect to all X-ray t_0 . b) Unique location of X-ray pulse 18. c) Ambiguous location of X-ray pulse 19. | 36 |
| 3.8 | Zoom of the most interesting time interval of Event 2019-11-11 06:39:06. The graph highlights the temporal correspondence between the X-ray pulses (blue lines and labels) and the most intense VHF pulses. The association is marked with blue stars. | 38 |
| 3.9 | a) Cross-correlation between X-ray t_0 and the most intense VHF pulses (top 25%), and between the less intense VHF pulses (bottom 75%). In both cases we considered an uncertainty of $\pm 0.5 \mu s$ on t_0 . b) Probability density function obtained from a Monte Carlo simulation to evaluate the p-value, in the case of study presented in Figure 8. . . . | 39 |
| 3.10 | a) Time difference between the X-ray t_0 and the VHF pulses associated. This quantity was evaluated in all X-ray bursts (gray) and in the X-ray burst 2019-11-11 06:39:06 (blue). b) Distribution of the VHF pulses associated with X-ray emissions. The VHF amplitude is expressed in quantiles to allow comparison between different events. | 40 |
| 3.11 | a) Analysis of the leader speed in relation with the high-energy radiation. Nine leader branches were examined and the 2D speed was calculated averaging all the VHF sources in a time interval of $10 \mu s$. The regions of interest are indicated by arrows and delimited by a contour plot, the X-ray sources are marked with black stars. Speed values greater than 4.0×10^6 m/s were saturated to this maximum value. . . | 41 |
| 3.12 | Collection of nine leader branches of the lightning event 2019-11-11 06:39:06:518 (UTC). The graphs show the VHF sources averaged in a time interval of $10 \mu s$. The height-time plot shows the 1D averaged leader speed computing the slope (p1) of the linear fit. It is possible to appreciate the variation of the leader speed and secondary branching in the time domain. The likely sources of high-energy radiation are marked with black stars. | 43 |

| | | |
|------|--|----|
| 3.13 | Dart leader associated with the detection of high-energy emissions. The lightning map is obtained with the VHF broadband lightning interferometer (INTF-1). The image is colored by time and the most likely location of the X-ray sources is marked with black stars. | 44 |
| 3.14 | Analysis of the 1D-speed of the dart leader. The graph shows in background the VHF signal and in black dot line the VHF amplitude of the sources. The time evolution of the VHF source height is depicted with blue dots and the black star markers represent the most likely height of the X-ray sources. Finally, the linear interpolation of the speed is superimposed. | 45 |
| 3.15 | Negative downward leaders event associated with the detection of an X-ray burst. a) Density plot of all the VHF sources that could be related to the high-energy emission in a time interval δt of $\pm 1 \mu s$ with respect to the X-ray t_0 . b) Temporal association between the X-ray pulses (blue lines and labels) and VHF amplitude peaks, the correspondence is marked with blue stars. Zoom of the last 200 μs | 45 |
| 3.16 | Assumption of a correspondence between the most intense VHF pulses and the high-energy radiation sources applied on real data. a) Most intense VHF sources, colored by VHF amplitude, if associated with X-ray detection marked with black stars. b) Temporal correspondence between VHF pulses and high-energy radiation sources. If the correspondence was really observed (blue stars) if only hypothesized (black dots). | 50 |
| 4.1 | Multi-stroke +CG flash along the same channel, event: 2019-10-27 11:15:06 (UTC). a) Electric field waveform recorded by a flat plate antenna, LINET detections (Betz et al. 2009) and Geostationary Lightning Mapper (GLM) energy (Goodman et al. 2013). b) Flash evolution in altitude, Quasi-3D data. c) Time-distance plot from the flash initiation, Quasi-3D data. d) Time-elevation plot, INTF data compared with LMA data. e) Spatial development of the flash, Quasi-3D data. f) Elevation-azimuth plot, INTF data. It is possible to observe (see letter A) the subsequent positive stroke (red) along the same pre-existing cloud-to-ground channel (green). The correspondence between panels e) and f) is highlighted through the letters A-F. An animation of the entire flash is available in the Supporting Information S1. | 57 |

- 4.2 Schematic illustration of the multi-stroke +CG flash 2019-10-27 11:15:06. Blue and red lines indicate respectively propagating negative leaders and propagating positive leaders (observed by the INTF). Green lines indicate fast lightning processes such as recoil leaders or fast new breakdowns. The gradient color indicates time evolution, and the faded color indicates decayed channels which are no longer propagating. 59
- 4.3 Initiation of the second DPL along a previous channel to ground, multi-stroke +CG flash 2019-10-27 11:15:06 (UTC). a) Overview of the last 4 ms before RS2. Time-elevation plot of the VHF sources mapped by the INTF and LMA. Electric field waveform (red line) recorded by the flat plate antenna and VHF waveform (gray line). Black arrows indicate the electric field variations in correspondence, respectively, with the approaching recoil leader (EF1), and the DPL (EF2). b) and c) Recoil leader and new breakdown connecting a previous channel end to the flash origin. Respectively colored by time and VHF power. d) Elevation-azimuth plot of the leader channels A-C. e) VHF sources in the subsequent 300 microseconds after the DPL connection to the ground. It is relevant to note VHF activity near the previous leader channels A-C. 62
- 4.4 Comparison between the first and the second positive strokes of the multi-stroke event: 2019-10-27 11:15:06 (UTC). a) VHF waveform and sources mapped by the VHF broadband interferometer (INTF) of the first positive stroke. The intermittent pattern of VHF waveform is highlighted through two different shades of gray, an envelope (red line) and its magnitude local maxima (blue dots). b) Elevation-azimuth plot of the VHF sources mapped by the INTF, c) VHF waveform and sources of the second positive stroke. d) Elevation-azimuth plot. . . . 64
- A.1 Illustration of the algorithm to detect t_0 . Red lines are the linear interpolations, blue lines and triangles represent t_0 , the tiny error bars represent the uncertainty $\pm 0.5\mu s$ 75
- A.2 Graphical evaluation of imaging efficiency. The range selected is particularly relevant for the high-energy emissions analysis. Black spline shows the VHF average amplitude provided by the interferometer, the green and orange sources belong to the lightning leader imaging the black sources are mislocated or due to the noise (case 2), the red VHF pulses are the entirely skipped VHF sources (case 1). Blue stars are the VHF sources associated with the X-ray pulses. 77

| | | |
|-----|--|----|
| A.3 | Graphical evaluation of imaging efficiency. The green and orange sources belong to the lightning leader imaging the black sources are mislocated or due to the noise (case 2). The noise is the 17% of the VHF sources but it is overestimated due to the leader branch in the red box. | 78 |
| A.4 | a) VHF sources and pulses in function of time and a graphical evaluation of the quantiles. The red line is the median (top 50%), blue line corresponds to the top 25% blue stars are the VHF pulses associated with the X-rays emissions. b) VHF pulse distribution of the last 3 ms before the RS, black stars are the VHF pulses associated with the X-rays emissions. | 80 |
| A.5 | a) Cross-correlation between VHF pulses and X-ray t0 considering an uncertainty on t0 of $\pm 0.5\mu s$. b) Cross-correlation between the most intense VHF pulses (top 25%) and X-ray t0 (in blue) and cross-correlation between the less intense VHF pulses (bottom 75%) and X-ray t0 (in gray) in both cases considering an uncertainty on t0 of $\pm 0.5\mu s$ | 81 |
| A.6 | a) Zoom of the most interesting temporal range of event 2019-11-11 06:39:06. In the last 180 μs , sixteen X-rays pulses can be associated with the most intense VHF pulses (Top 50%) with an average absolute deviation of $\bar{\Delta}t < 0.365 \mu s$. b) Probability density function obtained from a Monte Carlo simulation to evaluate the p-value of the case of study presented in a). | 82 |
| A.7 | a) Time difference between the X-ray t0 and the VHF pulses associated. This quantity was evaluated in all X-ray bursts (gray) and in the X-ray burst 2019-11-11 06:39:06 (blue). b) Distribution of the VHF pulses associated with X-ray emissions. The VHF amplitude is expressed in quantiles to allow comparison between different events. | 83 |
| A.8 | High-energy spectrum of our NaI(Tl) detector. The figure show the background X-ray and gamma-ray energy spectrum in fair weather and during thunderstorms. (Data from our campaign in Colombia in 2019) | 84 |

| | | |
|-----|--|----|
| B.1 | a) Temporal development of the thunderstorm to which belongs observations of flash 2019-10-27 11:05:10 and flash 2019-10-27 11:15:06. The scatter plot are the VHF sources recorded by the LMA in the area of interest, the total flash rate and the LINET detections of CG strokes are superimposed. The multipanel below (b,c,d,e) shows the charge structure reconstructed by the LMA data in the area of interest, in a temporal range of 20 minutes around the events observed. The positively charged region is colored red and the negatively charged region blue. | 87 |
| B.2 | a) Closure delay during flash 2019-10-27 11:15:06 (UTC), the closure standard deviation is $\sigma_{\tau_{123}} = 0.125$ ns. b) Angular resolution of our interferometer during flash 2019-10-27 11:15:06 (UTC). | 89 |
| B.3 | a) DPL spatial origin along the horizontal negative channel, Quasi-3D data. b) Elevation-azimuth map and c) Azimuth-time map of the beginning of the flash. The DPL origin and a RL are highlighted in red and green respectively. | 90 |
| B.4 | a) Spectral power density of the two DPLs and an intra-cloud negative leader. N.B. The power spectral density is not normalized between different lightning leader spectra. b) Elevation-azimuth map of the two DPLs. it is possible to appreciate the high angular resolution especially in the azimuth angle. | 91 |
| B.5 | Analysis of the propagation of the downward positive leader (DPL) in virgin air, the data belong to first +CG stroke of the event: 2019-10-27 11:15:06 (UTC). a) Selected range of Figure 3a. We colored alternately a first VHF burst in blue and the subsequent in red. Inter-burst pulses are colored in gray. b) Elevation-azimuth map of the VHF sources located by the INTF, same data of the left panel. c) Scatter plot of the burst VHF pulses in the last 1 ms before the return stroke (RS). The figure shows the VHF amplitude in function of the time and elevation residuals with respect to the mean burst value. d) Scatter plot of the VHF pulses in the last 1 ms before the RS. e) Burst time duration and time elapsed between two subsequent bursts. f) Frequency of the bursts, trend of the number of bursts per 100 microseconds in the last 1 ms before the RS. | 94 |
| B.6 | Multi-stroke +CG flash along the same channel, event: 2019-10-27 11:15:06 (UTC). Quasi-3D conversion of the INTF data and superposition of the LMA sources. | 95 |

- B.7 Initiation of the second DPL along a previous channel to ground, multi-stroke +CG flash along the same channel, event: 2019-10-27 11:05:10 (UTC). Overview of the last 4 ms before RS2. Time-elevation plot of the VHF sources mapped by the INTF. Electric field waveform (red line) recorded by the flat plate antenna and VHF waveform (gray line). 96

Abstract

The aim of this thesis work is the development of a VHF broadband interferometer for lightning research to investigate the high-energy emissions from lightning strikes and the occurrence of multi-stroke positive cloud-to-ground flashes sharing the same channel to ground. This Ph.D. project is contextualized in the European program: Science and Innovation with thunderstorms (SAINT), funded by the Horizon 2020 / Marie Skłodowska Curie Action, grant agreement ID: 722337.

A VHF broadband interferometer is an instrument capable of mapping lightning flashes with extremely high temporal resolution. This feature, combined with the omnidirectional field of view and the ability to map lightning within the cloud, makes this instrument really promising for scientific lightning research. Its use is enriched and enhanced by the installation of other detectors or measuring instruments. In this way, it is possible to simultaneously observe with several instruments the same lightning flash and obtain complementary information needed to advance in the understanding of the physical phenomena.

The main technical challenge of this work was to build our own version of a broadband VHF digital interferometer. This kind of instrument is still a prototype, off the market, and although some books and scientific papers describe how it works, its hardware and software implementation requires a lot of work and refinements to achieve the high performance required by the scientific research. Once the instrument was built and validated, field campaigns were carried out in Spain, Colombia and Italy. Observations made with our VHF broadband interferometer in coincidence with other instruments such as the high-energy detectors, electric field antenna, and Lightning Mapping Array (LMA) have made it possible to make some progress in understanding some unsolved aspects of lightning physics. The results of our research have been published mainly in the two scientific articles that constitute this Ph.D. thesis.

The first article of this compendium presents measurements in coincidence of high-energy radiation with the lightning mapping provided by the VHF broadband interferometer. During a field campaign in north-central Colombia, several intense X-ray bursts were detected from negative stepped leaders and dart leaders. A strong temporal correlation has been observed between the high-energy emissions and the most intense VHF pulses, which suggests the runaway electrons as a shared mechanism. We observed multiple high-energy sources belonging to different leader branches and we speculate that the high-energy emissions could occur more often than expected. We speculated a few possible implications for TGFs.

The second article presents the first observation of a multi-stroke positive cloud-to-ground lightning flash sharing the same channel to ground mapped with a VHF broadband interferometer and a Lightning Mapping Array. We propose a mechanism to describe this rare phenomenon and we identify in a fast recoil leader or a fast breakdown a crucial role in reconnecting these previously decayed leader channels and initiating the subsequent positive stroke. We investigated the polarity asymmetry of subsequent strokes.

Finally, in the appendix, further measurements and insights contained in the peer-reviewed Supporting Information documents of both articles were reported.

Resumen

El objetivo de este trabajo de tesis consistió en desarrollar un interferómetro de banda ancha en Very High Frequency (VHF) para la investigación de rayos. Las observaciones con este instrumento nos permitieron investigar algunos aspectos no resueltos de las descargas eléctricas atmosféricas relacionadas con emisiones de alta energía al igual que ocurrencia de rayos a tierra de polaridad positiva que comparten el mismo canal. Este proyecto de doctorado está en el marco del programa europeo Ciencia e Innovación con tormentas eléctricas (SAINT) financiado por la ayuda Horizonte 2020 / Marie Skłodowska Curie, grant agreement: 722337.

Un interferómetro de banda ancha VHF es un instrumento capaz de mapear los rayos con una resolución temporal de alta velocidad. Esta característica, combinada con el campo de visión omnidireccional y la capacidad de mapear los rayos dentro de la nube, hace que este instrumento sea realmente prometedor para la investigación científica de los rayos. Su uso se enriquece y mejora con la instalación de otros detectores o instrumentos de medición. De este modo, es posible observar simultáneamente con varios instrumentos el mismo relámpago y obtener información complementaria necesaria para avanzar en el entendimiento de los fenómenos físicos asociados con los rayos.

El principal reto técnico de este trabajo ha sido construir nuestra propia versión de un interferómetro digital VHF de banda ancha. Este tipo de instrumento es todavía un prototipo fuera del mercado, y aunque algunos libros y artículos científicos describen su funcionamiento, su implementación de hardware y software requiere aún mucho más trabajo y perfeccionamiento para lograr su alto rendimiento. Una vez construido y validado el instrumento, se realizaron campañas de observación en España, Colombia e Italia. Las observaciones realizadas con nuestro interferómetro en conjunto con otros instrumentos como los detectores de alta energía, la antena de campo eléctrico y el Lightning Mapping Array (LMA) han permitido avanzar en la comprensión de algunos aspectos no resueltos de la física del rayo. Los resultados de

nuestras investigaciones se han publicado principalmente en dos artículos científicos que constituyen esta tesis doctoral.

El primer artículo de este compendio presenta las mediciones de rayos proporcionada por el interferómetro en coincidencia con detecciones de alta energía producidas por el mismo fenómeno atmosférico. Durante una campaña de campo en el centro-norte de Colombia, se detectaron varias ráfagas intensas de rayos X producidos por líderes escalonados negativos y líderes dardos. Se ha observado una fuerte correlación temporal entre las emisiones de alta energía y los pulsos VHF más intensos, lo que sugiere un mecanismo compartido con lo runaway electrons. También se observaron múltiples fuentes de alta energía pertenecientes a diferentes ramas de líderes, lo que podría sugerir que las emisiones de alta energía pueden ocurrir con más frecuencia de lo esperado. Especulamos algunas posibles implicaciones para la producción de TGFs.

El segundo artículo presenta por primera vez la observación de un rayo de polaridad positiva con múltiples descargas subsecuentes que comparten el mismo canal a tierra y mapeado con el interferómetro y el sistema Lightning Mapping Array. Con esta segunda publicación proponemos un mecanismo para describir este extraño fenómeno en el que identificamos en un líder de retroceso rápido o fast breakdown como un papel crucial en la reconexión de estos canales de líderes rápidos iniciales con en el inicio de la siguiente descarga subsecuente positiva. A su vez, investigamos la asimetría de la polaridad de los líderes de rayos con las descargas subsecuentes a tierra.

Por último, en el apéndice se presentan otras mediciones y los documentos del material suplementario de ambos artículos.

Acronyms

- **AGILE**: Astrorivelatore Gamma ad Immagini LEggero
- **ASIM**: Atmosphere-Space Interactions Monitor
- **BATSE**: Burst And Transient Source Experiment
- **CAMMA**: Córdoba Argentina Marx Meter Array
- **CC**: Continuing Current
- **CG**: Cloud-to-ground
- **CGRO**: Compton Gamma-Ray Observatory
- **COLMA**: Colombia Lightning Mapping Array
- **DPL**: Downward Positive Leader
- **EF**: Electric field
- **FA**: Fast Antenna
- **FFT**: Fast Fourier Transform
- **GLM**: Geostationary Lightning Mapper
- **GPS**: Global Positioning System
- **IC**: Intra-cloud
- **INTF**: Interferometer, (VHF broadband interferometer)
- **ISS**: International Space Station

- **LB**: Leader branch
- **LINET**: Lightning detection Network (Nowcast GmbH, Keraunos Colombia)
- **LIS**: Lightning Imaging Sensor
- **LMA**: Lightning Mapping Array
- **LOFAR**: Low Frequency Array
- **MMIA**: Modular Multi-Imaging Assembly
- **MXGS**: Modular X- and Gamma-ray Sensor
- **PMT**: Photomultiplier
- **RF**: Radio frequency
- **RMS**: Root mean square
- **RREA**: Relativistic Runaway Electrons Avalanche
- **RS**: Return Stroke
- **SAINT**: Science And INnovation with Thunderstorm
- **SI**: Supporting Information
- **SNR**: Signal-to-noise ratio
- **TGF**: Terrestrial Gamma-ray Flash
- **TLE**: Transient Luminous Event
- **TOA**: Time of arrival
- **VHF**: Very High Frequency
- **VLF**: Very Low Frequency
- **+CG**: Positive cloud-to-ground
- **−CG**: Negative cloud-to-ground
- **2D**: Two-dimensional
- **3D**: Three-dimensional

1. Introduction

1.1 Relevance and motivation

Despite being one of the most fascinating phenomena of nature, lightning still have many unresolved aspects and open questions. Beyond the purely scientific interest, it is absolutely relevant understanding lightning for protection reasons. Lightning plays an important role in the dynamics of our atmosphere and have a major impact on our society and economy, causing a lot of damage to buildings, tall structures such (like wind turbines), aircraft and electronics. Lightning strikes can initiating wild-fires and especially causing loss of human lives (Rakov & Uman, 2003).

Lightning are a complex phenomenon which involves physical processes with different temporal and spatial scale. Currently, it is still not fully understood their initiation and the mechanism able to produce the charge separation which produce the high potential difference needed to the lighting propagation. Another crucial issue is the charge polarity asymmetry. Positive lightning has different characteristics and behavior than negative lightning, and this diversity results in the occurrence of different physical phenomena. Especially two types of lightning-related phenomena are currently being investigated with great interest: Terrestrial gamma-rays flashes (TGFs) and Transient Luminous Events (TLEs).

A Terrestrial Gamma-rays Flash (TGF) consists on an intense burst of gamma radiation produced during a thunderstorm and it was detected for the first time by the Burst and Transient Source Experiment (BATSE) onboard the Compton Gamma-Ray Observatory (CGRO) satellite (Fishman et al.,1994). This phenomenon was unexpected at the time of discovery, and although it has been studied since then, the mechanism behind TGFs is still debated, and its occurrence and characteristics are still being investigated . Although the main research approach on TGFs is carried out by space-based instruments (AGILE and Fermi satellite and ASIM instrument

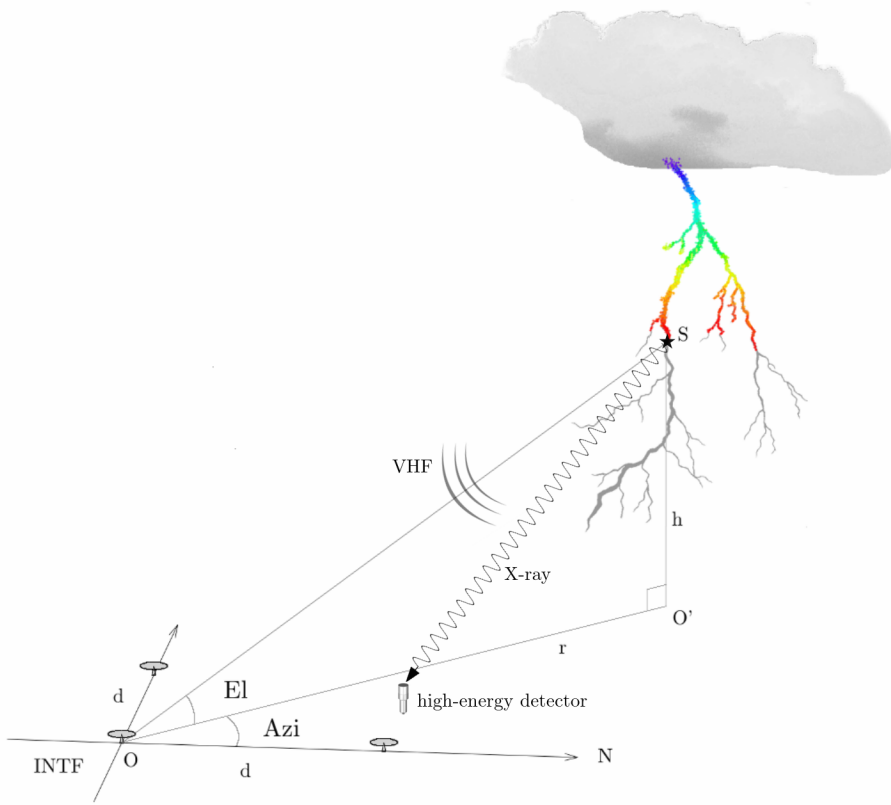


Figure 1.1: Sketch of the measurement technique. The lightning leader propagation is mapped by the VHF broadband Interferometer (INTF) and simultaneously the X-ray emissions are detected by the high-energy detector. (Image not in scale)

on the ISS), new details and important contributions can be made by ground-based instruments.

A VHF broadband interferometer is a privileged instrument for investigating lightning phenomena. It has a very high temporal resolution, at least one order of magnitude higher than other lightning detection networks with remote sensors, and its strength is the capability to resolve in detail leader channels and breakdown discharges even inside the cloud. If it is configured to acquire data in coincidence with other detectors or measuring instruments (like high-energy detectors, fast electric field antenna, photometers or high-speed camera), which add complementary information, this powerful instrument provides the lightning VHF mapping and flash development at the time of simultaneous detections. The combined information from a multi-instrument installation allows us to better depict lightning phenomena and make progress in their understanding with new scientific findings.

For this Ph.D. project, a VHF broadband interferometer was developed and installed together with high-energy detectors, fast electric field antenna and a Lightning Mapping array. The main goal was to measure in coincidence the high-energy emissions in lightning strikes and contribute to a better understanding of lightning phenomena.

1.2 Objectives

This Ph.D. project is contextualized in the European program: Science and Innovation with thunderstorms (SAINT), being part of Marie Skłodowska Curie Action Innovative Training Network (MSCA-ITN-2016) funded by the European program Horizon 2020, grant agreement ID: 722337. SAINT is an educational platform within a multidisciplinary scientific network of scientists leading the European space missions of ASIM, and the US mission ISS-LIS. The SAINT Training Program supports Ph.D. education for 15 Early-Stage Researchers (ESR) within the environment of 8 universities, 8 industrial partners, and 3 agencies and research institutes. This Ph.D. project titled “High-energy radiation from lightning strikes” (ESR 7) was carried out within the Lightning Research Group of the UPC.

The main objective is the development of a digital VHF broadband interferometer to investigate the lightning processes related with the high energy emissions. Install this instrument for observational field campaigns and simultaneously measure high-energy emissions with the VHF mapping of the leader propagation. Due to the exceptional performance of this instrument, a secondary objective is to carefully analyze the collected data in search of rare phenomena, like multi-stroke positive cloud-to-ground lightning along the same channel.

The specific objectives accomplished during this Ph.D. are:

- Gain a deep understanding of the lightning interferometry techniques and the physics of high-energy radiation processes in lightning.
- Develop a digital VHF broadband interferometer with high performance. Hardware and software design of the instrument, the acquisition system and the processing chain of the raw data.
- Validate the new instrument with the Lightning Mapping Array (LMA).
- Lead several field observational campaigns (Spain, Colombia and Italy). Install and operate the VHF broadband interferometer and other instrumentation.
- Measure in coincidence the high-energy radiation with the VHF emission recorded by the interferometer.

- Process the collected data and analyze in great detail the most interesting case of studies.
- Interpret the collected data in light of the current understanding of lightning phenomena and the literature.
- Upgrade and improve the instrument with the gained experience.
- Write scientific publications in high impact factor journal on the research topic of the PhD project.

1.3 Thesis structure

This thesis is planned as a compendium of two scientific articles. This document is divided into 5 chapters: Chapter 1 presents the motivation, the context and the objectives of the work performed during the PhD. Chapter 2 is focused on the state of the art of these research topics and provide a brief introduction of the main concepts and a review of the main reference in literature.

Chapter 3 is the first article of the compendium, titled "High-energy radiation from natural lightning observed in coincidence with a VHF Broadband Interferometer" and published on Journal of Geophysical Research: Atmospheres. This paper is focused on the X-ray bursts detected simultaneously with the lightning mapping provided by the VHF broadband Interferometer.

Chapter 4 is the second article of the compendium, titled "Multi-stroke positive cloud-to-ground lightning sharing the same channel observed with a VHF Broadband Interferometer" and published on Geophysical Research Letters. This paper is focused on the observations of multi-stroke positive cloud-to-ground lightning sharing the same channel to ground. A mechanism for the phenomenon is proposed based on the unprecedented observations. This paper contributes in the understanding of the charge polarity asymmetry in lightning.

Chapter 5 summarize the main finding and the original contribution of this thesis work. Finally, in appendices the Supporting Information of both papers are reported. They provide supplementary analysis and complementary information.

2. State of the art

This chapter presents the state of the art of the main topics covered in this thesis. This review is inspired by the most relevant and cited references in the field, combined with recent publications. For the review of lightning interferometry, Micheal Stock's book: "Broadband interferometry of Lightning" (Stock, 2014). For the review of the high-energy radiation from lightning: "High-Energy Atmospheric Physics: Terrestrial Gamma-Ray Flashes and Related Phenomena" (Dwyer, Smith, & Cummer, 2012) and for general concept and positive CG lightning, the book "Lightning: Physics and Effect". (Rakov & Uman, 2003).

2.1 Lightning interferometry

Lightning discharges emit radiation on almost the entire electromagnetic spectrum, from extremely low frequency (ELF) to the gamma-ray energy. Emissions in the radio frequency band can be used to map flashes.

The VLF/LF (3 – 30kHz / 30 – 300kHz) receivers are commonly used to locate high current impulses produced by cloud-to-ground (CG) strikes and some intra-cloud (IC) flashes on a very wide area of thousands kilometers squared. While the very high frequency (VHF) radiation (30 – 300MHz) is produced by smaller-scale breakdown activity and can be used to map the detailed development of individual flashes inside a thunderstorm.

A lightning interferometer is an instrument able to map lightning discharges correlating the signal received by two or more antennas. The distance between a pair of antennas is called "baseline". The interferometry technique allows to locate a radio point source calculating the phase difference between the interference fringes, due to the geometrical deployment of the antennas.

This kind of instruments have been used with great success for several decades to study the physical processes in a lightning flash, but limitations due to technology, the acquisition sample rate, the memory and the computational cost of the data analysis had limited the capability to investigate the lightning with this technique until recent years.

2.1.1 VHF lightning mapping

The VHF lightning mapping has traditionally been done one of following ways:

- by using interferometric technique to determine the direction of arrival of the radiation (e.g., Warwick et al., 1979; Hayenga, 1984; Richard et al., 1986; Rhodes et al., 1994; X. Shao & Krehbiel, 1996; Ushio et al., 1997; Kawasaki et al., 2000; Stock et al., 2014; Sun et al., 2014; Lyu et al., 2016; Tilles et al., 2019; Li et al., 2020; Pu et al., 2021; Urbani et al., 2021)
- by using time of arrival (TOA) measurements to image the lightning in three dimensions (e.g., Proctor et al., 1988; Rison et al., 1999; Thomas et al., 2004; Lyu et al., 2014; van der Velde et al., 2014; López et al., 2016; Chmielewski et al., 2022)

The main difference between time of arrival (TOA) and interferometric lightning location system is the use of coherence during the data processing. A TOA system makes use of a peak detector, which determines the time of a VHF source independently by another station. An interferometric system makes use of a peak detector, to select the maximum of the cross correlation function of the signals arriving at two antennas.

2.1.2 Basics of VHF lightning interferometry

A lightning interferometer is an instrument that allows to map in 2D radio point sources computing the phase difference between the interference fringes recorded by the antennas .

Two main assumptions are necessary for consistent use of the interferometry technique. First, the source of the radiation should be considered as a point source in a determined interval of time. Second, the source of the radiation should be far enough to consider as first approximation a plane waveform . Both assumption are generally respected in VHF lightning observations, due to the impulsive nature of the VHF

emissions and the usual distance between the lightning development and the interferometer.

The simplest version of this instrument consists of three antennas deployed along two orthogonal baselines. From geometrical considerations it is possible to compute the delay Δt_{ij} between pairs of antennas with baseline d .

$$d \cos \alpha = c \Delta t_{ij} = \left(\frac{\Delta \phi_{ij}}{2\pi} \right) \lambda \quad (2.1.1)$$

Where c is the speed of light in air and λ is the wavelength of the radiation. In Fig.2.1 an illustration with the basic geometry of the lightning interferometer is depicted.

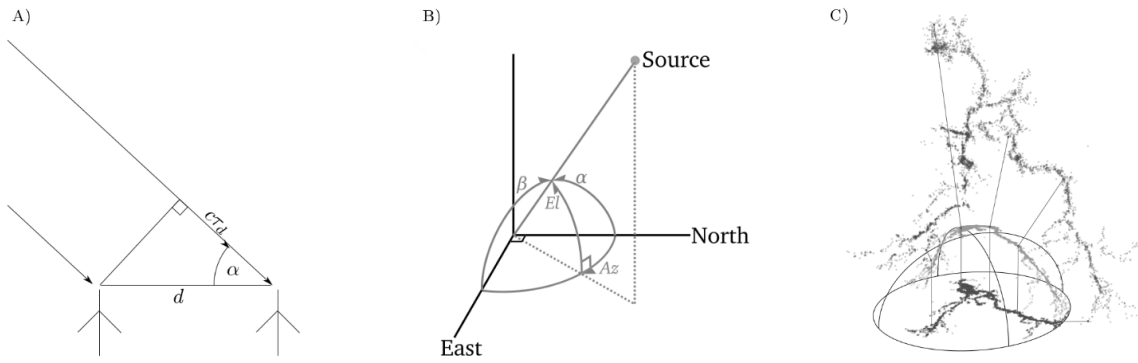


Figure 2.1: A) Phase delay due to geometry. B) Coordinate system for three antennas. C) The $\cos \alpha$ vs $\cos \beta$ plane. (Figure adapted from Stock, 2014)

In order to get the 2D map of the VHF sources, two angles are needed to specify the direction. Using the direction cosines, from spherical trigonometry, it is possible writing the following relations.

$$\begin{aligned} \cos \alpha &= \sin(Azi) \cos(El) \\ \cos \beta &= \cos(Azi) \cos(El) \end{aligned} \quad (2.1.2)$$

From which are obtained through calculations the azimuth and elevation angles in functions of the geometric delays Δt_{ij} between the antennas.

$$\begin{aligned} Azi &= \arctan \left(\frac{\Delta t_{12}}{\Delta t_{13}} \right) \\ El &= \arccos \left(\frac{c}{d} \sqrt{\Delta t_{12}^2 + \Delta t_{13}^2} \right) \end{aligned} \quad (2.1.3)$$

Where the azimuth angle is defined in degrees $[0;360[$ and the elevation angle $[0;90[$.

The phase ambiguity

Although the direction cosine can be determined directly from correlation measurements, its determination from phase values is more complicated due to the ambiguity of phase measurements. If we consider a monochromatic wave ω with wavelength λ , a phase ambiguity problem appears if the baseline is longer than $\lambda/2$. Figure 2.2 represents two possible angular solutions for the same phase difference in a long baseline. To solve this problem three strategies can be applied: first, reducing the baseline to values below $\lambda/2$; second, increase the number of antennas along the baseline or finally, use broadband technique instead of the traditional narrowband antennas. The first strategy is not convenient in VHF interferometry because longer baselines allow for better angular accuracy. The second strategy works, but requires more antennas and provides results equivalent to a broadband interferometry system (Stock, 2014).

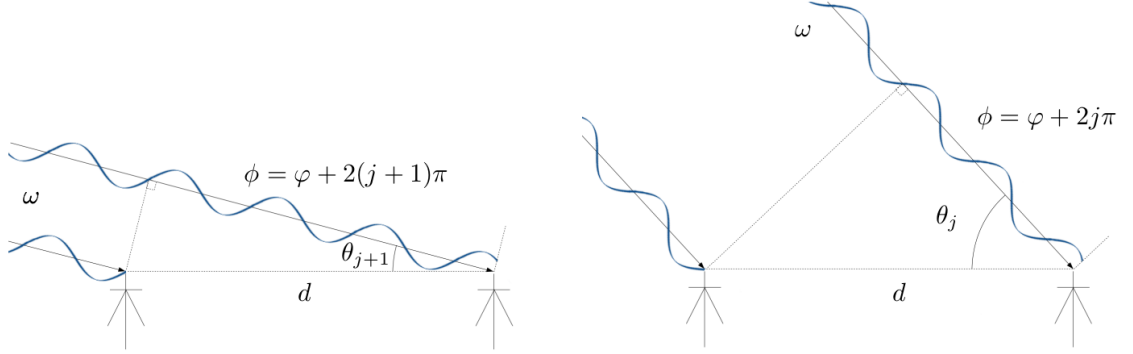


Figure 2.2: Phase ambiguity problem: the same phase difference $\Delta\phi$ measured by the two antennas corresponds to different θ_j . Therefore for a monochromatic wave ω we have an ambiguous location of the source.

2.1.3 VHF Broadband Interferometry

As anticipated, broadband interferometers have two main advantages compared with their narrowband counterparts.

First, correlating the signals at multiple frequencies is equivalent to using multiple baseline lengths at a single frequency (Stock, 2014). In Figure 2.3 it is possible to visualize the effect to remove the ambiguity of multiple frequencies using a broadband signal and filtering with multiple narrowband frequencies. The plot shows in black dots the narrowband solutions and their ambiguity and in red the broadband non-ambiguous solution.

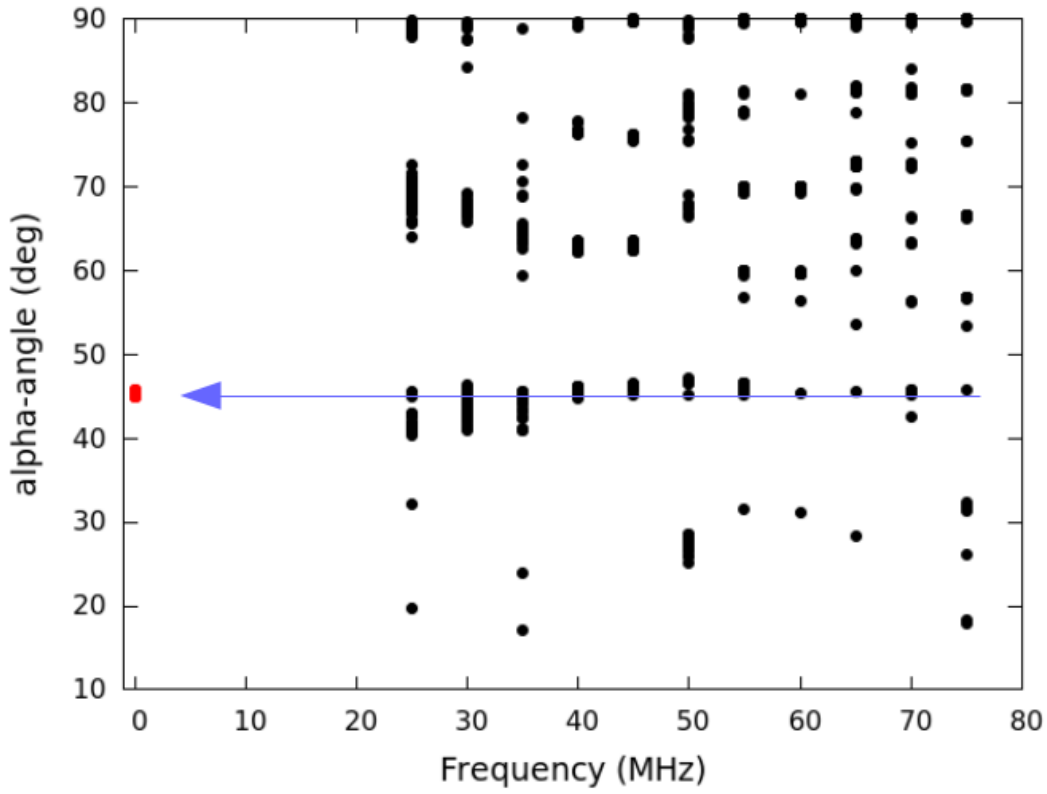


Figure 2.3: Conceptualization of the broadband strategy (real data). The phase ambiguity is solved by the contribution of multi-narrowband frequencies. The correct unambiguous broadband solution in red color, the multi-narrowband frequencies solutions in black color. The arrow shows the combined solution.

Therefore, multiple frequencies concur to determine the phase difference that is calculated through cross-correlation. Hence broadband interferometers are not susceptible to phase ambiguity (if the antenna response is really broadband, and there is any dominant frequency) and can be operated with fewer baselines. Longer baselines could locate a lightning source with greater angular accuracy. The second advantage is that the impulse response of a bandpass filter is inversely proportional to the bandwidth and it allow to have better time resolution.

2.1.4 Generalized cross-correlation technique

The processing technique used in broadband interferometry is called: generalized cross-correlation method. The cross-correlation function can be evaluated directly in the time domain or through the frequency domain thanks to the Parseval theorem with the Fourier transform. Computationally speaking is convenient to use to compute the cross correlation in the frequency domain, using the algorithm called Fast Fourier transform (FFT). Furthermore, this choice allows to filter in frequency the signal and using a weight function $W(f)$ to improve the signal-to-noise ratio (SNR). The transformations scheme is the following:

$$\begin{aligned}
 h_1(t) & \quad \xleftarrow{\mathcal{F}} \quad H_1(f) \\
 g_2(t) & \quad \xleftarrow{\mathcal{F}} \quad G_2(f) \\
 Xcorr_{12}(\tau) & \quad \xleftarrow{\mathcal{F}^{-1}} \quad H_1(f)G_2^*(f) \cdot W(f)
 \end{aligned} \tag{2.1.4}$$

The signals, in time domain from a pair of antennas $h_1(t)$ and $g_2(t)$ are transformed in frequency domain $H_1(f)$ and $G_2(f)$. Then complex multiplication between those functions and a successive inverse FFT returns the cross-correlation function. Through the up-sampling and parabolic interpolation of the cross-correlation peak, it is possible to get the best estimation of the correlation peak to which corresponds the time delay between the signals.

This procedure is iterated several times on short time windows shifted of a constant time step and overlapped to cover the entire time domain of the signals. The choice of the window length and the overlap ratio is crucial to maximize the efficiency and the accuracy of the solution.

Several considerations and numerical conditions can be done to improve the solution and reduce the SNR. The two most efficient are: an amplitude threshold on the entire time window (evaluated considering the noise level) and the closure condition.

$$\tau_{closure} = \Delta t_{12} + \Delta t_{23} - \Delta t_{13} \tag{2.1.5}$$

The amplitude threshold is computationally speaking really efficient, it avoids computing the cross-correlation where it is not needed. The closure condition $\tau_{closure} \approx 0$ increases a lot the SNR because discards all the solutions that do not respect the geometry boundaries, and likely they are mislocated.

2.1.5 Comparison between a Lightning Mapping Array and a VHF Broadband Interferometer

Like any instrument, the interferometer must be calibrated and the results validated with a different method or instruments to ensure reliability and to evaluate the accuracy of the post-processed data. A great option to validate a VHF broadband interferometer is recording simultaneous events with a Lightning Mapping Array.

A Lightning Mapping Array (LMA) is a time of arrival (TOA) system, which accurately measure the arrival times of impulsive VHF event detected at 60 – 66 MHz RF radiation from a lightning discharge at multiple stations, and locates the sources of the radiation to produce a 3D map of the lightning flash. The LMA digitizer sampling rate is 20 MS per second, which corresponds at 50 ns time resolution. The peak detector provides a sample each $80\mu s$. Sources over the network are located with an uncertainty of 6 – 12 m rms in the horizontal and 20 – 30 m rms in the vertical (Thomas et al., 2004).

A VHF broadband interferometer (INTF) is an instrument capable of mapping lightning discharges with a higher temporal resolution. The digitizer used for our INTF acquisition system is a GaGe Razor Express 1604 with four channels, 16-bit resolution, and 200 MS per second sampling rate. The time window length used is 512 samples (2.56 ns), timing uncertainty is 0.1 ns, and the angular resolution is reported in the appendices.

| | Lightning Mapping Array | Broadband Interferometer |
|--------------------------|-------------------------|--------------------------|
| Number Antennas | $\gtrsim 6$ | 3 |
| Baselines | $\sim 5 \div 30$ km | $\sim 20 \div 30$ m |
| Bandwidth | 60 – 66 MHz | 20 – 80 MHz |
| Digitizer sampling rate | 20 MS/s | 200 MS/s |
| Post processing sampling | $80\mu s$ | $\approx 1 \div 2\mu s$ |
| Technique | Time of arrival (TOA) | Cross-correlation |
| Coverage radius | ≈ 100 km | ≈ 10 km |
| Lightning reconstruction | 3D | 2D |

To compare the solutions of the two instruments we need to project the three-dimensional solution of the LMA into the reference system of the Interferometer. It is possible to observe at least an order of magnitude in almost all parameters between the two instruments. Nevertheless, very good agreement is observed, which even makes it possible to combine the solutions and obtain a nearly three-dimensional interpolation of the interferometer data. This interpolation technique is called "Quasi-3D conversion" and is described in the next section.

Quasi-3D conversion

The post-processing technique called “Quasi-3D conversion” was introduced and described by Stock (2014). It consists of an interpolation technique in a few steps: first, the projection of the LMA data on the system of reference of the interferometer; second, a raw approximation of the 3D projection is made for each INTF source by interpolating in the elevation-azimuth plane the projected LMA sources; finally, an iterative procedure using alternately the spatial correlation and successive projections allows an estimation of the radial distance of individual INTF sources.

Figure 2.4 shows the superposition of the LMA sources over the INTF data (Figure 2.4a and Figure 2.4c) and the Quasi-3D imaging (Figure 2.4b). A noise reduction technique was applied considering both sets of data (LMA and INTF). The LMA noise can affect the goodness of the Quasi-3D conversion introducing image artifacts.

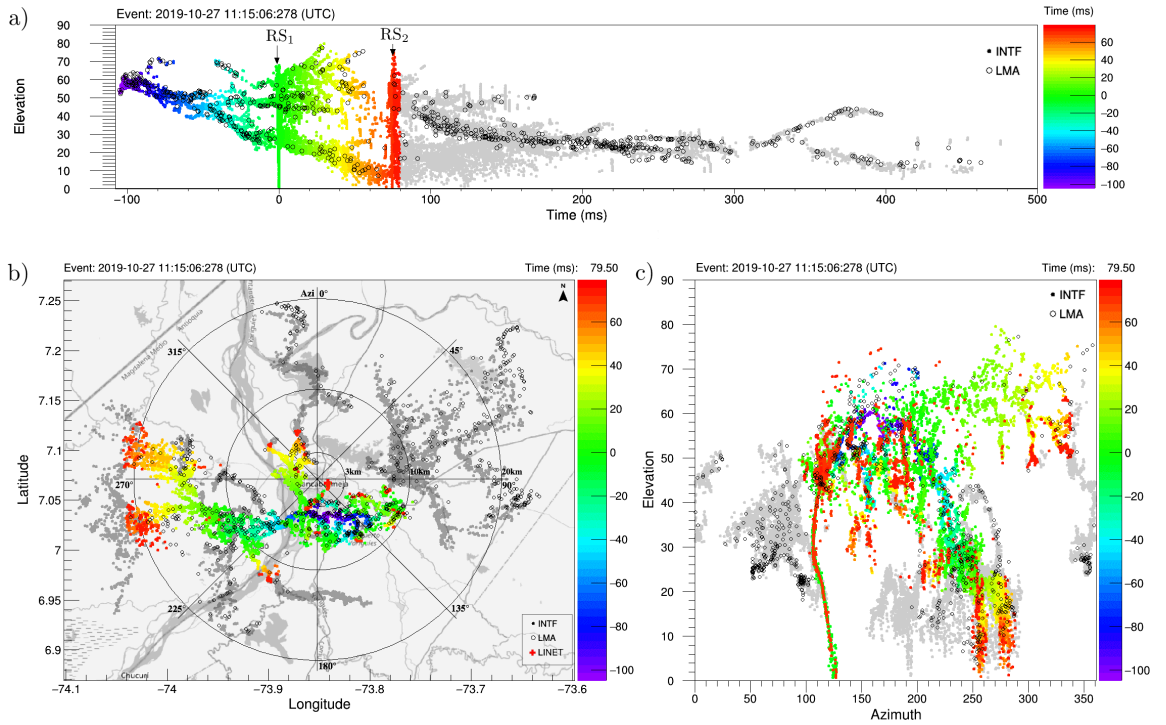


Figure 2.4: Quasi-3D conversion of the INTF data and superposition of the LMA sources over the INTF data.

2.2 High-energy radiation from thunderstorms

The idea that energetic radiation can be produced by thunderstorms was probably first formulated by C.T.R Wilson in 1925. Following this idea, several experiments to observe energetic electrons or x-rays from thunderstorms were led from 1930 till 1990, but much of these early works were inconclusive, because not enough precautions were taken to avoid RF interference in the high-energy instrumentation. (Dwyer, Smith, & Cummer, 2012) Nowadays, there are three main approaches to understanding the observations of high-energy radiation related to thunderstorms.

1. The study of the high-energy fluxes during thunderstorms lasting seconds to minutes, in which energetic particles and/or gamma-ray glows are detected. (e.g., Chilingarian et al., 2010; D. Smith et al., 2018; Wada et al., 2019)
2. The study of the origin of intense gamma-ray bursts named Terrestrial Gamma-ray Flashes (TGFs) detected from space-based instruments. Typically with 1ms duration. (e.g., Fishman et al., 1994; Østgaard et al., 2008; Meegan et al., 2009; Briggs et al., 2010; Marisaldi et al., 2014; Maiorana et al., 2020; Neubert et al., 2020)
3. The study of the production of the high-energy radiation from lightning strikes detected from ground-based instruments. Typically during downward leaders, usually 1ms before the return stroke. (e.g., Moore et al., 2001; Dwyer et al., 2005; Howard et al., 2008; Saleh et al., 2009; Howard et al., 2010; Montanyà et al., 2012; Hill, 2012; Schaal et al., 2013; Tran et al., 2015; Hare et al., 2016; Abbasi et al., 2017, 2018, 2019; M. Saba et al., 2019; Belz et al., 2020; Urbani et al., 2021; Rakov & Kereszy, 2022)

It is currently unclear whether X-ray emissions detected on the ground and TGFs observed in space are essentially the same phenomenon or how these phenomena are related (e.g. Gurevich et al., 2007; Dwyer, Smith, & Cummer, 2012).

Furthermore, it is relevant to note that several authors named their ground-based high-energy observations as TGFs (or downward TGFs). (e.g., Dwyer et al., 2004; Hare et al., 2016; Dwyer, Schaal, et al., 2012; Tran et al., 2015; Abbasi et al., 2018, 2019; M. Saba et al., 2019; Belz et al., 2020; Rakov & Kereszy, 2022).

This research topic has attracted great interest for several decades, as its rarity and difficulty of measurement leaves many questions unanswered and unsolved aspects.

2.2.1 Terrestrial Gamma-ray Flashes

The first scientific evidence that lightning can emit high-energy radiation was the discovery of a phenomenon observed from space called “Terrestrial Gamma-ray Flash” (TGF). This phenomenon consists on an intense burst of gamma radiation and it was detected for the first time by the Burst and Transient Source Experiment (BATSE) onboard the Compton Gamma-Ray Observatory (CGRO) satellite (Fishman et al., 1994).

The duration of these gamma-ray flashes is estimated from $50 \mu\text{s}$ to a few ms, and the photon’s energy can be up to 40 MeV. The origin of TGFs remained uncertain for many years. It was hypothesized that TGFs were associated with discharges in the upper atmosphere such as sprites (Nemiroff et al., 1997), but ground-based measurements conducted during thunderstorms by Moore et al. (2001) revealed a clear correlation between high-energy emissions and lightning leader propagation. In particular, in 2003, a ground-level gamma-ray flash was observed in a rocket-triggered lightning (Dwyer et al., 2004) with a similar duration and energy spectrum of a TGF detected from space. These observations introduced lightning discharges as a candidate to the origin of the TGF and further models and observations confirm that TGFs are produced inside or just above thunderclouds (Cummer et al., 2005; Dwyer & Uman, 2014). Although the exact mechanism that can give rise to TGFs, and the conditions for this process to occur are still debated and subject of research.

2.2.2 Space observations

Beyond the CGRO satellite, the second space instrument able to detect TGFs was the Reuven Ramaty High Energy Spectroscopic Imager (RHESSI) satellite, dedicated to studying solar flares. (D. M. Smith et al., 2005) RHESSI provided the high-energy spectra of TGFs that run from 30 keV to 17 MeV.

Currently, two satellites for astrophysics: AGILE and Fermi are able to detect and catalog TGFs. The satellite Fermi observes TGFs in its Gamma-ray Burst Monitor (GBM) instrument. (Meegan et al., 2009) The GBM is optimized for good resolution in time and photon energy, and is sensitive from 8 keV to 40 MeV.

The “Astrorivelatore Gamma a Immagini Leggero” (AGILE) satellite was built by the Italian Space Agency (Tavani et al., 2009). Like the Fermi satellite, is a tracking detector that determines the direction of incoming high-energy gamma-rays. Marisaldi et al. (2010) used these data to study the geographical distributions. The updated TGFs catalog and the TGFs properties based on the observation of this instrument are reported in Marisaldi et al. (2014); Von Kienlin et al. (2014); Maiorana et al. (2020).

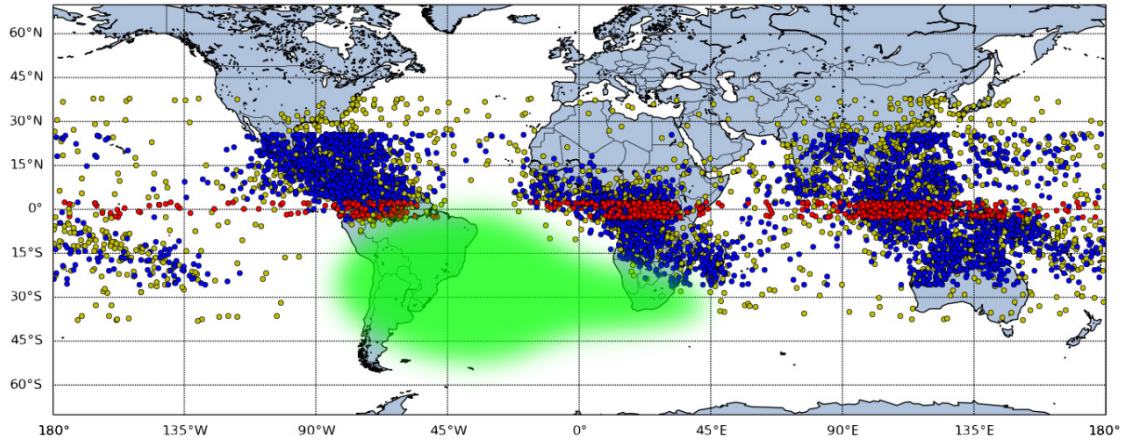


Figure 2.5: Geographic distribution of all TGFs detected by BATSE (yellow), RHESSI (green), AGILE (red) and Fermi (blue). (Figure from Ursi et al. 2017)

Figure 2.5 shows the satellite geographic distribution of all TGFs detected by BATSE, RHESSI, AGILE and Fermi. Recently, for the first time a specific instrument was built to study TGFs from space: the Modular X- and Gamma-ray Sensor (MXGS) of the Atmosphere-Space Interactions Monitor (ASIM) (Østgaard et al., 2019; Neubert et al., 2020) which is currently installed on the Columbus module of the International Space Station (ISS).

2.2.3 Ground-based observations

In the atmosphere, the high-energy radiation undergoes a strong absorption, exponentially proportional to the density of the air, which makes it more difficult to detect TGFs on the ground. Nonetheless, several ground measurements were conducted and observed that even in cloud-to-ground (CG) lightning high-energy radiation could be produced.

The works of Moore et al. (2001) and Dwyer et al. (2005) highlight two lightning processes in which the X-ray bursts could be produced: downward stepped leader and dart leader. The correlation with leader-step electric field derivative and the X-ray emission observed by Dwyer et al. (2005) was confirmed by the measurements of Howard et al. (2008) and Hill (2012). Three-dimensional Radio Frequency (RF) and X-ray measurements were conducted in natural lightning during the attachment process (Howard et al., 2010) and leader bursts were identified as the largest X-ray producers.

Further observations suggested that the X-ray emissions may be beamed to some degree in the direction of the leader propagation and strong VHF emissions were observed (Montanyà et al., 2012). The spatial, energy and angular distribution of the high-energy radiation was debated in (Schaal et al., 2013).

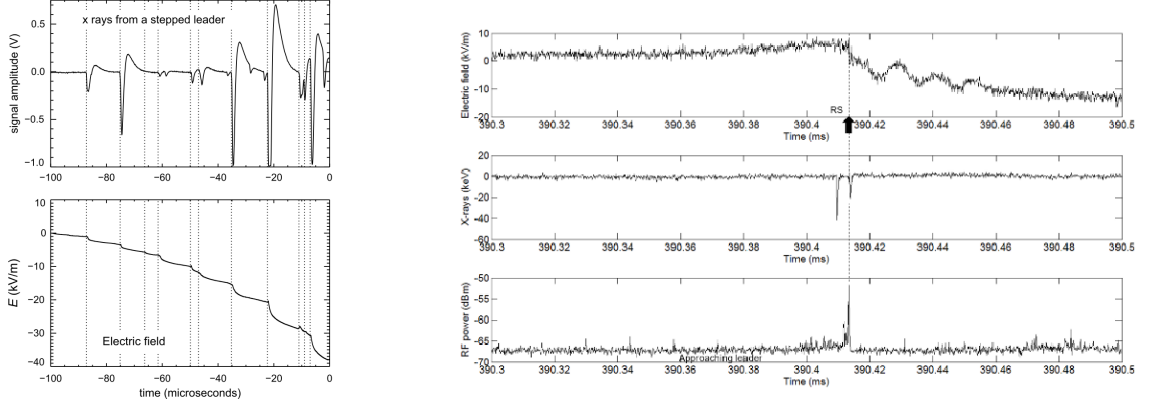


Figure 2.6: *Left:* X-rays from NaT-PMT detectors (top panel) and electric field waveforms (bottom panel) for a natural cloud-to-ground lightning flash at the ICLRT. As can be seen the x-ray pulses are closely associated with the step leader formation. Dwyer et al. (2005) *Right:* Simultaneous measurements of a X-ray emission and microwave RF power peak in a negative return stroke -25 kA ($t=388$ ms). Montanyà et al. (2014)

Due to the lower air density and consequently lower X-ray absorption, observations of high-energy radiation from thunderstorms were conducted at high-altitude towers (e.g., Montanyà, Fabr , et al., 2014; Hettiarachchi et al., 2018) and on aircraft (e.g., D. Smith et al., 2011; Kochkin et al., 2017; Skeie et al., 2020). Recently, M. Saba et al. (2019) measured X-ray emissions in coincidence with a dart leader using high-speed video and pointing out the role of the leader orientation in the X-ray detection. A very recent review of the X-ray burst detection in Florida was published by Rakov and Kereszy (2022).

Recently, several ground-based observations of downward TGF were reported from the Telescope Array in Utah (USA) (Abbasi et al., 2017, 2018, 2019; Belz et al., 2020). The Telescope Array is a cosmic ray observatory which consists of a large array of more than 500 plastic scintillators of 3m^2 deployed in a square grid with 1.2 km spacing. A total of fifteen TGFs were observed in the first 1-2 ms of downward negative breakdown prior to cloud-to-ground lightning strikes (Abbasi et al., 2019). The array detectors revealed that the high-energy radiation is forward-beamed and

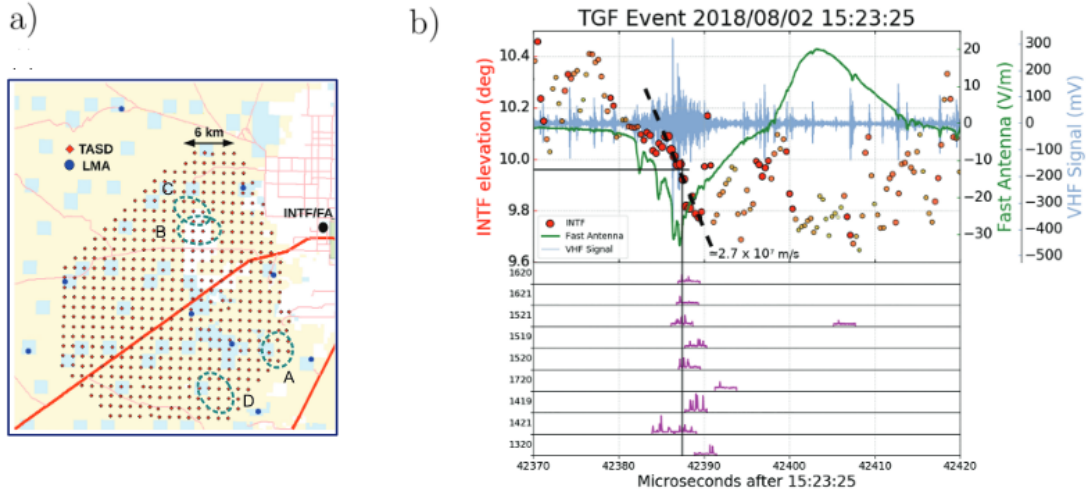


Figure 2.7: a) The Telescope Array in Utah (USA) b) An example of a downward TGF detected from the TA in Utah. (Figure from Belz et al. 2020)

it produces a footprint of 3-5 kilometers in diameter. The observed energy deposit of the gamma-ray shower found is consistent with a fluence of $10^{12} - 10^{14}$ photons.

Three main aspects/differences can be outlined between ground-based measurements and those from space. First, the direction. TGFs measured from space are directed upward, while those measured from space are directed downward. Second, the intensity and energy seem to be different, although we should consider the different detection conditions and in particular the different atmospheric absorption of photons due to the density of the atmosphere and finally their location. TGFs seem to be more likely in the equatorial zone though it is also important to consider the higher thunderstorm activity.

2.2.4 Review of high-energy radiation mechanisms

In this sections the Wilson's runaway electron mechanism, the RREA mechanism, and the relativistic feedback mechanism are briefly summarized following the description provided by Dwyer, Smith, and Cummer (2012). Figure 2.9 depicts the difference between those mechanisms.

Runaway Electrons

In 1925, C.T.R. Wilson discovered the runaway electron mechanism in which energetic electrons may be further accelerated from static electric fields in air. When the rate of energy gain exceeds the energy loss from interactions with air, the energy of an electron increases and it will “run away.”

Runaway electrons are produced in electric fields greater than the break-even field $E_b = 218kV/m \times n$, which corresponds to the minimum ionizing energy loss, where n is the density of air with respect to that at sea level. This field is about one order of magnitude below the conventional breakdown field $E_{cb} = 3200kV/m$ and is comparable to maximum fields seen inside thunderclouds.(Rakov & Uman, 2003)

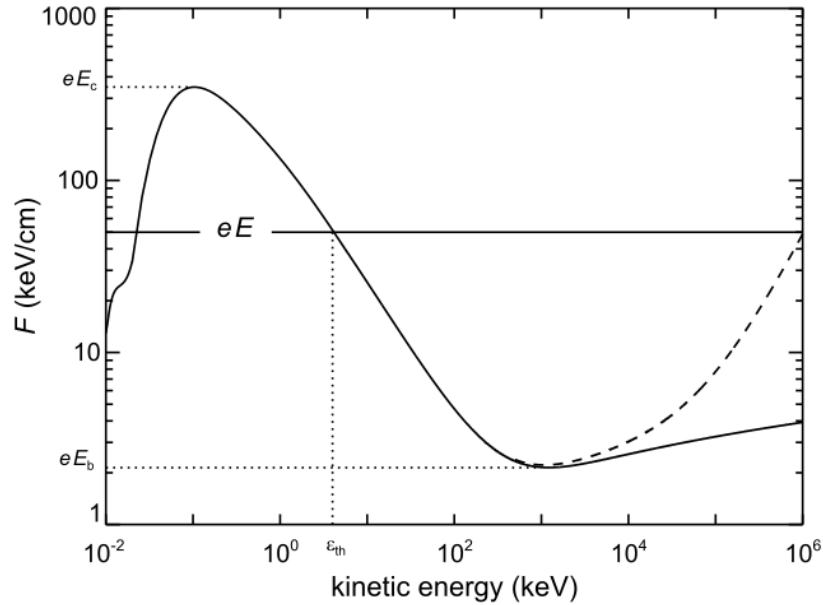


Figure 2.8: The effective frictional force experienced by a free electron (or positron) moving through air at STP as a function of kinetic energy. (Figure from Dwyer, Smith & Cummer 2012)

Figure 2.8 shows the rate of energy loss of an energetic electron moving in air, which is related to the effective frictional force. The plot also shows that rate of energy gain from a strong electric field (horizontal line). As can be seen, in order for an electron to run away, it must have an initial kinetic energy above the threshold, ϵ_{th} .

Such energetic electron, called “seed”, with energies above ϵ_{th} , may be provided from an external source such as cosmic-rays or radioactive decays.

Note that the kinetic energy, ϵ_{th} , required for the seed particles decreases rapidly with increasing electric field. When the electric field is increased above the critical field, E_c , above the energy loss curve for all kinetic energies, then all free electrons may run away, and, in particular, the thermal population created at low energies may run away. This mechanism proposed by Gurevich et al. (1961) is usually called “cold runaway” or “thermal runaway” and does not require any external seed particles.

Relativistic Runaway Electron avalanche (RREA)

McCarthy and Parks (1985) reported intense X-ray bursts, lasting a few seconds each, detected during thunderstorms. They suggested that Wilson’s runaway electrons, could produced the measured bremsstrahlung X-rays. However, this process could not explain the measured fluxes by itself.

Gurevich, Milikh, and Roussel-Dupre (1992) introduced the idea that runaway electrons could undergo a multiplication process through high-energy electron-electron elastic scattering (primarily Møller scattering), and form an avalanche process.

This process is called a relativistic runaway electron avalanche (RREA) and can occur for energetic electrons as long as the frictional force and the radiative energy loss suppress it.

Relativistic feedback mechanism

Modeling high-energy production observed by satellites, it is clear that about 10^{14} and 10^{17} runaway electrons are required to produce a TGF. Dwyer et al. (2003) introduced a new runaway electron production mechanism that involves positive feedback effects from positrons and energetic photons. This mechanism called relativistic feedback could provide a further multiplication factor to explain the high flux produced by TGFs.

In Fig. 2.9 a schematic diagram summarizes the three mechanisms for generating energetic electrons in an atmosphere. By including Møller scattering in the runaway electron mechanism, a relativistic runaway electron avalanche (RREA) is produced, with an increase in the number of runaway electrons of up to 10^5 over the Wilson

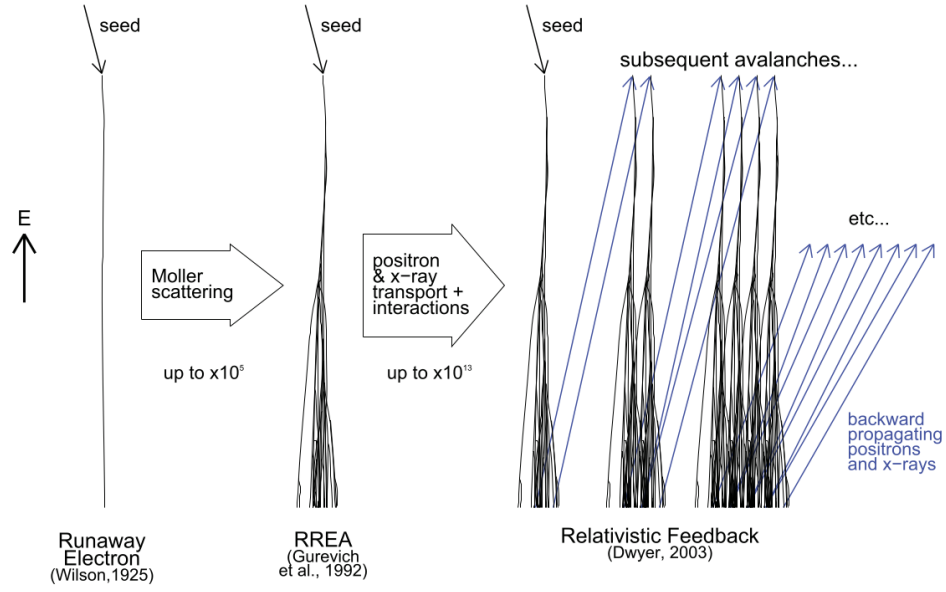


Figure 2.9: Schematic Comparison between the Wilson's runaway electron mechanism, the RREA mechanism, and the relativistic feedback mechanism. (Figure from Dwyer, Smith & Cummer 2012)

runaway electron mechanism. By including positron and x-ray transport and interactions to the RREA mechanism, Relativistic Feedback is produced, with an increase in the number of runaway electrons of up to 10^{13} over the RREA mechanism.

Another possible solution, to explain the TGFs high flux, has been presented by Celestin and Pasko (2011). They show that seed electrons with energies on the order of 60 keV can be produced in the vicinity of the tips of lightning leaders by streamers and be further accelerated in the potential drops in front of lightning leader tips. They found that this process was capable of producing 10^{17} energetic electrons.

3. Urbani et al. (2021): High-energy radiation from natural lightning observed in coincidence with a VHF Broadband Interferometer

M. Urbani, J. Montanyà, O. A. van der Velde, J. A. López, M. Arcanjo, P. Fontanes, D. Romero, J. A. Roncancio, *High-Energy Radiation From Natural Lightning Observed in Coincidence With a VHF Broadband Interferometer*, Journal of Geophysical Research: Atmospheres, 10.1029/2020JD033745, 126, 7, (2021).

3.1 Abstract

This work presents the first simultaneous X-ray measurements from natural lightning in coincidence with a very high frequency (VHF) broadband interferometer. During an observational campaign in north-central Colombia, five intense X-ray bursts were detected from negative stepped leaders and two X-ray emissions from a dart leader. Thanks to the high angular and time resolution of the interferometer, it was possible to locate the origin of high-energy radiation during the lightning leader propagation. We study the correlation with VHF pulses and the two-dimensional speed of the leader channels. A strong temporal correspondence has been observed between the high-energy emissions and the most intense VHF pulses, which suggests the runaway electrons as a shared mechanism. The observations show that an X-ray burst can have multiple high-energy sources belonging to different leader branches, that can be several hundreds of meters apart. Therefore, from a spatial point of view, not a unique origin has to be searched, but an extensive origin of the X-ray burst should be considered. We hypothesize similar conclusions in particular for downward TGFs and maybe for TGFs in general.

3.2 Plain Language Summary

It is well known that lightning can produce high-energy emissions. In particular, a phenomenon has been observed from space called “Terrestrial Gamma-ray Flash” (TGF), which consists of an intense burst of gamma radiation that can be produced during thunderstorms. This phenomenon has met with considerable interest in the scientific community and its mechanism is still not fully understood. Beyond space observations, in order to investigate TGFs, ground-based measurements can provide complementary information to better understand under which conditions high-energy emissions are produced. In this research context, this work presents some accurate ground-based observations of the location of high-energy emissions during natural cloud-to-ground lightning.

3.3 Introduction

The first scientific evidence that lightning can emit high-energy radiation was the discovery of a phenomenon observed from space called “Terrestrial Gamma-ray Flash” (TGF). This phenomenon consists on an intense burst of gamma radiation and it was detected for the first time by the Burst and Transient Source Experiment (BATSE) onboard the Compton Gamma-Ray Observatory (CGRO) satellite (Fishman et al., 1994).

The origin of TGFs remained uncertain for many years. It was hypothesized that TGFs were associated with discharges in the upper atmosphere such as sprites (Nemiroff et al., 1997), but ground-based measurements conducted during thunderstorms by Moore et al. (2001) revealed a clear correlation between high-energy emissions and lightning leader propagation. In particular, in 2003, a ground-level gamma-ray flash was observed in a rocket-triggered lightning (Dwyer et al., 2004) with a similar duration and energy spectrum of a TGF detected from space. These observations introduced lightning as a candidate to the origin of the TGF and further models and observations confirm that TGFs are produced inside or just above thunderclouds (Dwyer & Uman, 2014). It is well established that the high-energy radiation is produced by accelerated electrons via bremsstrahlung, but the exact process that generates the high number of runaway electrons needed to justify the observed TGF brightness is still debated (Dwyer, 2008; Celestin & Pasko, 2011; Dwyer, 2020). Two main theories were proposed to explain the TGF origin, the electron acceleration mechanism and the multiplication factor. The first theory, supported by ground-based observations, claims that the intense electric field ahead of the streamer tips might accelerate thermal electrons to runaway during the stepping lightning leaders (e.g Dwyer, 2004;

Cummer et al., 2005; Moss et al., 2006; Williams et al., 2006; Dwyer, 2008; Carlson et al., 2009; Chanrion & Neubert, 2010; Celestin & Pasko, 2011).

The second theory identifies in cosmic rays the source of the high-energy electrons, named “seeds”, able to trigger the relativistic runaway electron avalanche (RREA) process in thunderstorm ambient electric field (Gurevich et al., 1992). However, the RREA was estimated to not be enough to explain TGFs so an additional mechanism was required to provide enough amplification. In 2003, Dwyer (2003) introduced the “relativistic feedback” a new mechanism involving backward propagating runaway positrons to self-sustain the production of runaway electrons.(e.g Dwyer & Smith, 2005; Dwyer, Smith, & Cummer, 2012; Skeltved et al., 2014). In order to establish which mechanism is dominant and reach a deeper understanding of these high-energy phenomena, more observations are needed.

Currently, two satellites for astrophysics: AGILE and Fermi are able to detect and catalog TGFs (Marisaldi et al., 2014; Von Kienlin et al., 2014; Maiorana et al., 2020) and a specific instrument like the *ASIM-MXGS* detector (Neubert et al., 2020) on the International Space Station are studying TGFs from space. In the atmosphere, the high-energy radiation undergoes a strong absorption, exponentially proportional to the density of the air, which makes it more difficult to detect TGFs on the ground. Nonetheless, several ground measurements were conducted and observed that even in cloud-to-ground (CG) lightning high-energy radiation could be produced.

The works of Moore et al. (2001) and Dwyer et al. (2005) highlight two lightning processes in which the X-ray bursts could be produced: downward stepped leader and dart leader. The correlation with leader-step electric field derivative and the X-ray emission observed by Dwyer et al. (2005) was confirmed by the measurements of Howard et al. (2008) and Hill (2012). Hill located the X-ray sources in 3D via time-of-arrival techniques for dart-stepped leader steps in both natural and triggered lightning. Three-dimensional Radio Frequency (RF) and X-ray measurements were conducted in natural lightning during the attachment process (Howard et al., 2010) and leader bursts were identified as the largest X-ray producers.

In a triggered lightning experiment (Saleh et al., 2009), measurements showed results compatible with isotropic radiation. Instead, further observations suggested that the X-ray emissions may be beamed to some degree in the direction of the leader propagation and strong VHF emissions were observed (Montanyà et al., 2012). The spatial, energy and angular distribution of the high-energy radiation was debated in (Schaal et al., 2013).

A statistical study of X-ray emissions was published by Mallick, Rakov, and Dwyer (2012) with emphasis on subsequent strokes, they observed that not all leaders of the same flash produced detectable X-rays. Due to the lower air density and consequently lower X-ray absorption, observations of high-energy radiation from thunderstorms were conducted at high-altitude towers(e.g. Montanyà, Fabr , et al., 2014;

Hettiarachchi et al., 2018) and on aircraft (e.g. D. Smith et al., 2011; Kochkin et al., 2017; Skeie et al., 2020). Recently, M. Saba et al. (2019) measured X-ray emissions in coincidence with a dart leader using high-speed video and pointing out the role of the leader orientation in the X-ray detection.

Currently, it is not clear if the X-ray emissions detected at ground level and the TGFs observed in space are essentially the same phenomenon or how these phenomena are related (e.g. Gurevich et al., 2007; Dwyer, Smith, & Cummer, 2012).

It is relevant to note that several authors named as TGFs (or downward TGFs) their high-energy observations. Two TGFs cases were reported from rocket-triggered lightning (Dwyer et al., 2004; Hare et al., 2016), and other two cases in association with negative CG lightning (Dwyer, Schaal, et al., 2012; Tran et al., 2015) in Florida (USA). Gamma-ray glows and downward TGFs were also observed from ground during Japanese winter thunderstorms (e.g. D. Smith et al., 2018; Wada et al., 2019).

Recently, several ground-based observations of downward TGF were reported from the Telescope Array in Utah (USA) (Abbasi et al., 2017, 2018, 2019). The Telescope Array is a cosmic ray observatory which consists of a large array of more than 500 plastic scintillators of 3m^2 deployed in a square grid with 1.2 km spacing. A total of fifteen TGFs were observed in the first 1-2 ms of downward negative breakdown prior to cloud-to-ground lightning strikes (Abbasi et al., 2019). The array detectors revealed that the high-energy radiation is forward-beamed and it produces a footprint of 3-5 kilometers in diameter. The observed energy deposit of the gamma-ray shower found is consistent with a fluence of $10^{12} - 10^{14}$ photons. Simulations on the beaming geometries, the fluence, and the time dispersion were discussed by (Berge & Celestin, 2019). These downward TGF observations show that it is particularly interesting and promising to study high-energy emissions also from ground-based instruments. Despite the strong absorption of the high-energy radiation, ground-based observations can reach a better accuracy in time and space and provide crucial information to investigate the origin and conditions under which these emissions occur.

A privileged instrument for this research is a VHF Broadband Lightning Interferometer, a system of antennas that allows to map lightning through the VHF emission. An extensive description of this instrument and its performance it has been provided by Stock et al. (2014). Due to the high resolution of this instrument, it is possible to locate the origin of the high-energy emissions and hopefully provide a better understanding of the radiation mechanism.

3.4 Instrumentation and Methodology

The measurements reported were made during an observational campaign at the Universidad Industrial de Santander (UIS) campus of Barrancabermeja (Colombia)

in autumn 2019. On this site, two lightning interferometer (INTF-1 and INTF-2) were installed and synchronized with a flat-plate antenna, a high-energy detector and a GPS receiver. Figure 3.1 shows the deployment of the instrumentation on the roof of the university main building.

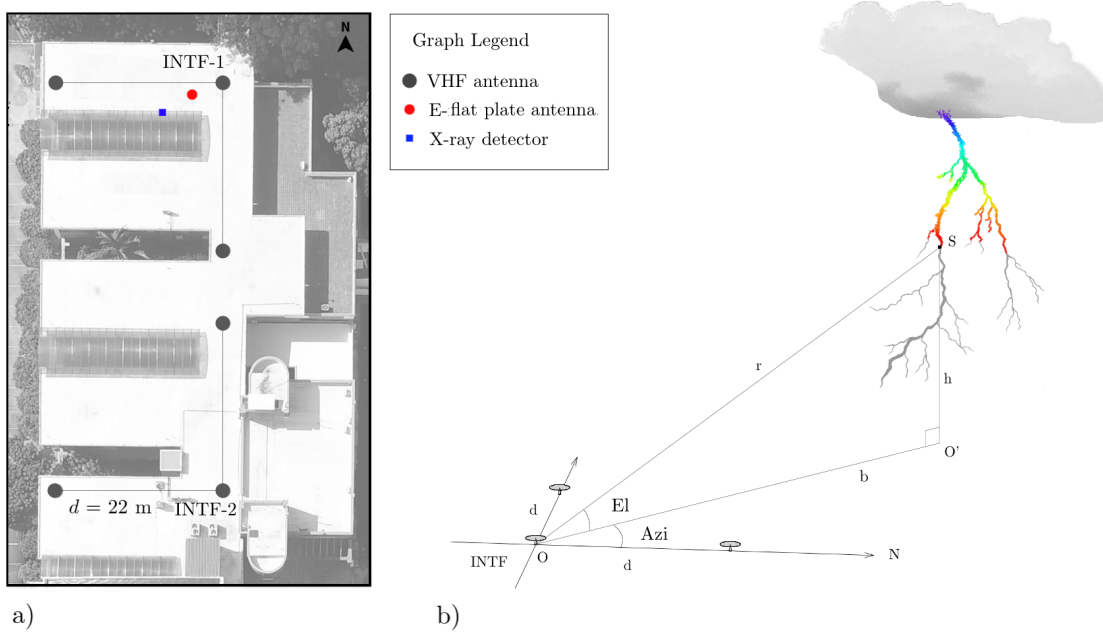


Figure 3.1: a) Instrumentation deployment on the UIS roof in Barrancabermeja (Colombia). Two lightning interferometers (INTF), a flat plate antenna for E-field measurements and an X-ray detector. b) Conceptual scheme and basic geometry of the lightning interferometer. A single interferometer provides a 2D imaging of the lightning in angular coordinates: elevation and azimuth.

3.4.1 VHF Broadband Interferometry System

Lightning discharges emit electromagnetic radiation over a broad range of the electromagnetic spectrum from extremely low frequency (ELF) to gamma-ray energy. In particular, in the VHF band (30-300 MHz) the nature of this emission is characterized by pulses of variable duration from some nanoseconds to a few microseconds. Due to their short duration, it is possible to consider, in first approximation, these pulses as stationary point sources. This assumption allows to locate the VHF sources evaluating the different time-of-arrival (TOA) or the phase difference of the electromagnetic waves detected by a system of antennas.

A VHF broadband lightning interferometer is an instrument that allows to map these VHF sources with an interferometric technique called generalized cross-correlation. Computing the geometric delay δt_{ij} between pairs of antennas with baseline d , it is possible to determine the direction of the point source through two angles: azimuth and elevation.

$$\begin{aligned}
 Azi &= \arctan \left(\frac{\delta t_{12}}{\delta t_{13}} \right) \\
 El &= \arccos \left(\frac{c}{d} \sqrt{\delta t_{12}^2 + \delta t_{13}^2} \right)
 \end{aligned}
 \tag{3.4.1}$$

An illustration with the basic geometry of the lightning interferometer is depicted in Fig.3.1.b).

An excellent description of this kind of instrument and the processing technique was presented by the New Mexico Tech researchers (Stock et al., 2014). Our system and processing technique is clearly inspired by their work and we refer further details on the overall operation of the interferometer to their report (Stock et al., 2014).

Two almost identical interferometers were built and developed in order to lead this investigation. Each interferometer consists of three antennas (aluminum disks of radius 20 cm) deployed along two orthogonal baselines ($d = 22$ m). The antenna's output signal is connected to a bandpass-filter (20-80 MHz) and then preamplified. All the antennas are connected using three identical high-quality coaxial cables ($l = 30$ m) to the acquisition system. The hardware of the acquisition system is primarily made by a digitizer and a workstation with sufficient CPU and memory requirements. The digitizer board used is the *GaGe Razor Express 1604*: 4 channel with 16-bit of resolution and 200MS/s of sampling rate and 8GB of memory. In order to maximize the chance to record interesting events, we developed the acquisition system software to get a *continuous recording* in streaming mode, filling a circular buffer in the RAM memory. We set our acquisition time duration at 2.5 s with 0.5 s of pre-trigger and less than 20 s of dead time after the triggered event.

Both interferometers were online and could be turned on remotely when a storm was approaching. Once activated, the acquisition system can be triggered by an E-field flat plate antenna installed nearby. The flat-plate antenna measures the environmental electric field along the vertical axis. In order to study the high-energy emissions, we were interested in close lightning CG strokes in a 10 km area. For this reason, the gain of the antenna was set properly to avoid saturation and the trigger threshold was adjusted to avoid to collect too remote events. The nominal calibration of the antenna is 16 kV/m on output volt with a time-constant of 1 s. The E-field signal was acquired in the 4th channel of the GaGe digitizer and by a Picoscope PS4424 to

synchronize the high-energy detector output with the VHF signals (further details in 2.2).

In the data processing, we applied a window-based cross-correlation method in frequency domain, with up-sampling and parabolic interpolation of the cross-correlation peak. The window length was set to 128 samples (~ 640 ns) with a sliding step of a single sample. To mitigate the effect of the strong window overlapping, a clustering algorithm was applied. We selected all the compatible values within 1 nanosecond and then averaged them together. Several thresholds were applied to improve the accuracy and the noise reduction: an amplitude threshold of the cross-correlation peak of 0.8, a threshold on the closure parameter of 0.6 ns and a minimum size of the cluster of 8 windows. Further details on the data processing and especially a discussion on the imaging efficiency are available in Supporting Information.

3.4.2 High-energy detector

The high-energy detector was installed nearby the INTF-1 (Fig.3.1.a) and it is composed of a NaI(Tl) cylindrical scintillator 76×76 mm (Scionix: type 76B76/3M-E2-X2) with a photomultiplier tube (PMT). The detector contained a voltage divider and a preamplifier in a magnetic shielded housing and the scintillator is enveloped in an aluminum body (thickness 0.5 mm). The nominal decay constant is 0.23 ms and the rise time $0.5 \mu s$, in good agreement with measured values. The detector was calibrated in energy at the nuclear physics laboratory in the Physics department at the Polytechnic University of Catalonia (UPC) with a ^{137}Cs and a ^{60}Co radioactive sources. The linear calibration in the range (0 - 1332 keV) provided a scale factor of $m = 4.63 \pm 0.02$ keV/mV. This calibration was used, as well, at higher energy assuming a linear response. The output signal was acquired by a Picoscope PS4424 with 12-bit resolution and a sampling rate of 10 MS/s and triggered by the E-field flat plate antenna. Therefore, the acquisition system has two different digitizers with two different sampling rates: The GaGe Board with 4 channels at 200MS/s (3 VHF antennas, E-field flat plate antenna) and the Picoscope 4 channels at 10 MS/s (E-field flat plate antenna, high-energy detector, GPS signal). The E-field signal provides the trigger of both acquisition system and allows an accurate synchronization ($\sim 0.1 \mu s$) during the post-processing phase. Other systematic instrumental uncertainties were evaluated, all of them are dominated by the rise time of the detector and the synchronization accuracy.

From the signal processing, two relevant quantities are estimated: the X-ray energy and the time-of-arrival t_0 . The energy is evaluated by computing the ΔV of the signal at the pulse rise and then using the calibration factor. This method underestimates the energy when the time interval between two successive pulses is less than the decay time (Bolic et al., 2009). In contrast, an energy overestimation occurs when it is not possible to resolve multiple photons. The resolution to exclude the photon pile-up is dominated by the rise time $\delta t_{rt} \sim 0.5 \mu s$. Both cases are very common in the physical phenomenon investigated; therefore, with our instrumentation, a very accurate measurement of the energy is out of our scope. On the other hand, an accurate evaluation of the t_0 is crucial for the discussion of the results. For this reason, we applied an algorithm to compute the t_0 using a linear interpolation of the rise time (further details are available in the Supporting Information), this simple procedure ensures a good accuracy and objectivity of the results. Another relevant observation concerns the environmental background. The probability of observing k background pulses in a given time interval Δt can be estimated using the Poisson distribution (e.g Tran et al., 2019):

$$P(k, \Delta t) = \frac{(\lambda \Delta t)^k e^{-\lambda \Delta t}}{k!} \quad (3.4.2)$$

where λ is the average rate of background events and Δt is expressed in milliseconds. We evaluated λ in the field during the campaign and we estimated a mean value of $\lambda = 0.20 \pm 0.05$ events/ms, almost the double of the Mallick et al. (2012) measurements. For example, the probability to have more than 2 background events in the last millisecond before a lightning return stroke is $P(k > 2, 1) \approx 0.001$. Therefore, when a X-ray burst is observed, there is no doubt that those emissions can be related to lightning activity. On the other hand, a single pulse emission has to be evaluated more carefully considering the probability of a false coincidence with lightning activity. (e.g. the chance to have a background pulse in 1 ms before the return stroke is $P(1, 1) \approx 0.18$ and in 0.1 ms is $P(1, 0.1) \approx 0.02$).

3.4.3 LINET

Complementary data and information to our measurements were provided by the Colombian Total Lightning Detection Network, operated by *Keraunos* company since 2011. This network is composed of nineteen low frequency (VLF/LF) sensors of LINET type (Betz et al., 2009) deployed with baselines of approximately 100 km. Further details on this network can be found in Aranguren et al. (2017).

3.5 Observations and Analysis

During the campaign period, nine thunderstorms were observed and in four of them high-energy radiation was detected. More than 200 lightning events (about 65% CG and 35% IC) triggered the acquisition system and in particular, seven X-ray bursts were detected, of which five intense bursts (with at least ten X-ray pulses) and other fifteen lightning events with at least a single X-ray pulse in the last 0.1 ms before the returned stroke were recorded. In order to present the observations, we decided to give an overview of the overall data to contextualize the measurements and then present in detail the most interesting cases.

3.5.1 Overall data analysis

In this paper, an “X-ray burst” is defined as a sequence of three or more X-ray pulses related with the same lightning event. Each X-ray pulse is not necessarily a single photon and the choice of three as the minimum size of an X-ray burst is discussed in section 2.2. In the literature, it is equally common to define an X-ray burst as the sub-microsecond emissions of multiple energetic photons (e.g. Dwyer et al., 2005). We call “X-ray pulses” the detection of these emissions, as they appear in our measurements (e.g. Mallick et al., 2012).

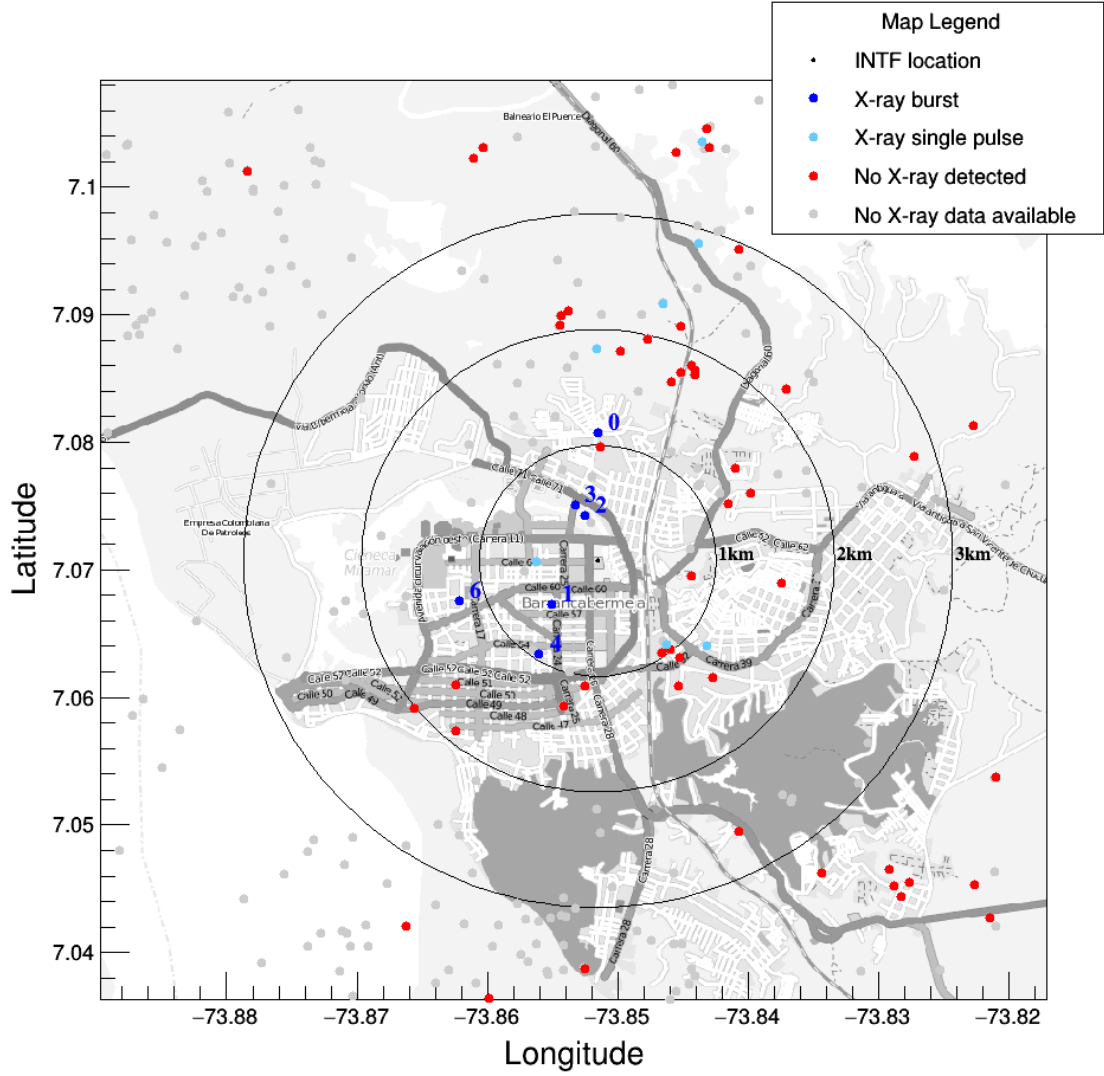


Figure 3.2: The map shows the LINET lightning location recorded during the observational campaign at the Universidad Industrial de Santander (UIS) campus of Barancabermeja (Colombia) in autumn 2019. The map is centered in the INTF location. Lightning events observed by the INTF in coincidence with an X-ray burst were colored in blue, lightning events observed by the INTF without X-ray detection were colored in red, lightning events not recorded were colored in gray.

The observed events can be divided into four categories: 1) Events where an X-ray burst was observed; 2) Events where one or two X-ray pulses were observed (we call these events “single X-ray pulses” as discussed in section 2.2.); 3) Events in which no X-ray emissions were observed; 4) Events that did not trigger our data acquisition system, but they were recorded by LINET.

In Figure 3.2 we combined the high-energy detections with the lightning locations provided by LINET. The map is centered in the INTF-1 system of reference and allows to evaluate in particular the radial distance between our detection system and the lightning strokes. It can be observed that all the X-ray bursts detected are within an area delimited by a radius of about 1.2 km, and the majority of the events observed in this area have produced detectable high-energy radiation.

Table 3.1 summarizes the overall X-ray bursts data combining the high-energy measurements with the LINET data. Seven X-ray bursts were observed, corresponding to a total of 84 X-ray pulses. Unfortunately, for some events, we only have some partial data, due to the failure of the trigger in the acquisition system or to the detection efficiency of the lightning network.

Table 3.1: X-ray bursts overall data. Distance, current, and timestamp are provided by Keraunos LINET lightning location network.

| X-ray burst ID | Timestamp (UTC) | Distance | Current | Nr. of X-rays |
|----------------|-------------------------|----------|----------|---------------|
| 0 ^a | 2019-11-11 06:21:52.193 | 1.10 km | -55.5 kA | 3 |
| 1 | 2019-11-11 06:38:16.378 | 0.55 km | -36.6 kA | 23 |
| 2 | 2019-11-11 06:39:06.518 | 0.40 km | -6.8 kA | 22 |
| 3 | 2019-11-11 06:53:03.843 | 0.52 km | -23.3 kA | 4 |
| 4 | 2019-11-11 06:59:04.632 | 0.95 km | -18.4 kA | 10 |
| 5 ^b | 2019-11-11 07:04:32.823 | - km | - kA | 11 |
| 6 | 2019-12-31 08:18:23.579 | 1.22 km | -43.8 kA | 11 |

^a INTF data not available.

^b LINET data not available. GPS timestamp

Figure 3.3 shows the energy distribution and the time distribution of the X-ray pulses belonging to the X-ray bursts. The energy distribution has the most frequent count in the range 100-150 keV and the median value is approximately 280 keV. It is possible to observe that the vast majority of the X-ray pulses has an energy below 1 MeV. Higher values of energy have been observed from 2 MeV up to 8 MeV, but these results have to be discussed. Although energies of some MeV can actually be achieved and therefore observed, it is important to underline that our instrument has a rise time of 0.5 μ s and therefore, as explained in section 2.2, we cannot exclude that some of these values may be due to a pile-up phenomenon caused by the detection of multiple

photons (Dwyer, 2004). This energy spectrum is consistent with earlier lightning observations (e.g. Dwyer et al., 2004; Arabshahi et al., 2015) and it is softer than a typical TGF spectra detected from space (e.g. Østgaard et al., 2012; Marisaldi et al., 2014). The time distribution shows a clear increase in X-ray detection approaching the return stroke (RS), as previously observed by Mallick et al. (2012). Unfortunately, with our instrumentation, we are not able to say if this effect is mainly due to the leaders' approach to the ground or due to the decreasing distance between leaders and the high-energy detector. We cannot separate efficiently the two contributions. The maximum duration of the observed X-ray bursts was about $900 \mu s$ and the mean duration $\sim 600 \mu s$. Taking into account the time distribution of all X-ray pulses belonging to the X-ray bursts observed, the median value was $150 \mu s$ before the return stroke.

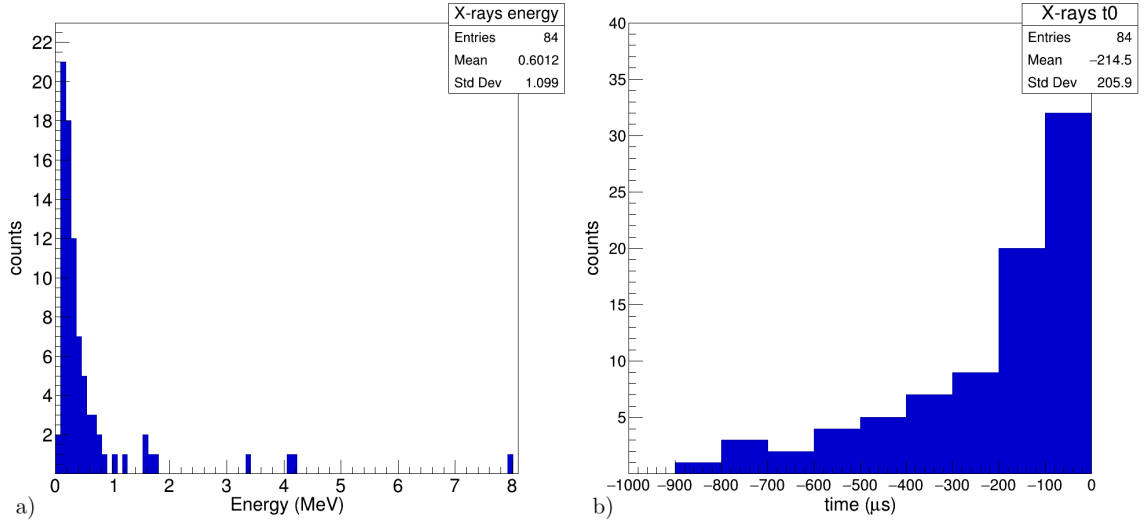


Figure 3.3: a) Energy distribution of the X-ray detected during the bursts observed. The highest energy values can be real or overestimated due to a pile-up effect. The nominal time resolution to excluding pile-up is $0.5 \mu s$. b) Time distribution of the X-ray pulses detected during the bursts observed in negative downward leaders before the return stroke.

3.5.2 Negative Downward Leaders: 2019-11-11 06:39:06

On 11 November 2019, a tropical thunderstorm passed through Barrancabermeja during the night and several lightning events were recorded. Six X-ray bursts and five X-ray single pulses were detected from lightning activity. In this section, we

present the most energetic burst associated with a negative downward leader and subsequently a dart leader event that occurred 4 ms later.

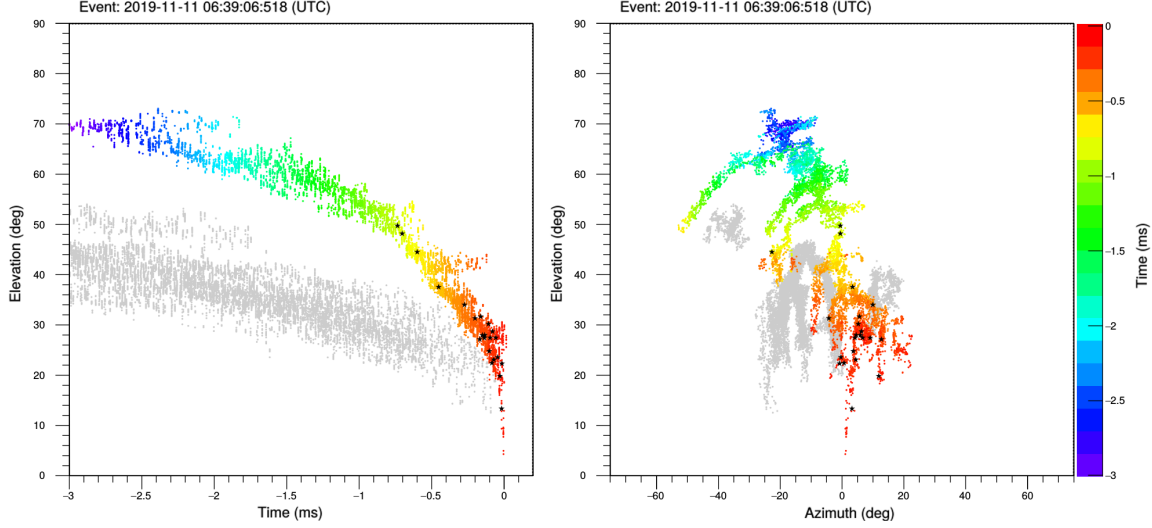


Figure 3.4: Negative downward leader associated with the detection of an X-ray burst. The lightning map is obtained with the VHF broadband lightning interferometer INTF-1. The image is colored by time and the most likely locations of the X-ray sources is marked with black stars. The gray image is related to another simultaneous leader branch likely farther away from the interferometer.

The first relevant observation is that all the X-ray bursts detected were associated with negative downward leaders with several branches. In particular, in this case, it is possible to distinguish two main leader branches: the first one at a lower elevation, probably farther away from the INTF or with lower speed, and the second one at a higher elevation probably closer to the INTF or faster. This ambiguity is due to the two-dimensional imaging of a three-dimensional development of a lightning event. We will focus especially on this second main leader branch because the high-energy radiation detected seems to be associated with its propagation.

Figure 3.4 and Figure 3.5 show the negative downward leader evolution during the last 3 ms before the RS. The lightning map is 2D and it is described by the angular coordinates: elevation and azimuth defined in section 2.1 and in Figure 3.1.b). The timestamp in UTC time is the proper time of the RS detected by LINET. In order to better appreciate the evolution in time, especially when the X-ray emissions were detected, we provide an animation of Figure 3.4 in the supplementary material.

For this event, it was possible to obtain a relatively accurate location of the radial distance comparing the LINET location with pictures and satellite images of the

struck area and likely this distance is 430 – 450 m, two high-buildings are the most likely striking point. In Figure 3.5 it is possible to appreciate the detailed evolution of the downward leader and the most likely location of the X-ray sources.

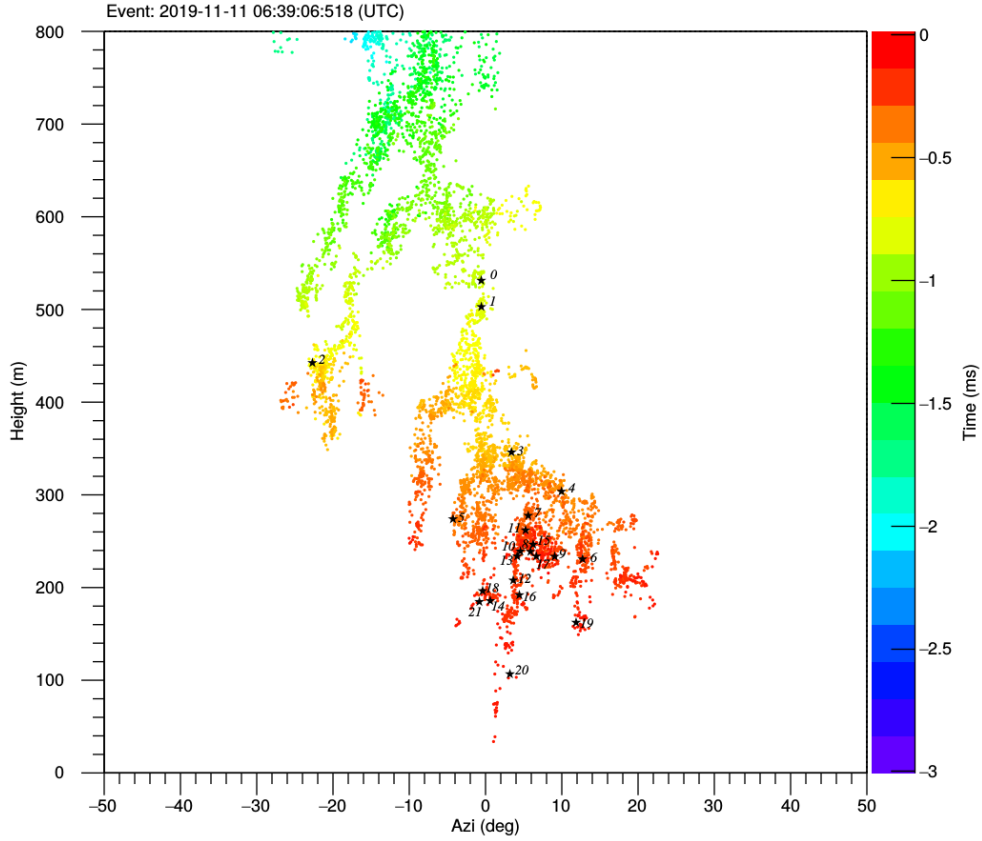


Figure 3.5: Negative downward leader associated with the detection of an X-ray burst. The lightning map is obtained with the VHF broadband lightning interferometer INTF-1. The image is colored by time and the most likely location of the X-ray sources is marked with black stars.

In order to describe the procedure by which the most likely X-ray sources were located, a few comments on the E-field signal, the X-ray signal and VHF sources are needed.

Figure 3.6.a) shows the output signals of the flat plate antenna and the high-energy detector in the last 1 ms before the RS. The electric field increases due to the approaching of the downward leader to the ground until the dramatic drop at the RS. The high-energy detector signal shows the overlap of the X-ray pulses due to the long

decay constant of the detector. This pile-up effect can be resolved for time intervals greater than $0.5 \mu s$. The time-of-arrival t_0 of each X-ray pulse was evaluated and numbered.

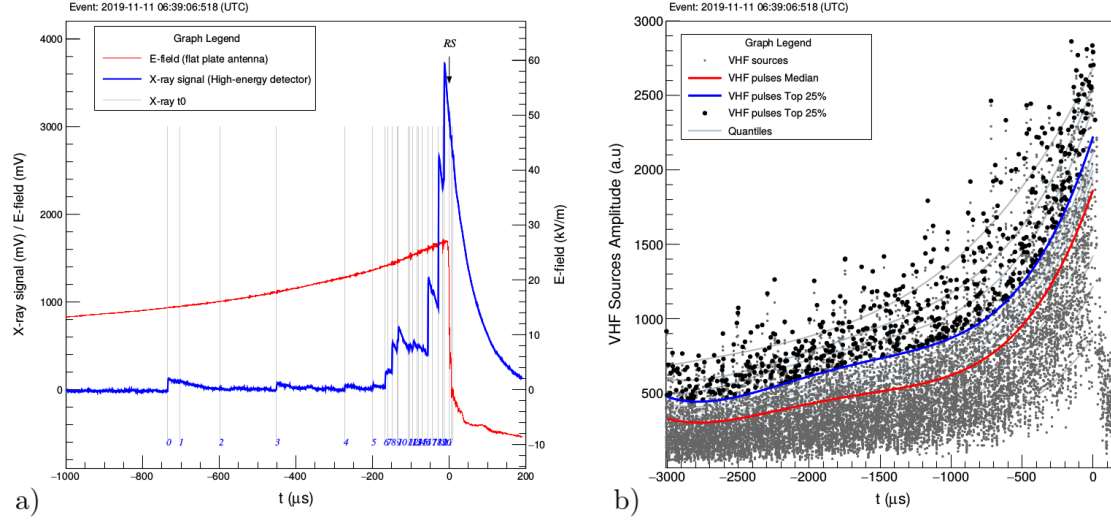


Figure 3.6: a) Electric field from the flat plate antenna and high-energy detector signal in the last 1 ms before the return stroke. b) VHF sources and VHF pulses amplitude in the last 3 ms before the return stroke. The red line and the blue line represent the VHF pulses median and the third quartile respectively, which define the most intense VHF pulses.

Figure 3.6 .b) allows us to clarify the terminology used in this work. We use the term “VHF sources” to indicate the set of all solutions provided by the interferometer data processing.

In general, the VHF sources detected by a broadband lightning interferometer can be due to continuously radiating or impulsive events (Stock et al. 2014). We are especially interested in a subset of these VHF sources that we call “most intense VHF pulses”. We define this subset considering a local maximum condition and a threshold condition on the VHF amplitude. The local maximum condition on the amplitude, generally defines a “VHF pulse”, instead, the threshold condition on the amplitude, based on the median or the third quartile (top 25%), allows to define in a robust way the “most intense VHF pulses”. More details are available in the Supporting Information.

With only one high-energy detector, it was not possible to obtain an independent measurement to locate the X-ray sources. Therefore, our initial assumption was

to associate each X-ray t_0 with the closest VHF sources in time domain and infer the X-ray source location from the associated VHF source location. Following this procedure, we realized that several VHF sources could be associated with the same X-ray in our uncertainty range, dominated by the rise time of the high-energy detector. For this reason, in order to express this uncertainty in the location of the high-energy radiation, a good strategy consists in plot all the possible X-ray sources in a time interval δt with respect to X-ray t_0 . We have chosen $\delta t = \pm 1 \mu s$ because it is the double of our uncertainty range, and assuming a normal random distribution, it would correspond to a 95% of confidence interval.

Figure 3.7.a) shows the density plot of VHF sources in this interval; it is probably the most effective way to show all the possible locations of the X-rays detected together with their location uncertainty. Despite that, this figure is integrated over a long time compared to the single X-ray emission and it is not allow to evaluate the location uncertainty of each X-ray pulse detect. Therefore, we provide in Figure 3.7 two example of the location uncertainty related to the X-ray pulses number 18 and 19 (all the other cases can be find in supplementary material). Figure 3.7.b) shows an unique location of the X-ray source, instead, Figure 3.7.c) shows an ambiguous location.

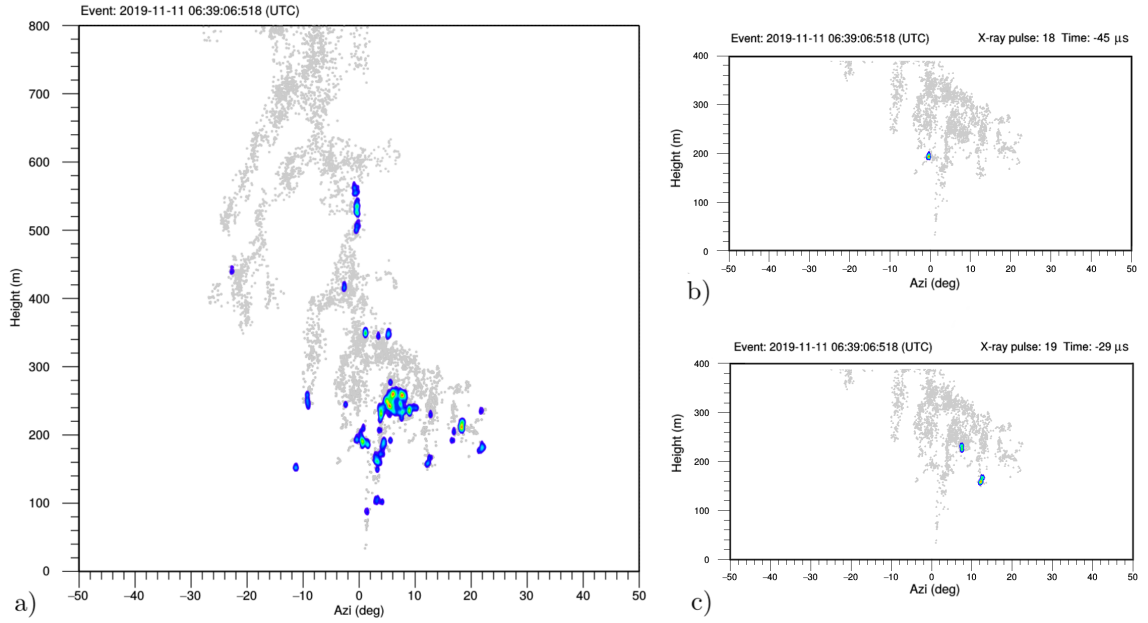


Figure 3.7: a) Density plot of all the VHF sources that can be related to the high-energy emission in a time interval δt of $\pm 1 \mu s$ with respect to all X-ray t_0 . b) Unique location of X-ray pulse 18. c) Ambiguous location of X-ray pulse 19.

Despite this occasional ambiguity on the X-ray source location, we were not sure that

the VHF emissions and the high-energy radiation were related until we observed a clear correspondence between the X-ray t_0 and the most intense VHF pulses.

Temporal correspondence between the high-energy emissions and the most intense VHF pulses

In this section, we present the evidence of a temporal correspondence between the high-energy emissions and the most intense VHF pulses. We compare the time-of-arrival of the high-energy emissions t_0 , computed by the algorithm described in section 2.2, with the time-of-arrival of the VHF sources, computed by the interferometer. Further details on the data processing and the quantitative definition of the the VHF source amplitude are described in the Supporting Information .

Figure 3.8 shows a clear example of this temporal correspondence. On the background, it is possible to observe the VHF signal of the central antenna (gray line). The black spline connects all the VHF sources obtained by the INTF processing and in particular, the most intense VHF pulses marked with black dots. The output signal of the high-energy detector and the dE/dt signal are respectively the blue and the red line.

It is possible to observe how the black spline presents several peaks, which correspond to the most intense VHF pulses. Superimposing a vertical reference related with t_0 (blue lines) emerges the correspondence with VHF peaks. A blue star mark represents the matching.

As already mentioned, there are several VHF sources that could be associated with the same X-ray pulse in our uncertainty range, but usually only one intense VHF pulse. Nonetheless, to prove the goodness of this correspondence, we performed two complementary analysis.

The first test consists in computing the discrete cross-correlation between the X-ray time-of-arrivals t_0 and the VHF pulses timestamps, considering the temporal uncertainty of $\pm 0.5\mu s$ as the width of the t_0 pulses. The result shows a correlation peak compatible with zero, therefore, we can state that high-energy pulses and VHF pulses are temporally correlated. Furthermore, following a similar approach we computed the cross-correlation between the X-ray time-of-arrivals t_0 and the most intense VHF pulses (top 25 %) and we compared it with the the cross-correlation with the other VHF pulses (bottom 75%). Figure 3.9.a) shows that there is a clear correlation between the X-ray time-of-arrivals t_0 and the most intense VHF pulses, instead there is no correlation with VHF pulses with lower amplitude.

The second test we performed is a Monte Carlo simulation to evaluate the p-value in the case of study illustrated in Figure 3.8. We considered all the most intense VHF Pulses (top 50%) and we simulated the X-ray t_0^* assuming a random uniform

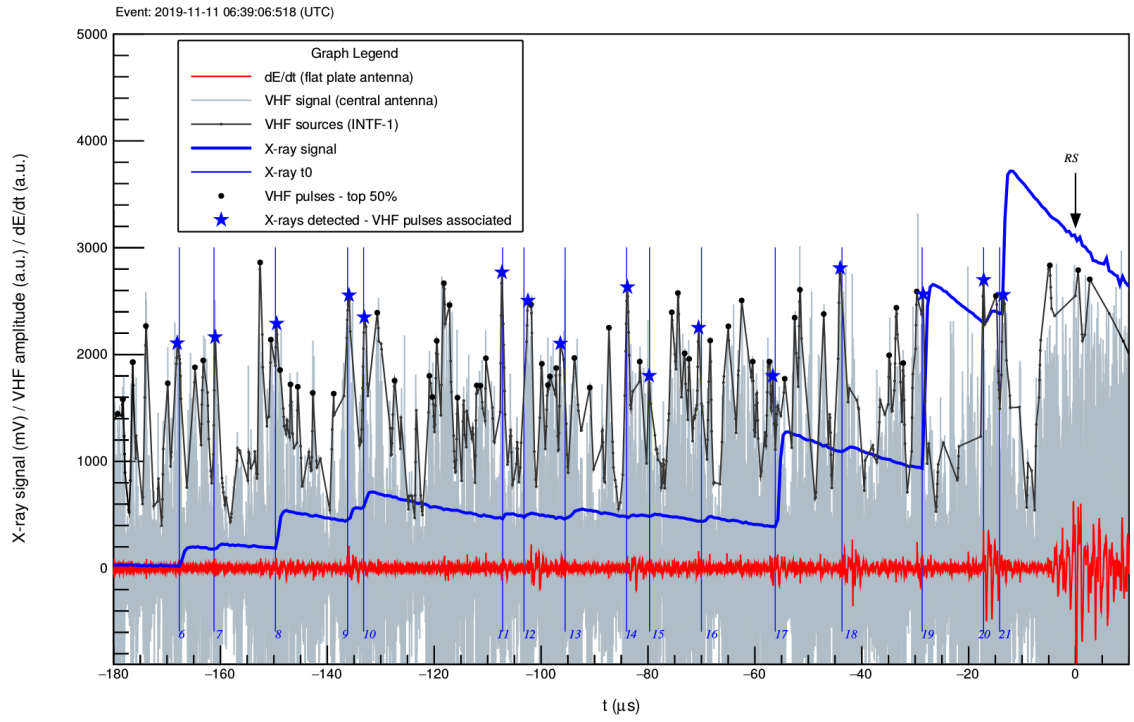


Figure 3.8: Zoom of the most interesting time interval of Event 2019-11-11 06:39:06. The graph highlights the temporal correspondence between the X-ray pulses (blue lines and labels) and the most intense VHF pulses. The association is marked with blue stars.

distribution in the time range $[-180 : 0] \mu s$, then we evaluated the absolute deviation $\Delta t = |t_0^* - t_{VHF}|$. The probability to have a single random correspondence is actually quite high $p(k = 1, \Delta t < 0.5) < 0.366$, but the probability to have several random correspondences decrease rapidly.

We evaluated the average absolute deviation for 16 correspondences. The probability density function is shown in Figure 3.9 b). The probability for a random correspondence in the uncertainty range is less than 0.4% but the p-value of our event is lower than 0.02% and if we consider the average VHF amplitude as well, the probability to have a random association with overall higher VHF amplitude is absolutely low ($p < 2.6 \times 10^{-6}$).

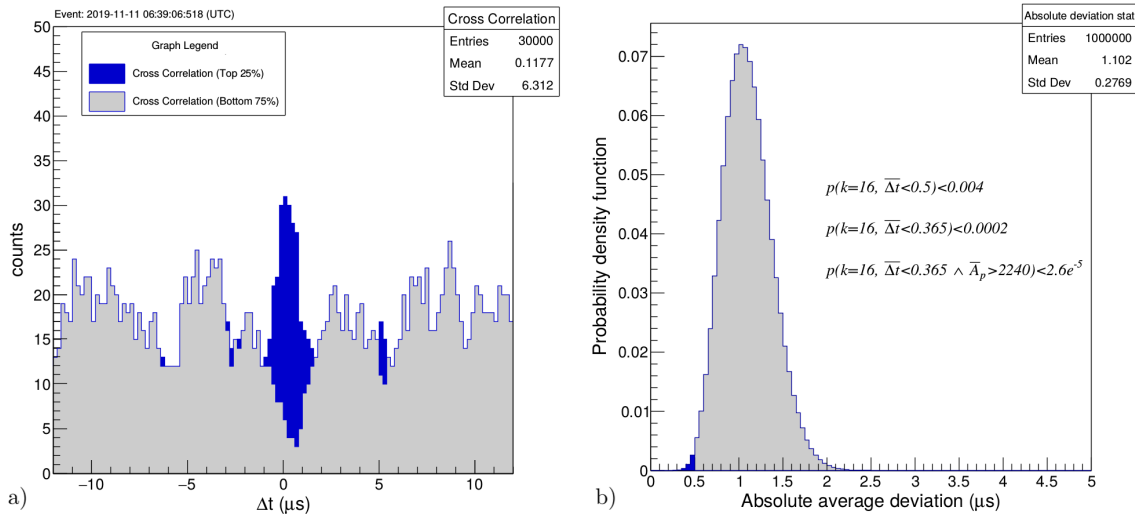


Figure 3.9: a) Cross-correlation between X-ray t_0 and the most intense VHF pulses (top 25%), and between the less intense VHF pulses (bottom 75%). In both cases we considered an uncertainty of $\pm 0.5 \mu s$ on t_0 . b) Probability density function obtained from a Monte Carlo simulation to evaluate the p-value, in the case of study presented in Figure 8.

After that, we evaluated the deviation $\Delta t = t_0 - t_{VHF}$ of the measured X-ray t_0 , where t_{VHF} is the time related to the VHF pulse associated. This quantity Δt was computed for all the X-ray bursts observed and shows that both processes could be considered simultaneous within an accuracy of $0.5 \mu s$ (see Figure 3.10.a).

Despite the definition of the “most intense VHF pulses” provided is generally clear, we studied the relation with the VHF amplitude more thoroughly. We computed the 20-quantiles in all the X-ray bursts observed in order to compare the relative magnitude of the VHF amplitude of the pulses associated with the high-energy emissions.

The overall distribution is shown in Figure 3.10.b), the most intense VHF pulses (top

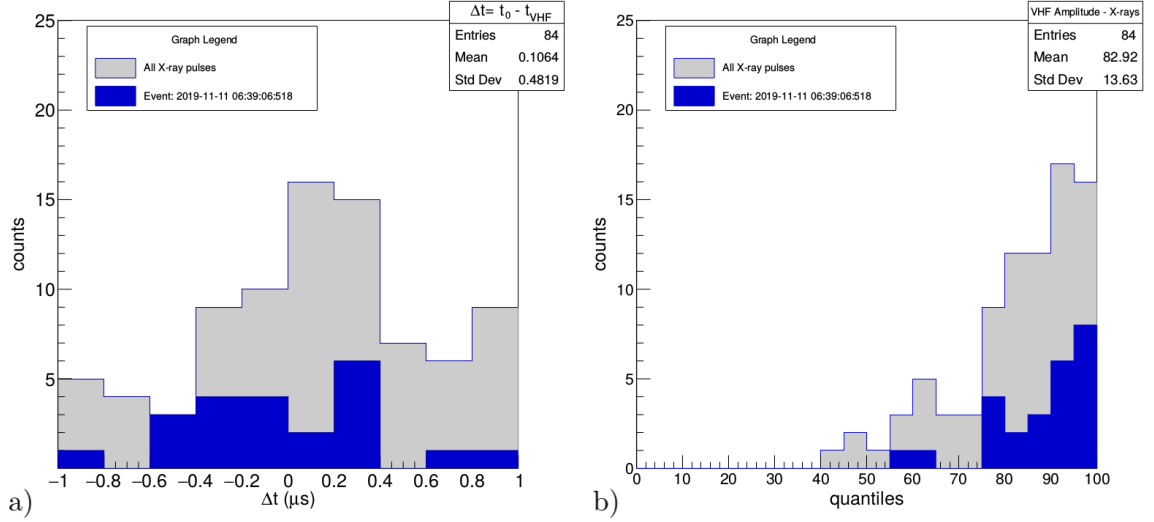


Figure 3.10: a) Time difference between the X-ray t_0 and the VHF pulses associated. This quantity was evaluated in all X-ray bursts (gray) and in the X-ray burst 2019-11-11 06:39:06 (blue). b) Distribution of the VHF pulses associated with X-ray emissions. The VHF amplitude is expressed in quantiles to allow comparison between different events.

50%) correspond to more than 96% and the top 25% correspond to the 82% of the distribution.

In conclusion, we can state that a temporal correspondence between the high-energy emissions and the most intense VHF pulses was observed and it is statically significant. This temporal correlation allows a more accurate location of the X-ray sources and could suggest a shared production mechanism.

It is relevant to note that also the peaks of the electric field derivative (dE/dt) are in correspondence of the X-rays pulses, as observed for the first time by Dwyer et al. (2005) and with the majority of the VHF pulses. This “triple” correlation between high-energy radiation, VHF pulses and electric field derivative dE/dt is discussed in the section 4.

High-energy emissions and leader speed

In this section we investigate the relation between the high-energy radiation and the VHF leader speed. The goal of these measurements is not intended to provide an accurate absolute value of the leader speed, but rather to investigate whether it is possible to observe some correlation or change in speed in correspondence with the

high-energy emission. Assuming a good accuracy in the radial distance (≈ 450 m) and a leader development, essentially vertical, it is possible to quantify the 2D speed of the leader.

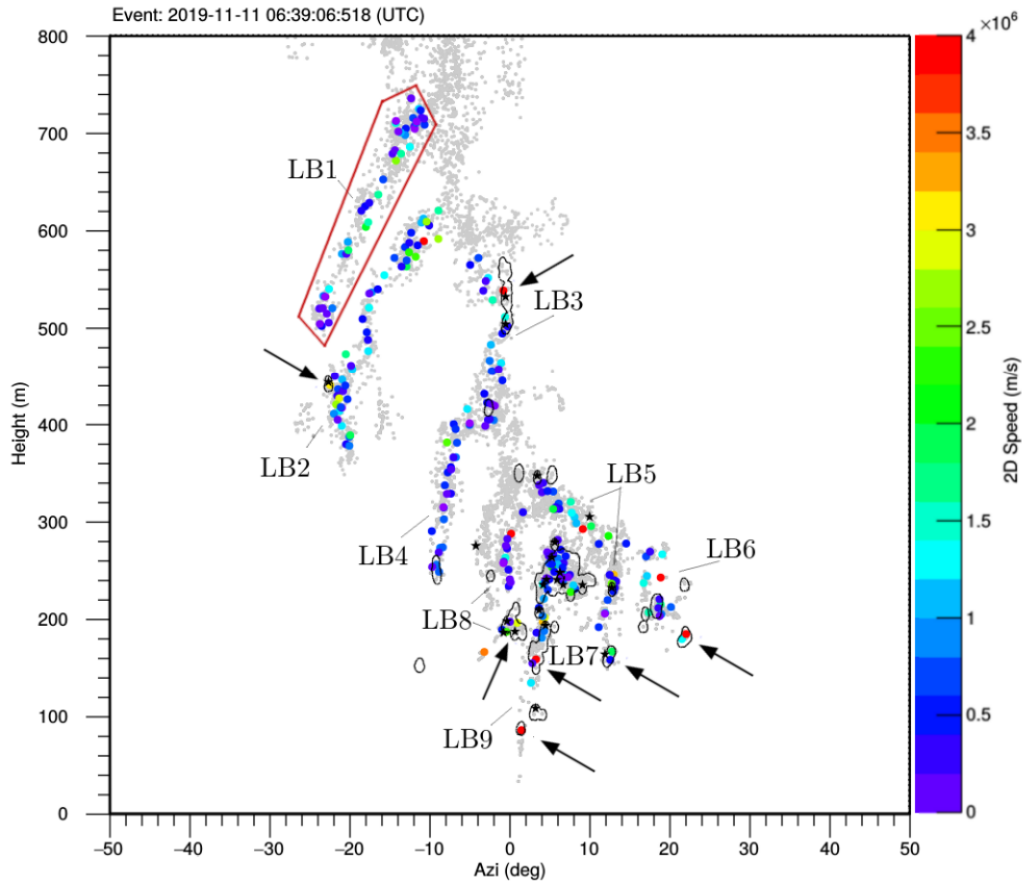


Figure 3.11: a) Analysis of the leader speed in relation with the high-energy radiation. Nine leader branches were examined and the 2D speed was calculated averaging all the VHF sources in a time interval of $10 \mu s$. The regions of interest are indicated by arrows and delimited by a contour plot, the X-ray sources are marked with black stars. Speed values greater than 4.0×10^6 m/s were saturated to this maximum value.

The attempt to calculate the speed between two consecutive VHF sources has failed, this procedure produces unreliable values of the leader speed. The reason for that could be due to the fluctuations or likely because the VHF pulses measured by the INTF are associated with the streamers' propagation (and therefore, two consecutive streamers can be randomly directed and unrelated in terms of their propagation). To overcome this problem, we selected 9 leading branches (LBs) by visually separating the VHF sources through polygons in the 2D image and then we averaged the VHF sources together in a fixed time interval of $10 \mu s$.

Figure 3.11 shows the 2D speed of the selected branches, the areas of great interest are delimited by a border obtained from the previous density plot. To allow better visualization, it was decided to saturate speeds above 4.0×10^6 m/s, this threshold was chosen considering the overall speed distribution.

It seems possible to observe a variation in the 2D speed in correspondence with the X-ray emissions (see the arrows in Figure 3.11, e.g. LB2, LB3, LB5, LB8 and LB9). This speed variation can be identified by the color change, especially in the presence of red dots or warm colors, but it could also be due to multiple branching in the third dimension or in smaller scale, high streamer activity or simply random fluctuations. Therefore, although there is an indication of correspondence between the X-ray location and the 2D speed variation, such correlation is not strong enough to be statistically significant.

Despite the averaging procedure, several outliers, essentially due to fluctuations or secondary branching, compromise the measurement of the overall 2D speed of a single leader branch. For this reason, in order to get more reliable speed values for each single branch, we preferred to calculate them using an 1D linear fit (see Fig.3.12). We take advantage of the 2D imaging to select the branches and compute the 1D speed in both components (vertical and horizontal) and then obtain the 2D speed by combining both.

In conclusion, although we investigated the relation between the high-energy radiation and the VHF leader speed, we did not observe a clear correlation. It is possible to report that high-energy radiation was observed in negative downward leader propagation in the 2D speed range $0.4 - 1.2 \times 10^6$ m/s. Further implications are discussed in the section 4.

3.5.3 Dart Leader: 2019-11-11 06:39:06

After 4 ms from the previous negative downward leaders, we observed dart leader event with X-ray emissions. In Figure 3.13, it is possible to appreciate the development of the dart leader along the main channel of the previous event (in gray). Two

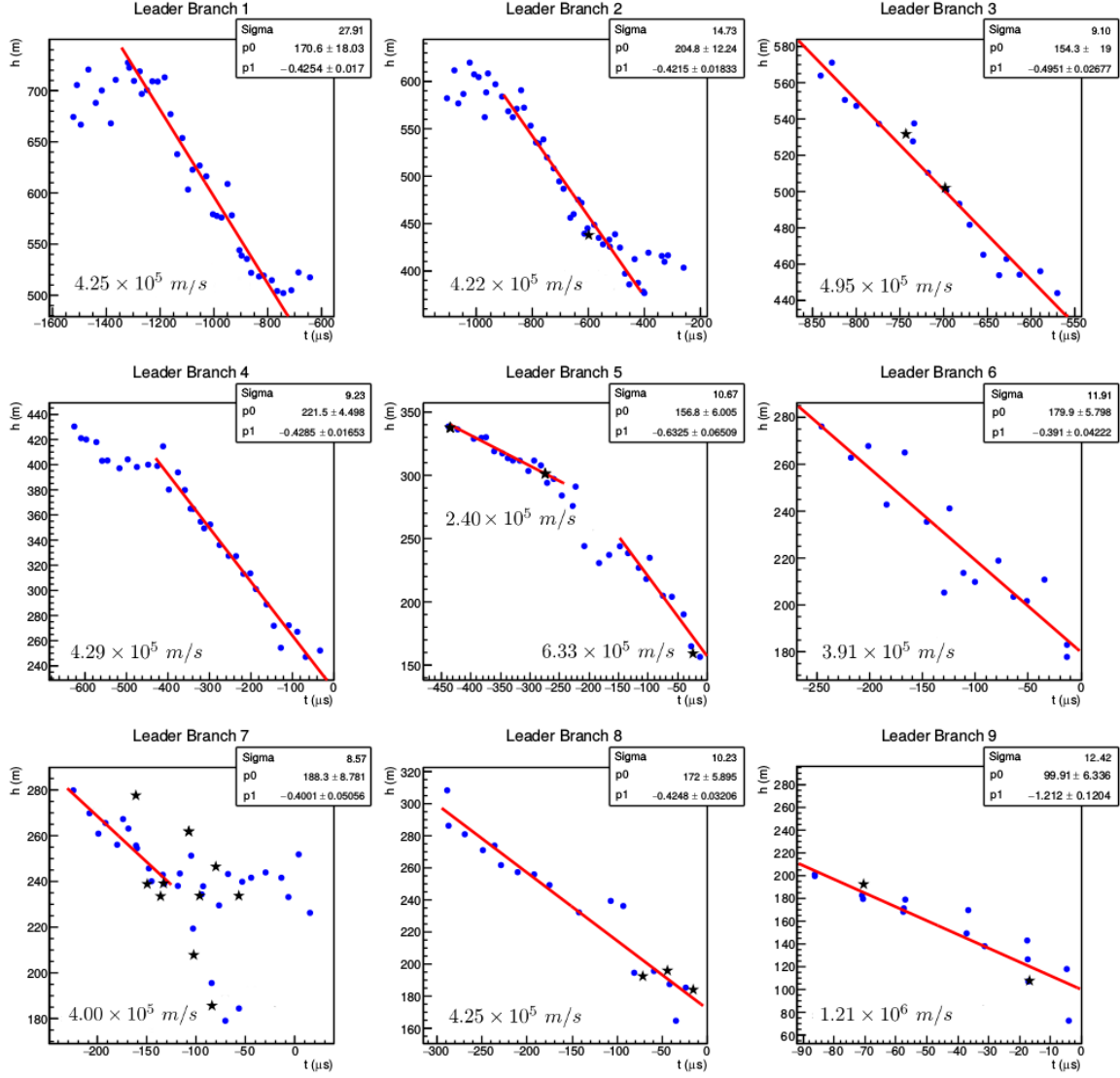


Figure 3.12: Collection of nine leader branches of the lightning event 2019-11-11 06:39:06:518 (UTC). The graphs show the VHF sources averaged in a time interval of $10 \mu s$. The height-time plot shows the 1D averaged leader speed computing the slope (p_1) of the linear fit. It is possible to appreciate the variation of the leader speed and secondary branching in the time domain. The likely sources of high-energy radiation are marked with black stars.

X-ray pulses were observed in coincidence, both with an energy of about 100 keV. The total duration of the event is about $100 \mu s$.

Figure 3.14 shows the vertical evolution of the dart leader during the last $50 \mu s$

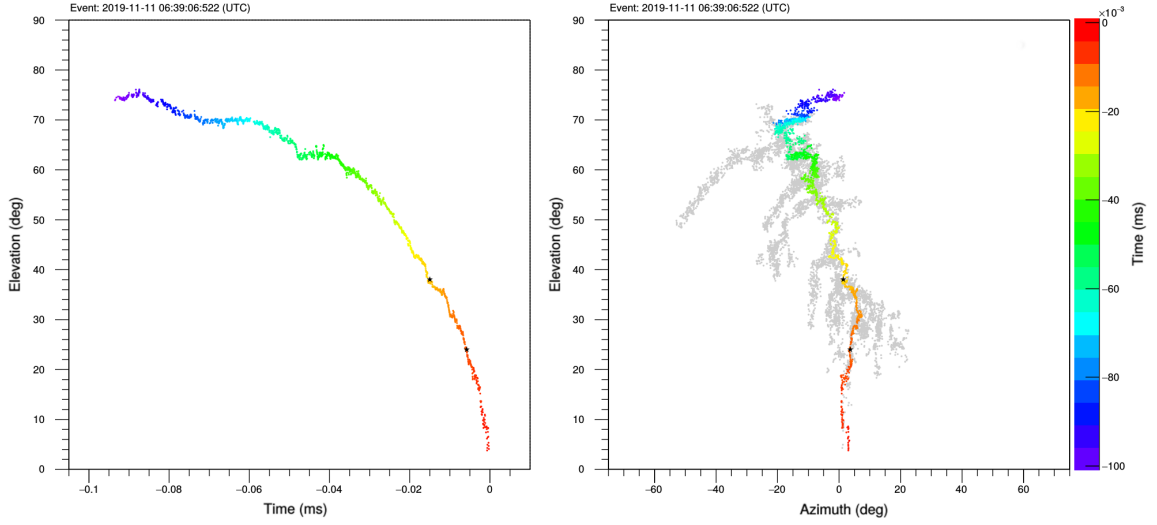


Figure 3.13: Dart leader associated with the detection of high-energy emissions. The lightning map is obtained with the VHF broadband lightning interferometer (INTF-1). The image is colored by time and the most likely location of the X-ray sources is marked with black stars.

before the return stroke. We used linear interpolation to calculate the 1D speed in both components (vertical and horizontal) to determine the 2D speed. The average speed seems constant for the last 800 m with a value of 2.0×10^7 m/s. We did not observe measurable increase of the speed in the proximity of the X-ray emissions. A strong VHF signature was observed, typical of dart leaders. The elapsed time between the VHF pulses is much less than the negative downward leaders. Further implications are discussed in the section 4.

3.5.4 Negative Downward Leaders: 2019-11-11 06:38:16

A similar analysis to the one described for the event 2019-11-11 06:39:06 is conducted on all observed X-ray bursts, but in less detail due to the larger uncertainty on the distance and a smaller number of X-rays detected. For completeness and further considerations, we briefly present another case of negative downward leaders: 2019-11-11 06:38:16.

Figure 3.15.a) shows the location of the high-energy sources with their uncertainty expressed by the density plot. This case is characterized by three simultaneous distinct leaders' main branches all around our INTF station (note azimuth scale). The duration of the X-ray burst is about 1 ms with 23 X-ray single pulses detected. We

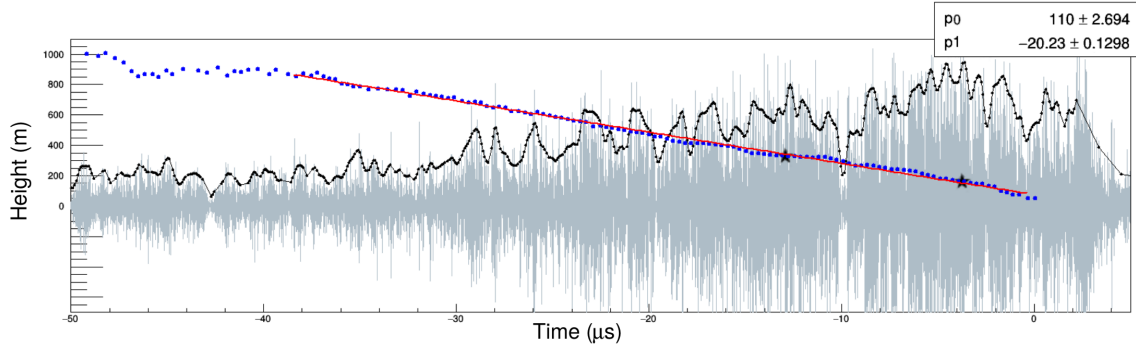


Figure 3.14: Analysis of the 1D-speed of the dart leader. The graph shows in background the VHF signal and in black dot line the VHF amplitude of the sources. The time evolution of the VHF source height is depicted with blue dots and the black star markers represent the most likely height of the X-ray sources. Finally, the linear interpolation of the speed is superimposed.

observed many X-ray sources in correspondence with the unconnected leader tips.

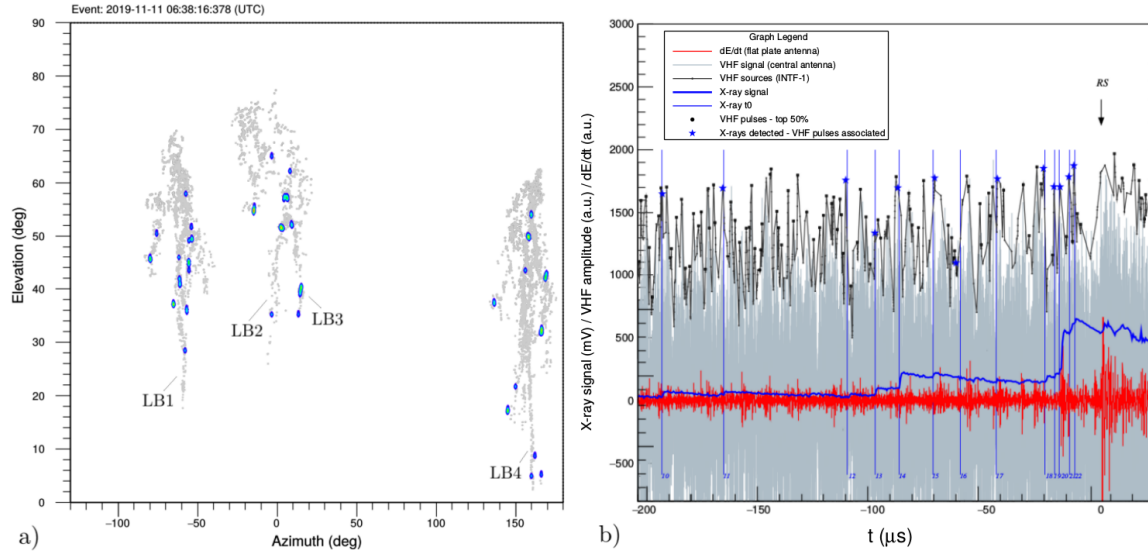


Figure 3.15: Negative downward leaders event associated with the detection of an X-ray burst. a) Density plot of all the VHF sources that could be related to the high-energy emission in a time interval δt of $\pm 1 \mu s$ with respect to the X-ray t_0 . b) Temporal association between the X-ray pulses (blue lines and labels) and VHF amplitude peaks, the correspondence is marked with blue stars. Zoom of the last $200 \mu s$.

LINET provides a unique location for this event (likely related to LB4 the channel where the return stroke occurred), the approximate distance from the INTF station is 550 m. Assuming this value for all the LBs, we calculated the 2D speed: $0.8 - 1.0 \times 10^6$ m/s for LB1, LB2, LB3 and 1.2×10^6 m/s for LB4.

As a final remark, we would like to point out that an X-ray burst can have multiple sources belonging to different leader branches, that could be hundreds of meters apart. Therefore, an extensive origin of the X-ray burst should be considered, the same also in downward TGFs like those observed by Abbasi et al. (2019) and maybe, we hypothesize, in TGFs detected from space.

3.6 Discussion

In this study, we presented simultaneous measurements of high-energy radiation and lightning imaging provided by a VHF broadband interferometer. In comparison with other studies, the main advantage of this approach is to observe directly the lightning leaders propagation and measure in coincidence the high-energy radiation with sub-microsecond time accuracy. On the other hand, the main limitations of our setup are related to the use of a single high-energy detector and the partial information provided by the 2D imaging of the interferometer.

As previously discussed in section 3.1, a single detector does not allow to obtain an independent measurement to spatially locate the high-energy sources, while in other studies (Howard et al., 2008; Hill, 2012), it was possible to locate the high-energy sources directly using several detectors in 3D via TOA techniques. Despite this limitation, we observed a strong temporal correspondence between the X-ray detection and the most intense VHF pulses that can be used to locate the VHF sources associated with the high-energy radiation. The time difference between the X-ray detection and the VHF pulses is shown in Figure 3.10.a) and suggests the simultaneity of the two processes within a time interval comparable with our instrumental uncertainty $0.5 \mu s$. A similar time correspondence, between the high-energy radiation and the electric field derivative dE/dt , had already been observed by Dwyer et al. (2005) and associated with the leader step process. Howard et al. (2008) studied the co-location between the electric field change sources and the high-energy emissions. They observed that X-rays are emitted 0.1 to $1.3 \mu s$ after the dE/dt pulses at an average distance of 50 m. Instead, our observations show the location of the VHF sources (associated with the high-energy radiation) and not directly the high-energy sources.

The other significant limitation is due to the 2D imaging of the interferometer. In particular, two consequences derive from it: the lack of information on the distance of the source, which cannot be obtained directly from our measurements, and the

lack of information on the spatial direction of the leader branches. Without knowing the distance of the sources, it is not possible to estimate correctly the leader speed and the intensity of the high-energy sources. In addition, without knowing the direction of the leader branches, it is difficult to consider and discuss the beaming effect due to the orientation of the leaders. In order to overcome these limitations, we installed two interferometers (INTF-1 and INTF-2) for a limited period of time, but unfortunately, we did not observe any X-ray burst in coincidence with both interferometers. Therefore, we used LINET data to obtain the complementary information for our measurements, in particular the distance between the event and INTF-1 and the stroke peak current.

In spite of the limitations discussed, the images obtained with the VHF broadband interferometer allow to appreciate in detail the leader's development and to locate with good accuracy the VHF sources associated with the high-energy radiation. The bottleneck of our accuracy is due to the rise time $\sim 0.5 \mu s$ of the high-energy detector and secondarily the digitizer sampling rate. As explained in section 3.2, it is not particularly relevant to estimate the spatial accuracy of the high-energy sources location in terms of meter or degrees because in our temporal uncertainty multiple VHF sources can be associated with the same X-ray. For this reason, we selected the most intense VHF pulses in the interval δt of $\pm 1 \mu s$ and we represented our uncertainty in the density scatter plot (Figure 3.7.a, 3.15.a). Despite the discussed uncertainty, there is clear evidence from our data that the high-energy radiation sources detected during negative downward leaders propagation can be associated with different leader branches (Figure 3.7.b-c, 3.15.a). We have tried to catalog the locations of high energy sources in a possible relevant position during the propagation of the leaders (branching point, end of the unconnected leader channel, change of direction, change of speed, final jump) with respect to random leader steps, but we cannot state any clear conclusion. Although most of them, in particular the end of an unconnected leader channel ($\sim 23\%$) and the branching point ($\sim 12\%$) seem to be more frequent than a random leader step.

Even if, as already discussed, we are not able to reconstruct in 3D the direction of the leader channels, there are two observations in favor of the thesis that the high-energy radiation flux is beamed forward as observed in particular by Howard et al. (2010), Montanyà, Fabró, et al. (2014) and M. Saba et al. (2019). The first observation is related to the LB7 in Figure 3.12. It is possible to realize that the evident branching in time domain on a narrow selection ($\Delta Az_i < 5^\circ$) correspond to a branching in the direction of the INTF and probably this justifies the unusual high number of high-energy sources detected in the same location.

The second observation is related to the dart leader case. There are numerous evidence that dart leaders radiate high-energy radiation and according to Mallick et al. (2012)

in subsequent strokes the chance to detect X-ray is higher. In contrast, we detected only two low energetic X-ray pulses with an energy of about 100keV, probably due to secondary Compton scattering. This observation is consistent with M. Saba et al. (2019) measurements, which confirm the important role of the leader orientation in the X-ray detection.

At the end of section 3.2, we have already discussed the methodology to compute the 1D and 2D leader speed and the difficulties related to their measurement. The results obtained are in a very good agreement in particular with the work of Howard et al. (2010), where high-energy radiation was detected in natural CG lightning with a leader speed range of $3.6 - 9.0 \times 10^5$ m/s and with Tran and Rakov (2017), who reported a leader speed range approaching to the ground of $1.8 - 6.0 \times 10^5$ m/s.

Finally, we believe that the association between X-ray emissions and strong VHF pulses could be a key element in the study and understanding of high-energy emission phenomena. This association, in fact, reveals that both RF emissions and high-energy radiation likely share a production mechanism (Tierney et al., 2005; Howard et al., 2008; Montanyà et al., 2015).

The results presented and discussed have some relevant implications: on the origin of the intense VHF pulses, on the origin of the high-energy radiation, and in particular, on the origin of the TGFs.

3.6.1 Implications on the origin of the most intense VHF pulses

A recent study has established that VHF emissions from stepping negative leaders in lightning is most likely due to streamer formation around the region of the step (Hare et al., 2020). It is interesting to note that observations in laboratory experiments (Kochkin et al., 2014; Montanyà et al., 2015), models (Gurevich et al., 2007) and simulations (Chanrion & Neubert, 2010; Celestin & Pasko, 2011) agree that the high-energy radiation is associated with streamers development and in particular, the tip of the streamer provides the high electric field needed to initiate the electron runaway.

Therefore, the association between high-energy radiation and VHF pulses observed suggests that the origin of the VHF pulses could be due to the runaway electrons mechanism, or more in general, to the high-energy electron acceleration. It is well known that accelerated electrons produce an intense electromagnetic radiation field, whose emitted power is proportional to the square of the acceleration according to the Larmor formula. It is possible to show that the radiation spectrum in frequency domain justifies the VHF signature observed. In particular, it is relevant to note that the emitted power increases drastically in the relativistic regime.

A very high field cannot exist in air for very long, since conventional breakdown will

rapidly discharge the field. (Dwyer & Uman, 2014). The consequence of this fact is that the runaway electrons mechanism in lightning discharges is an impulsive phenomenon. In summary, high-energy radiation and the most intense VHF emissions likely share the runaway electrons as a common production mechanism. This could explain in particular, the intensity and impulsive nature observed in the VHF bandwidth.

3.6.2 Implications on the origin of the high-energy radiation

High-energy radiation undergoes a strong absorption exponentially proportional to the density of the air (e.g. Hubbell & Seltzer, 1995) which plays a crucial role in the detection, especially in ground-based observations. The strong absorption explains why the X-ray detection from lightning requires to be very close to the lightning discharge as shown by the results obtained in section 3.1. Furthermore, the small effective detector area ($\sim 0.02 \text{ m}^2$) considerably limits the chance of observation. Based on these considerations, it is reasonable to think that observed X-rays are a very small fraction compared to those actually produced by lightning leaders. This conclusion is in agreement with Monte Carlo simulations and absorption models (Østgaard et al., 2008; Celestin et al., 2015; Berge & Celestin, 2019).

In Figure 3.16, we considered the negative downward leaders event described in detail in section 3.2 and we hypothesized that all the most intense VHF pulses are associated with sources of high-energy radiation. Assuming that, the number of high-energy radiation sources is potentially greater than the one observed, many more sources ($\approx 10^2 - 10^3$) have to be taken into account.

Clearly, high-energy radiation requires energetic electrons and a threshold has to be considered to assume the correspondence with the VHF pulses, but if we assume that runaway electrons is the shared mechanism, the amplitude of the VHF pulses is related to electrons acceleration, hence it can be considered a good criterion to infer the high-energy production.

Therefore, with reference to Figure 3.16.b), if an X-ray detection is associated with a VHF pulse, there is no reason to think that another VHF pulse with comparable amplitude cannot be considered as a source of high-energy radiation too.

In our measurements, high-energy radiation has been detected in negative downward leaders with a 2D speed range of $0.4 - 1.2 \times 10^6 \text{ m/s}$ and in a dart leader with a 2D speed of $2.0 \times 10^7 \text{ m/s}$. Unfortunately, we were not able to establish a strong relation between the leader speeds required for high-energy production, although we speculate that intense VHF pulses in negative leader with comparable speed could be considered as high-energy sources.

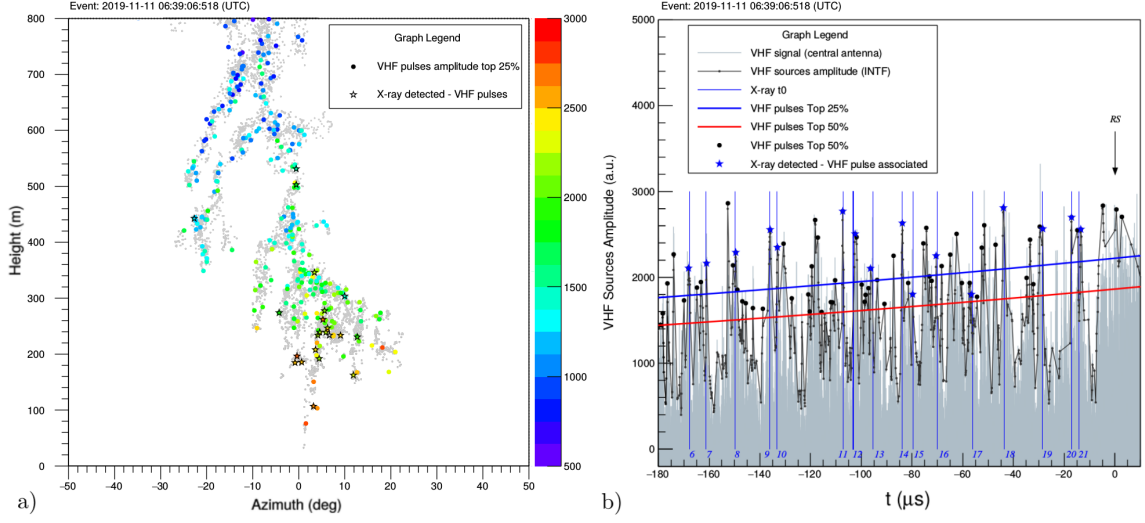


Figure 3.16: Assumption of a correspondence between the most intense VHF pulses and the high-energy radiation sources applied on real data. a) Most intense VHF sources, colored by VHF amplitude, if associated with X-ray detection marked with black stars. b) Temporal correspondence between VHF pulses and high-energy radiation sources. If the correspondence was really observed (blue stars) if only hypothesized (black dots).

3.6.3 Implications on the origin of the TGFs

Although our measurements are related to high-energy radiation in cloud-to-ground lightning, some relevant considerations could be extrapolated for TGFs detected from the space. First of all, it is evident from our analysis that the X-ray bursts detected in coincidence with negative downward leaders are originated by multiple sources of high-energy radiation. As discussed in the previous section, the number of these sources is clearly underestimated by ground measurements, essentially due to the strong absorption exponentially proportional to air density.

This suggests that the origin of TGFs could be seen as the cumulative effect of many sources, each capable of generating runaway electrons. The cumulative effect is capable of explaining the origin of TGFs observed with the duration of several microseconds (e.g. $\gtrsim 50\mu$ s). This is more consistent for events with a longer duration. On the other hand, in shorter TGFs, since there are fewer sources in the time interval, it is not possible to state this conclusion with the same confidence. This hypothesis supported by our observations is in agreement with Celestin and Pasko (2012) simulations and Dwyer and Cummer (2013) calculations. From a spatial point of view, the multiplicity of sources translates into an extensive origin of the TGF radiation.

The association between X-ray emission and strong VHF pulses can be considered a valuable method to locate the high-energy radiation phenomena. Furthermore, it can be a crucial criterion to locate the origin of the TGFs, as recently shown in Lyu et al. (2018) two TGFs were associated with $10 \mu\text{s}$ accuracy with a strong VHF emission detected by the Lightning Mapping Array (LMA). Our measurements can suggest that likely those strong VHF emissions can be properly associated with the high-energy radiation and therefore that could be the most accurate spatial and temporal reference of the TGFs origin.

Moreover, it is interesting to point out a very good agreement between the leader speed measured in CG negative downward leaders and a few measurements in the literature of leader speed in IC negative upward leaders associated with TGF production. In particular, the leader speed measured by X.-M. Shao, Hamlin, and Smith (2010) $0.4 - 0.6 \times 10^6 \text{ m/s}$ and Cummer et al. (2015) $0.8 - 1.0 \times 10^6 \text{ m/s}$. Although more investigations are needed to evaluate the relation between leader speed and high-energy radiation, leader speed could be another relevant observable in TGF studies from ground measurements.

Finally, we would like to compare our results with the downward TGFs observed by the Telescope Array reported by Abbasi et al. (2019) since their instrument allows unique ground measurements of the high-energy radiation from lightning discharges. We point out several analogies which their results (summarized in section 1.) that allow us to believe that the observed phenomena are substantially the same.

3.7 Conclusions

In this work, we presented the first simultaneous X-ray measurements from natural lightning in coincidence with a VHF broadband interferometer. We can summarize the results we obtained with the following observational evidence:

1. Multiple high-energy radiation sources were observed and located during the propagation of negative downward leaders, in different leader branches.
2. A strong temporal correspondence has been observed between the high-energy radiation and the most intense VHF pulses, comparable with our instrumental uncertainty $\sim 0.5\mu\text{s}$.
3. High-energy radiation has been detected in negative downward leaders with a 2D speed range of $0.4 - 1.2 \times 10^6 \text{ m/s}$ and in a dart leader with a 2D speed of $2.0 \times 10^7 \text{ m/s}$.

From these observations, we have identified some relevant implications and consequences:

1. High-energy radiation and strong VHF pulses likely share the runaway electrons as a common production mechanism. The impulsive nature of the VHF pulses and their power are explained by the radiation field and the Larmor formula in the VHF bandwidth.
2. The strong absorption, exponentially proportional to the density of the air, plays a crucial role in high-energy detection, especially in ground-based observations. X-ray bursts detected in coincidence with negative downward leaders are originated by multiple sources of high-energy radiation that can be located in the proximity of the leader step region, many more sources ($\approx 10^2 - 10^3$) can be inferred observing the most intense VHF pulses.
3. Assuming that TGFs are produced during the upward leaders propagation, not a unique origin has to be searched but an extensive origin due to the multiplicity of sources. Dwyer and Cummer (2013) address and put limits on this multiplicity in TGFs. This cumulative effect is able to explain the origin of TGFs observed with a duration of several microseconds.
4. Our measurements suggest that strong VHF emissions, like those observed by Lyu et al. (2018) with LMA, can be properly associated with the high-energy radiation and therefore that could be the most accurate spatial and temporal reference of the TGFs origin.
5. The results are consistent with the observations of Abbasi et al. (2019). We believe that our conclusions can find further confirmation in their future studies allowing a better understanding of the mechanisms of TGF production.

4. Urbani et al.(2022): Multi-stroke positive cloud-to-ground lightning sharing the same channel observed with a VHF Broadband Interferometer

M. Urbani, J. Montanyá, O. A. van der Velde, M. Arcanjo, J. A. López, *Multi-Stroke Positive Cloud-To-Ground Lightning Sharing the Same Channel Observed With a VHF Broadband Interferometer*, Geophysical Research Letters, 10.1029/2021GL097272, 49, 9, (2022)

4.1 Abstract

This work presents the first observation of a multi-stroke positive cloud-to-ground lightning flash sharing the same channel to ground mapped with a VHF broadband interferometer and a Lightning Mapping Array. This type of lightning flash is very rarely observed, and it is currently unclear how frequent it is and even under what conditions it occurs. Our observations indicate a scenario where the first downward positive leader initiates from a decayed negative channel. After the first return stroke, some of the main negative channel branches stop propagating and likely cut off. A fast recoil leader and/or a fast breakdown play a crucial role in reconnecting these previously decayed leader channels and initiating the subsequent positive stroke. The mechanism we propose to describe the phenomenon allows us to explain its rarity and the discrete positive charge transfer to the ground.

4.2 Plain Language Summary

In the same lightning flash, whose usual duration is less than a second, there can be multiple negative cloud-to-ground (-CG) strokes with different terminations or following a pre-existing channel to the ground. In contrast, it is not common to have multiple positive cloud-to-ground (+CG) strokes, and especially multi-stroke +CG flashes sharing the same channel to ground are very rarely observed. This polarity asymmetry is not well understood and many aspects are debated. In this letter, we present for the first time a very high frequency (VHF) radio band observation of a multi-stroke +CG flash along the same channel, observed simultaneously by a VHF broadband interferometer (INTF) and a Lightning Mapping Array (LMA) in north-central Colombia. These combined observations have unprecedented temporal and spatial resolution and allowed us to observe in detail the development of the flash and especially to understand the initiation mechanism of the subsequent positive stroke.

4.3 Introduction

Positive cloud-to-ground (+CG) lightning flashes are less frequent than the negative counterpart, about 10% of the global cloud-to-ground lightning, but in general, their charge transfer is an order of magnitude greater (Rakov & Uman, 2003). For this reason, they usually can cause more damage, especially to tall structures like wind turbines (e.g., Montanyà, Van Der Velde, & Williams, 2014; Becerra et al., 2018) or cause wildfire ignition (e.g., Fuquay et al., 1972; Blouin et al., 2016). Furthermore, +CG flashes are mainly associated with the production of transient luminous events like sprites (e.g., Boccippio et al., 1995; Williams et al., 2010). Therefore, +CG flashes have attracted significant research interest in recent years and some aspects are still debated or require a better understanding.

One of these aspects concerns the origin and the development of multi-stroke +CG lightning. Positive flashes usually have a single stroke (Rakov & Uman, 2003). However, several cases of multi-stroke positive flashes were recently observed and reported in the literature. The first study reporting optical observations of multi-stroke +CG flashes was conducted by Fleenor, Biagi, Cummins, Krider, and Shao (2009). They documented for the first time subsequent positive strokes sharing the same channel to ground, and observed nine multi-stroke +CG flashes of which five cases involving a pre-existing channel. M. M. Saba et al. (2010) reported high-speed video observations of 19 multi-stroke +CG flashes and only one case of subsequent positive stroke along the same channel. These optical observations highlighted the occurrence and rarity of

the phenomenon, but present limitations in describing the flash development within the cloud and the mechanisms that make subsequent positive strokes possible.

Thanks to improved lightning detection systems, new observations and findings on multi-stroke +CG flashes are emerging. Wu, Wang, and Takagi (2020) reported 47 new observations during the winter season in Japan. They observe that downward positive leaders (DPLs) in multi-stroke flashes are mostly originated from in-cloud negative leader channels. They did not observe any subsequent stroke along the same channel. Yuan et al. (2020) investigated the origin of an uncommon three-stroke event with different terminations to ground and proposed a mechanism involving an advancing negative leader.

Recently, Zhu et al. (2021) observed 84 multi-stroke +CG flashes during a supercell storm in Argentina. They observed 54 (64%) +CG flashes with a subsequent leader likely following a pre-existing channel to ground (within 100 m between the striking points) and they suggested that the behavior of subsequent leaders in positive lightning can be very similar to subsequent leaders in negative lightning. These new observations raise interest and new questions about the conditions necessary for these phenomena to occur and what mechanisms may explain the discrete charge transfer along the same channel in +CG flashes.

4.4 Instrumentation and Methodology

The data presented in this work were recorded during an observational campaign at the Universidad Industrial de Santander (UIS) campus of Barrancabermeja (Colombia) in autumn 2019. Instruments, processing techniques, and the deployment of the instrumentation are further described in Urbani et al. (2021) and in the Supporting Information (SI).

4.4.1 VHF Broadband Interferometer

A VHF broadband interferometer (INTF) is an instrument capable of mapping lightning discharges with a high temporal resolution. We designed and built our version, which consists of three VHF antennas (20-80 MHz bandwidth) deployed along two orthogonal baselines of 22 m. The digitizer used for the acquisition system is a GaGe Razor Express 1604 with four channels, 16-bit resolution, and 200 MS per second sampling rate. The interferometric processing technique is a window-based cross-correlation method (Stock et al., 2014) improved by a clustering algorithm to average overlapping solutions and perform noise reduction (Urbani et al., 2021). The time window length used is 512 samples (2.56 ns), timing uncertainty, and angular resolution are reported in the Supporting Information S1.

4.4.2 Colombia Lightning Mapping Array

The Colombia LMA was installed by the Universitat Politècnica de Catalunya (UPC) lightning research group (López et al., 2019). It consisted of 8 VHF antennas (60-66 MHz bandwidth) deployed with baselines from ~ 6 to ~ 36 km around the city of Barrancabermeja. The processing technique based on time-of-arrival is provided by New Mexico Tech (Rison et al., 1999; Thomas et al., 2004).

4.4.3 Quasi-3D conversion

Simultaneous detections of a lightning flash with the INTF and the LMA allow us to use a post-processing technique, which has the great advantage of combining the high temporal resolution of the INTF with the spatial accuracy of the LMA. This interpolation technique called “Quasi-3D conversion” was introduced and described by Stock (2014). This technique is approximated and imperfect because, in some cases, there simply are not enough LMA sources to reconstruct the correct development of all leader branches (or fast lightning processes) and sometimes, it may introduce artifacts. Noise reduction and supervised processing are needed to get reliable results. Despite that, Quasi-3D reconstruction adds substantial information to understand the overall structure of the flash, removing the typical ambiguity in the 2D data of the interferometer (Figures 1e and 1f).

4.5 Observations and Analysis

We observed two multi-stroke +CG flashes with a double stroke along the same channel to ground, named with the timestamp in UTC of the first return stroke (RS1): (a) 2019-10-27 11:05:10 and (b) 2019-10-27 11:15:06. We present in detail only the second flash for the sake of brevity, but where some differences are relevant, or some important results are consistent, we mention the other case.

4.5.1 Multi-stroke +CG flash: 2019-10-27 11:15:06

In this section, we describe the development of the multi-stroke +CG flash (b), which can be best appreciated from the Quasi-3D data animation provided in the Supporting Information S1. A frame of this animation and the evolution of the main physical quantities and dimensions are shown in Figure ???. Additionally, a schematic representation of the flash development is provided in Figure 4.2.

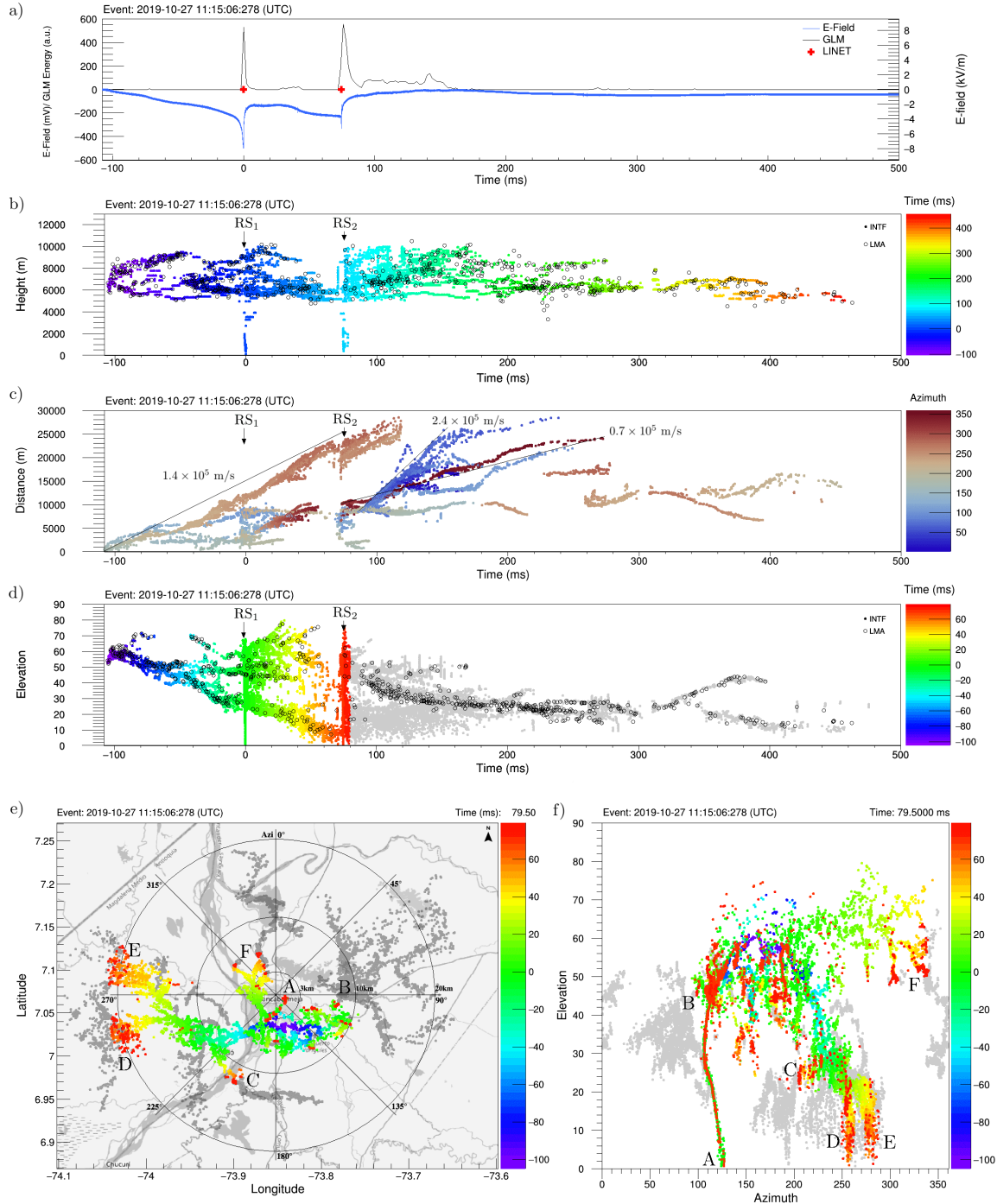


Figure 4.1: Multi-stroke +CG flash along the same channel, event: 2019-10-27 11:15:06 (UTC). a) Electric field waveform recorded by a flat plate antenna, LINET detections (Betz et al. 2009) and Geostationary Lightning Mapper (GLM) energy (Goodman et al. 2013). b) Flash evolution in altitude, Quasi-3D data. c) Time-distance plot from the flash initiation, Quasi-3D data. d) Time-elevation plot, INTF data compared with LMA data. e) Spatial development of the flash, Quasi-3D data. f) Elevation-azimuth plot, INTF data. It is possible to observe (see letter A) the subsequent positive stroke (red) along the same pre-existing cloud-to-ground channel (green). The correspondence between panels e) and f) is highlighted through the letters A-F. An animation of the entire flash is available in the Supporting Information S1.

The origin of the flash (b) was located by the LMA at an altitude of around 6 km and a horizontal distance from the INTF of about 4.5 km.

After an initiation phase, of which the duration is around 1.5 ms propagating upward, several negative leader branches start growing with an average speed of 1.2×10^5 m/s in two main directions, upward and horizontal (Animation S1, Figure 2a). The strong VHF emission of the negative leaders masks the positive leader development, and only a faint emission belonging to the positive leaders can be clearly located at a height of around 5.5 km after 31 ms from the initiation. The upward negative leader subsequently forks again and both branches stop propagating about ~ 40 ms before the first positive stroke, reaching an altitude of around 10 km. The main horizontal negative leader branch grows westward, generating multiple secondary branches.

According to our best interpretation of the data (Figure S3, Figure 2c), it seems that the DPL does not originate from the typical bidirectional leader development after the flash initiation (e.g., Mazur, 2002; van der Velde et al., 2014; Li et al., 2020), but from the negative horizontal channel in its lowest altitude location (~ 5.7 km). A similar scenario is widely reported in the literature (e.g., Krehbiel, 1981; M. M. Saba et al., 2009; Nag & Rakov, 2012; Wu et al., 2020). In our data, it is possible to observe a recoil leader along a decayed secondary branch of the horizontal negative channel simultaneously with the DPL initiation, 4.8 ms before RS1. This could be evidence of a disconnected channel and it might create the conditions to initiate the first DPL (Figure 2b, Figure S3). Further details on the initiation and propagation of the first DPL are discussed in section 3.3 and reported in the Supporting Information S1.

RS1 brings ground potential to the channel, inserting negative charge along the in-cloud leader channels. The majority of the negative leader channels are involved, but there is more VHF activity in the horizontal channel compared with the vertical ones. After RS1, another main leader branch initiates and propagates northward with a similar speed (negative branch F, Figure 1e, Figure 2d). All the leader branches to the east stop propagating after 40 ms from RS1 (Figure 2e) and 18 ms later, even the northward branch (F) stops propagating, while the main horizontal branch continues to propagate, reaching a length of about 25 km (Figure 2f). Approximately 2 ms before the second return stroke (RS2), a fast recoil discharge can be observed, which appears to involve or possibly trigger the subsequent DPL (Figure 2g). More details on this fast process and the initiation of the second DPL are discussed in section 3.2. The interstroke interval between the RS1 and RS2 is about 74.5 ms, whereas in flash (a) it is about 25.5 ms.

Similarly, after the RS2, it is possible to observe a burst of VHF activity that can be associated with the continuing current phase (e.g., Lapierre et al., 2017). The continuing current can also be seen from the Geostationary Lightning Mapper (GLM) data and the electric field measurements (Figure 1a). Figure 1e shows the increase

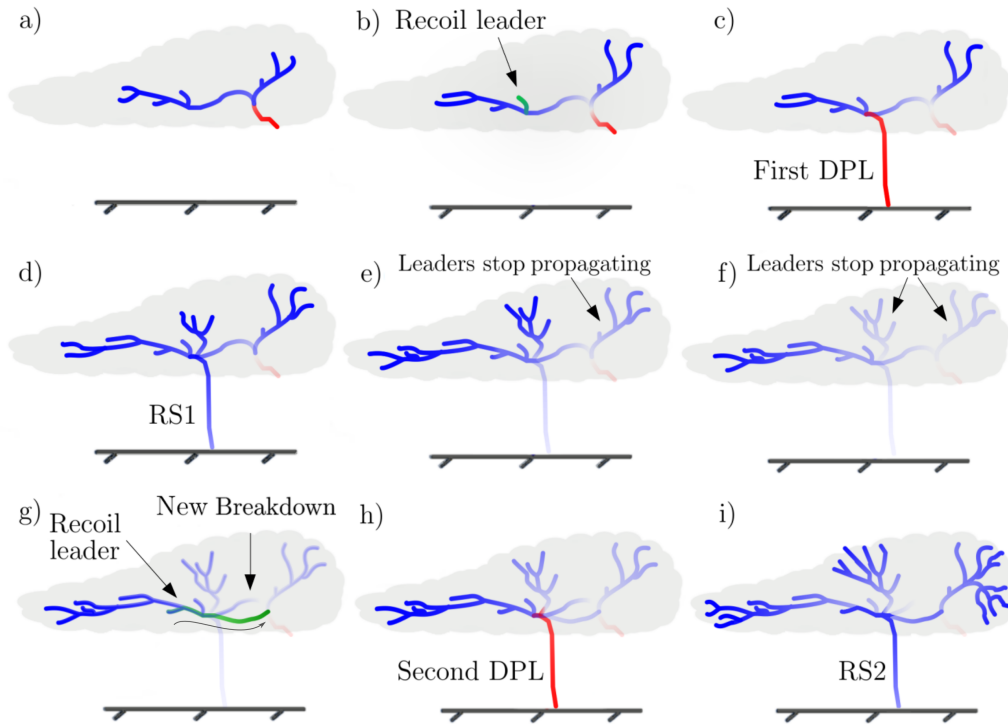


Figure 4.2: Schematic illustration of the multi-stroke +CG flash 2019-10-27 11:15:06. Blue and red lines indicate respectively propagating negative leaders and propagating positive leaders (observed by the INTF). Green lines indicate fast lightning processes such as recoil leaders or fast new breakdowns. The gradient color indicates time evolution, and the faded color indicates decayed channels which are no longer propagating.

in VHF activity, especially in the westward horizontal branches (C,D,E) and in the previously stopped northward branch (F), where the fast processes (red color) correspond to the re-ionization of the leader tips, an effect of the continuing current. The negative leader branch (F) restarts to propagate again after RS2 (Figure 2i). A new leader branch (B) is initiated after 15 ms from RS2, giving rise to a particularly extended and branched negative leader with higher speed 2.4×10^5 m/s, probably developing in a previously highly ionized area.

4.5.2 Initiation of the subsequent positive leader along the previous channel

One of the main questions regarding multi-stroke +CG flashes is how the subsequent DPL could initiate and propagate along the same channel of the first DPL, and why this is not as common as in -CG flashes. To investigate this aspect, we analyze what happens in the last milliseconds before the second return stroke. In this section, we describe the observations and the analysis for flash (b); the other case is reported in the Supporting Information S1.

Figure 3a is an overview of the data collected in the last 4 ms before RS2. It can be seen that a fast recoil leader [A] starts to propagate at about 2.4 ms before RS2. After 0.5 ms, it initiates a new breakdown phase [B] and then it continues to propagate, likely retracing a previous channel [C] until about 1.5 ms before RS2. We observed that the recoil leader initiates from the far end of a secondary decayed branch belonging to the main horizontal negative leader branch. This secondary branch is the one likely involved in triggering the first DPL (Figure S3) and subsequently extended by RS1 (Animation S1). The recoil leader retraces the channel propagating backward (Figure 3b). Although we are not able to precisely localize the three-dimensional development of this branch, the fact that it proceeds from a lower to a higher elevation suggests that the recoil leader is approaching, in the INTF reference system. This assumption is also supported by the increase of the VHF intensity and the monotonic enhancement of the electric field detected by the flat plate antenna in time correspondence with the recoil leader stage [A], as indicated by a black arrow (EF1) in Figure 3a. The combined observations of the leader's spatial development and the electric field enhancement allow us to infer the leader polarity, which is consistent with an approaching negative leader. The recoil leader speed was estimated to be between $1.0 - 1.5 \times 10^7$ m/s by comparison with the speed of the previous negative leader (1.2×10^6 m/s) along the same channel.

After 0.5 ms, we observed a strong increase of the VHF intensity and a variation in the electric field consistent with a fast negative breakdown [B], which likely reconnects previously disconnected leader channels. According to what we can see with the

INTF, it is interesting to note that it does not seem to retrace a previous channel, but it traces a new path connecting itself with the origin of the flash (Figures 3b and 3c). After the connection with the origin of the flash, another recoil leader [C] can be observed, likely the continuation of [A] and [B], in a decayed leader branch clearly not belonging to the main horizontal leader channel. When the recoil leader [C] stops propagating, it can be observed in the electric field waveform the indication (EF2) of an accumulation of positive charge, which gives rise to the second DPL in the following 0.3 ms.

Finally, we show in Figure 3e the first 300 microseconds after the second DPL connection to the ground. It is interesting to note that the whole in-cloud VHF activity during this time interval is located around the recoil leader A-C. Especially, as indicated by the arrows, along the recoil channel [A], then in [C] and in the junction point between [A] and [B] from where it originates a new fast negative leader. These observations seem to support the hypothesis that the recoil leader A-C is not an uncorrelated lightning process happening before RS2 but probably the trigger mechanism of the subsequent DPL.

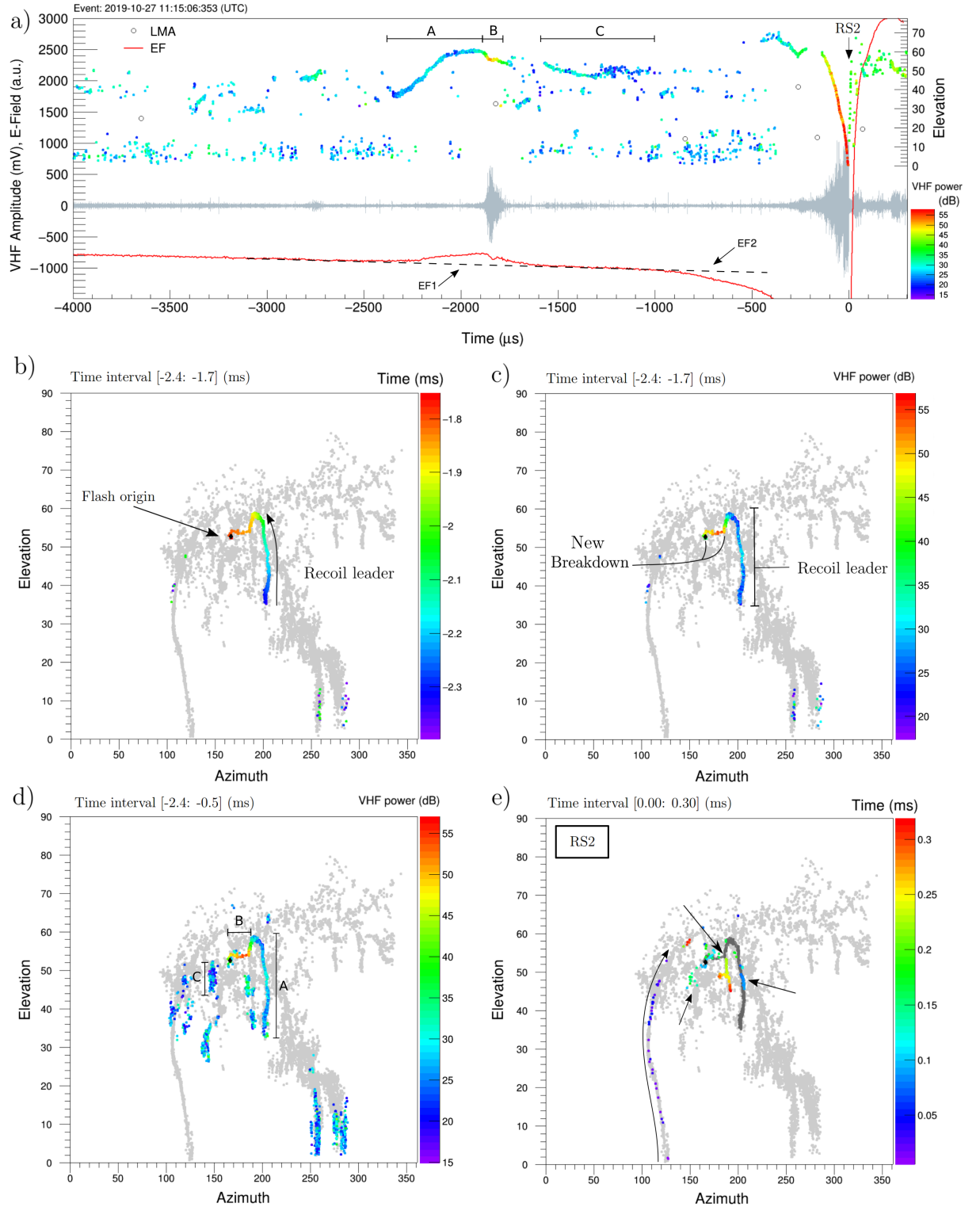


Figure 4.3: Initiation of the second DPL along a previous channel to ground, multi-stroke +CG flash 2019-10-27 11:15:06 (UTC). a) Overview of the last 4 ms before RS2. Time-elevation plot of the VHF sources mapped by the INTF and LMA. Electric field waveform (red line) recorded by the flat plate antenna and VHF waveform (gray line). Black arrows indicate the electric field variations in correspondence, respectively, with the approaching recoil leader (EF1), and the DPL (EF2). b) and c) Recoil leader and new breakdown connecting a previous channel end to the flash origin. Respectively colored by time and VHF power. d) Elevation-azimuth plot of the leader channels A-C. e) VHF sources in the subsequent 300 microseconds after the DPL connection to the ground. It is relevant to note VHF activity near the previous leader channels A-C.

4.5.3 Comparison between the first positive stroke and the subsequent stroke.

The striking point of +CG flash (b) is about 1.2 km away from our INTF location. The accuracy of this location is good because LINET detected both positive strokes and provides compatible values (same longitude: -73.8412 and latitude: 7.0674 and 7.0670). Furthermore, the INTF mapping confirms they have the same channel and same striking point. According to LINET, the peak current of RS1 is 52.2 kA and the subsequent 20.7 kA and the time elapsed between them is about 75 ms.

In Figure 4, we provide an unprecedented high-resolution comparison between the first positive stroke and the subsequent stroke. It is particularly interesting to note the different VHF signatures of the two DPLs. The first DPL is propagating in virgin air with a quite constant 2D speed of 1.5×10^6 m/s in the last 750 μ s before RS1. The VHF waveform presents an intermittent pattern of bursts of VHF pulses with an evident periodicity, every 10-20 μ s, located on the positive leader tip (Figure 4a). A similar observation of this intermittent pattern was recently shown by Pu et al. (2021). Further analysis of the VHF bursts and the DPL propagation is reported in the Supporting Information S1.

The subsequent DPL is faster, following a pre-ionized channel, its average 2D speed is quite constant at 1.3×10^7 m/s and slightly accelerating in the last 20 μ s to 2.0×10^7 m/s. This speed range is very similar to the speed of dart leaders following negative CG strokes (e.g., Urbani et al., 2021) and the recent measurements of Zhu et al. (2021). In the subsequent DPL, it is not possible to clearly distinguish any intermittent pattern. This could be due to the higher speed or different propagation conditions along the pre-existing channel.

Another remarkable observation is regarding the VHF waveform of the return strokes (Figures 4a and 4c). RS1 has a more intense VHF signal and a 2D speed of 5.1×10^7 m/s while in RS2 the signal amplitude is much weaker and the 2D speed is higher, about 1.23×10^8 m/s. It is interesting to note that despite the higher speed and the weaker signal, the INTF was able to better map RS2 than RS1, which suggests that in RS1 more sources were simultaneously emitting (along the channel or in different branches) while in RS2 what has been mapped is the wavefront of the return stroke (Figure 3e). We suggest that the different VHF signatures between the first and the subsequent return stroke could be due to the different conductivity of the channel, higher in RS2 than RS1.

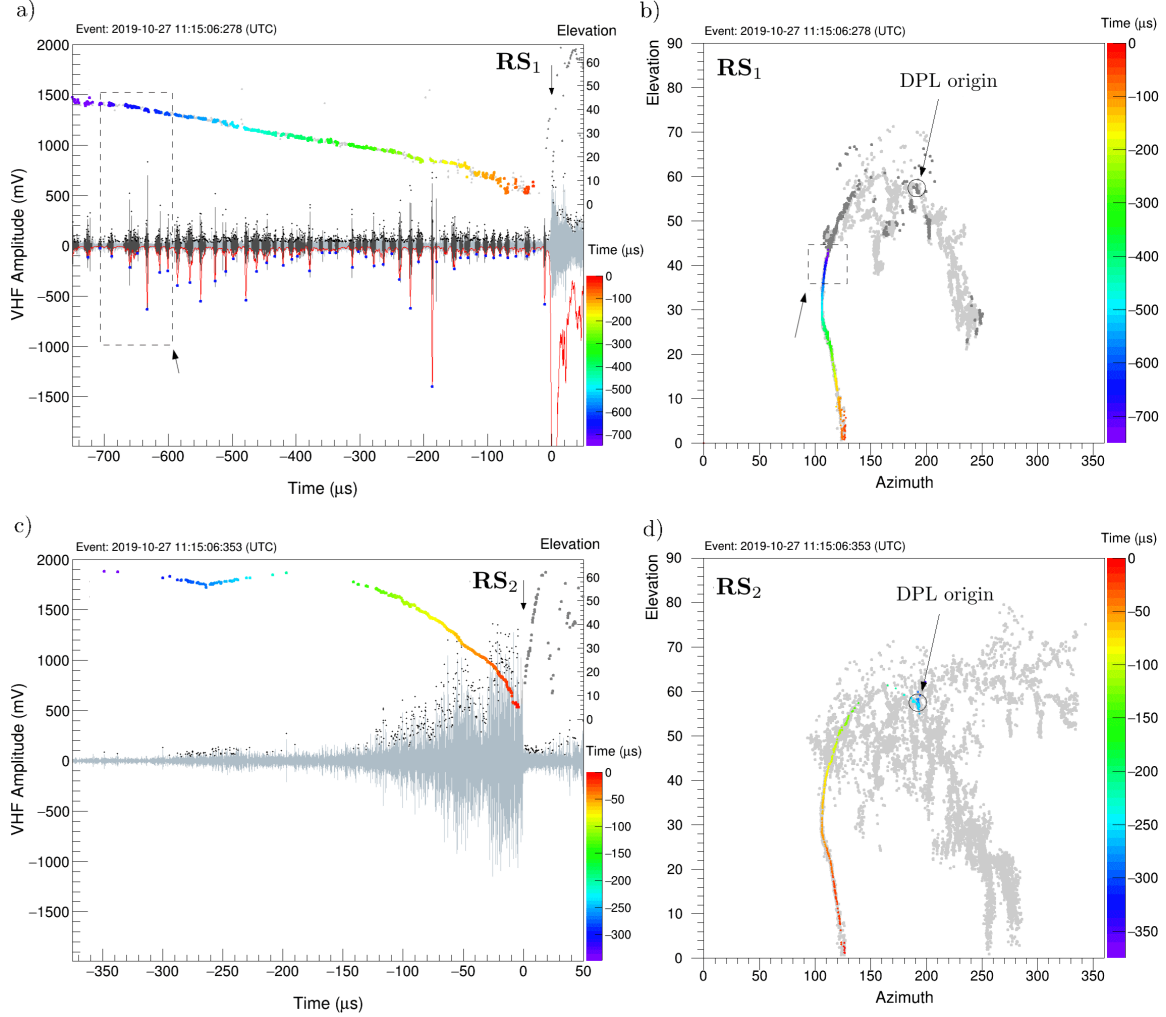


Figure 4.4: Comparison between the first and the second positive strokes of the multi-stroke event: 2019-10-27 11:15:06 (UTC). a) VHF waveform and sources mapped by the VHF broadband interferometer (INTF) of the first positive stroke. The intermittent pattern of VHF waveform is highlighted through two different shades of gray, an envelope (red line) and its magnitude local maxima (blue dots). b) Elevation-azimuth plot of the VHF sources mapped by the INTF, c) VHF waveform and sources of the second positive stroke. d) Elevation-azimuth plot.

4.6 Discussion

The recent observations by Zhu et al. (2021) by means of the low/high frequency with the Córdoba Argentina Marx Meter Array (CAMMA) suggest that the processes in positive flashes with multiple strokes to ground sharing the same channel appear very similar to the mechanism in -CG flashes but with opposite polarity. Their observations belong to a supercell storm anomalously charged with the main negative charge region located above the main positive charge region. They observed that the positive subsequent strokes were initiated from the decayed in-cloud negative branches near their far ends by recoil leaders. In the three-stroke +CG flash presented by Zhu et al. (2021), they were able to map the positive recoil leader propagating backward, with a duration of more than 10 ms.

Similarly to Zhu et al. (2021), we observed that subsequent strokes occur after some negative leader branches stop propagating. Therefore, the presence of decayed negative channels seems to be a key aspect in multiple positive strokes. We also observed a recoil leader initiated from the far end of a decayed leader channel, but in our case, it is a much faster process (speed 10^7 m/s and duration of 1.8 ms) and according to our analysis, the recoil leader polarity seems to be negative. In both flashes we recorded, we observed a fast negative breakdown a few hundred microseconds before the second DPL initiation, respectively, 200 microseconds for flash (a) and 1.8 milliseconds for (b). The observation of this fast breakdown along a new channel path, described in section 3.2, has never been reported before. Our interferometer and LMA data do not show a slow positive recoil leader of several milliseconds before the subsequent return stroke as observed by Zhu et al. (2021), but this is not necessarily in contradiction with their observations. Our instrumentation operates at a higher frequency radio band, and it is more suited to detect breakdown and streamer activity near the head of propagating leaders instead of in-cloud current pulses. Therefore, we do not exclude that a slow positive recoil process like the one described by Zhu et al. (2021) could occur along with one of the cutoff negative leaders during stage (f) in Figure 2, while their instrument does not resolve the very fast process we observed during stage (g).

We propose an alternative interpretation of our data, which does not require a slow positive recoil leader, but still involves the presence of decayed channels that cut off after the first return stroke (Figures 2e and 2f). The evidence of this disconnection is found in the fast breakdown observed in the two milliseconds before the DPL (Figure 3). We assume an accumulation of positive charge at the root of one of the previous negative leaders, during stage (f), to explain the negative recoil leader we observed in the opposite direction of a propagating negative leader branch. The fast breakdown acts as a switch that reconnects the decayed leader channel branches and allows the

positive charge to propagate downward in the pre-existing return stroke channel to ground (Figures 2g and 2h). In this scenario, the positive leader occurs after the trigger mechanism and is much faster in time (two orders of magnitude) than what was observed by Zhu et al. (2021). Actually, our observations have similarities to the two-stroke +CG flash shown by Zhu et al. (2021) in their figure 4, where a slow positive recoil leader is not evident and it might be an indication of a fast breakdown before RS2, as it can be seen in the electric field waveform.

This mechanism might explain why the multi-stroke +CG flashes along the same channel are rare. The reason could be that usually in single stroke +CG flashes the DPL originates from the bi-directional flash initiation (e.g., van der Velde et al., 2014), whereas in multi-stroke +CG flashes, the DPLs mostly originate from in-cloud negative leader channels (Wu et al., 2020; Yuan et al., 2020). Furthermore, the condition of sharing the same channel to ground instead of initiating a new DPL may be subordinated to the possibility of a re-connection with a decayed channel through a fast recoil leader and/or a breakdown.

The available cases suggest that this type of +CG flash requires more than one main negative leader branch near the flash origin and first stroke location. In addition, the cutoff must occur within tens of milliseconds after the first return stroke in order to maintain the conductivity of the channel to ground for it to be re-used. These conditions may not be facilitated in all storms.

Due to the scarcity of similar observations, the data presented are particularly valuable in describing the multi-stroke +CG flashes along the same channel. Likely not one single mechanism is able to explain each occurrence. Further studies and observations will lead to a more complete understanding of this phenomenon.

Open Research

Measurements and data file supporting the conclusions are available at:
<https://doi.org/10.7910/DVN/YUWYRD>

5. Conclusions and future perspective

This thesis presents as a compendium of articles the investigation carried out with the VHF broadband interferometer that I built for my Ph.D project.

This PhD project originated from a larger European project within the SAINT (Science and INnovation with Thunderstorms) collaboration. The network of scientists, involved in SAINT, is leading the European space missions of ASIM (Atmosphere-Space Interactions Monitor) an instrument dedicated to study two lightning correlated phenomena: the Terrestrial Gamma-ray Flashes (TGFs) and the Transient Luminous Events (TLEs).

My project titled "High-energy radiation from lightning strikes" was focused in studying the high-energy emissions in cloud-to ground lightning, collecting new data simultaneously with a VHF Broadband Interferometer and ground-based detectors. The main goal of the project was to determine the lightning process that generates high-energy radiation and study the sub-process related.

The objectives and the deliverables required by the SAINT Marie Curie project were successfully achieved, essentially, with the first paper. The second paper is a further evidence of the usefulness and effectiveness of this instrument in lightning research.

The first paper shows clearly that the X-ray bursts can be observed in negative downward leaders and dart leaders. Almost every negative lightning strike in a 1.0 km range produced detectable X-rays emissions. The observations revealed a strong temporal correlation with the most intense VHF pulses. This correlation suggest a shared physical process between the VHF emissions and the high-energy radiation, we think the runaway electrons could radiate for the relativistic Larmor formula the VHF emissions we revealed. This correlation allows to locate the high-energy emission during the negative downward leaders propagation and allowed us to observe that different leaders branches even at hundreds meters apart can contribute to the same X-ray burst. These conclusions can have several implications in the study of the TGFs

detected from ground and space. Our conclusions is that probably the high-energy radiation is more common than expected and probably the emissions are much more beamed in the direction of the leader propagation than what is expected.

Further research is needed to prove these hypotheses, and a full 3-D interferometer would be needed to obtain downward leader directions and correlate them with the high-energy emission flux. Another improvement would be to install several high-energy stations to cover a larger area and provide much more detail on the high-energy bursts. Finally, better detectors, with faster resolution in terms of rise time and energy, would be needed to understand the flux and the energy spectrum of these emissions.

The second paper presented the first observation of a multi-stroke positive cloud-to-ground flash along the same channel to ground observed with a VHF broadband interferometer and a Lightning Mapping Array. These simultaneous observations allowed us to apply an advanced post-processing technique called "Quasi-3D conversion" to reconstruct the entire flash combining the high temporal resolution of the INTF with the three-dimensional spatial accuracy of the LMA. Thanks to this technique we were able to map in great detail the development of the multi-stroke +CG flash and especially the positive leader channel to ground and to propose a mechanism for this rare phenomenon.

We reconstructed the cloud charge structure in proximity of the events using the LMA data. Our results show that multi-stroke +CG flashes can occur in the dissipation phase of a storm likely in the presence of an active, vertical, and compact cell. In particular for the flash observed, we were able to identified the DPL origin from the lower altitude location of an horizontal negative leader channel in the quasi-neutral charge region. We made an unprecedented detailed comparison between the first +CG stroke and the subsequent stroke along the same channel in VHF band and we analyze in deep the first DPL. Finally, we observed in both cases a fast recoil leader and/or a fast breakdown connecting decayed leader channels play a crucial role in triggering the subsequent positive stroke. These observations have a relevant implications in understanding the charge asymmetry in lightning leaders.

Summing up, the main achievement of this Ph.D. work is the development of a VHF Broadband Interferometer, an instrument that allows us to carried out high quality scientific research on lightning physics.

The main scientific results of the two papers can be summarized in the following key-points:

1. X-ray bursts were detected simultaneously with a lightning imaging obtained from a VHF broadband interferometer.
2. A strong temporal correspondence has been observed between the high-energy radiation and the most intense VHF pulses.
3. The runaway electrons mechanism could be the shared mechanism between the high-energy radiation and the VHF emissions. Runaway electrons can produce VHF emissions according to the Larmor formula and high-energy emissions for Bremsstrahlung.
4. Measurements suggest an extensive spatial origin of TGFs due to a multiplicity of high-energy sources.
5. First time observation of positive cloud-to-ground strokes sharing the same channel to ground with a VHF broadband interferometer.
6. A fast recoil leader and/or a fast breakdown connecting decayed leader channels play a crucial role in triggering the subsequent positive stroke.
7. The high-resolution comparison between the first and subsequent stroke shows different VHF signatures related to the channel conductivity.
8. A new mechanism for multi-stroke positive cloud-to-ground strokes sharing the same channel to ground was proposed.
9. The downward positive leader propagation shows an intermittent pattern of VHF bursts whose frequency increases as it approaches ground.

5.1 Future perspectives

Recently, our VHF Broadband Interferometer was used for other two observational campaigns in Colombia (2021) and in Italy (2022).

In Colombia, the INTF was installed in the same site of the previous measurements in the city of Barrancabermeja and simultaneously observations with two photometers (337 and 777.4 nm) and an high-speed camera were carried out by another member of our LRG, José Andrés Roncancio. The results of this campaign of observation will be published soon.

In Italy, the INTF was installed at Passo del Lupo (MO) near Mt. Cimone for a site survey. We got the opportunity to extend the installation period for one month and several lightning flashes were collected. The hope is to have obtained simultaneous measurements with the Gamma-Flash detector installed on the top of Mt. Cimone (Tiberia et al., 2022; URSI et al., 2022). The data analysis is in progress.

In addition, during our campaign in Colombia in 2019, we installed two interferometers with the hope of obtaining full 3-D mapping of lightning development. Unfortunately, due to logistical limitations, it was not possible to install the two interferometers in two different locations 2-4 km apart as our simulations suggested. Instead, we were able to install the two interferometers INTF1 and INTF2 on the same rooftop only 50 m apart (Figure 3.1). By having two different interferometers, we obtained a larger number of recorded events and some of them simultaneously measured by both interferometers. Unfortunately, the too small angular separation of the interferometers did not allow 3D reconstruction. This is undoubtedly the next step, as we already have two interferometers and all the necessary algorithms to process the data in 3D.

Appendices

A. Urbani et al (2021): Supporting Information

Supporting Information

1. Table of Event: 2019-11-11 06:39:06
2. Description of the algorithm to compute t_0
3. Imaging efficiency
4. Temporal correspondence between high-energy emission and VHF pulses
5. X-ray and gamma-ray spectrum

Additional Supporting Information (Files uploaded separately)

1. Animation 1 (<https://doi.org/10.7910/DVN/VBOJBV>)
2. Animation 2 (<https://doi.org/10.7910/DVN/VBOJBV>)

Introduction

This supporting information provides additional details requested by reviewers and complementary material useful for other scientists working in the field.

A.1 Table of Event: 2019-11-11 06:39:06

Table A.1: Measurements and location of VHF pulses associated with the X-ray sources.

| X-ray | t_0 (μs) | Elevation (deg) | Azimuth (deg) | Δt (μs) | Energy (keV) |
|-------|-------------------|-----------------|---------------|------------------------|--------------|
| 0 | -735,3 | 49,7 | -0,6 | 0,3 | 641 |
| 1 | -703,4 | 48,2 | -0,5 | 0,6 | 155 |
| 2 | -599,6 | 44,5 | -22,7 | -0,1 | 99 |
| 3 | -451,7 | 37,6 | 3,4 | -0,2 | 377 |
| 4 | -273,8 | 34,0 | 10,0 | -0,3 | 266 |
| 5 | -200,8 | 31,3 | -4,3 | 0,2 | 215 |
| 6 | -168,3 | 27,1 | 12,7 | -0,3 | 506 |
| 7 | -161,3 | 31,7 | 5,6 | 0,2 | 220 |
| 8 | -149,8 | 28,0 | 5,9 | 0,2 | 1664 |
| 9 | -136,2 | 27,4 | 9,1 | 0,3 | 571 |
| 10 | -133,3 | 28,0 | 4,6 | 0,2 | 696 |
| 11 | -107,7 | 30,2 | 5,2 | -0,1 | 187 |
| 12 | -102,7 | 24,8 | 3,6 | 0,9 | 192 |
| 13 | -96,6 | 27,4 | 4,2 | -0,8 | 4210 |
| 14 | -84,2 | 22,4 | 0,6 | 0,1 | 91 |
| 15 | -80,3 | 28,7 | 6,2 | -0,2 | 94 |
| 16 | -70,8 | 23,1 | 4,4 | -0,5 | 214 |
| 17 | -57,0 | 27,4 | 6,7 | -0,4 | 4099 |
| 18 | -44,4 | 23,6 | -0,4 | -0,4 | 186 |
| 19 | -28,8 | 19,8 | 11,9 | -0,5 | 7998 |
| 20 | -17,5 | 13,3 | 3,2 | 0,1 | 456 |
| 21 | -15,2 | 22,3 | -0,8 | -0,5 | 3345 |

A.2 Description of the algorithm to compute t_0

In this section we describe the algorithm used to compute the time-of-arrival t_0 of the X-ray emissions detected by the NaI(Tl) high-energy detector described in section 2.2.

Due to rising time, the noise level and in particular the large decay constant of the high-energy detector, it is not trivial to evaluate t_0 uniquely and with good accuracy ($< 0.5\mu s$).

Therefore we compute t_0 as the time reference of the cross-point between the linear interpolation of the pulse rising and the linear interpolation of the noise level before the pulse rising (see Figure 1).

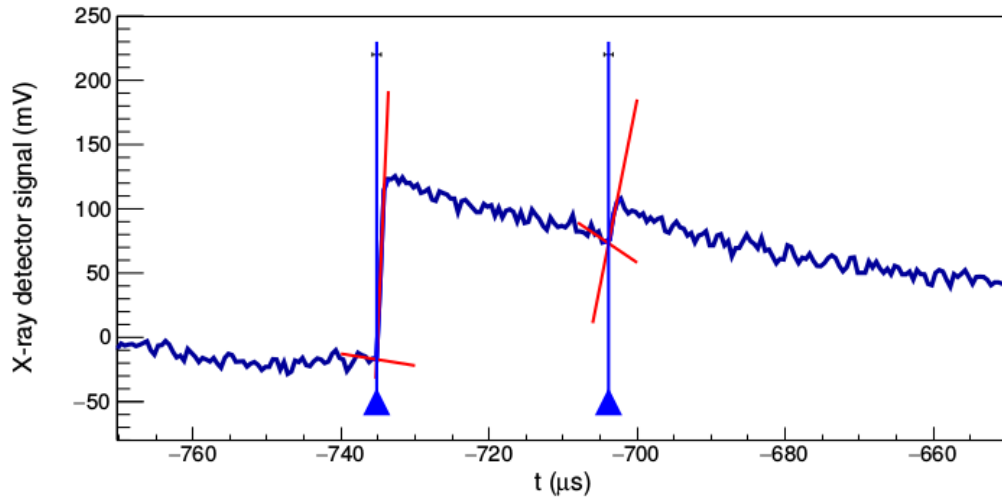


Figure A.1: Illustration of the algorithm to detect t_0 . Red lines are the linear interpolations, blue lines and triangles represent t_0 , the tiny error bars represent the uncertainty $\pm 0.5\mu s$.

More specifically, the algorithm can be divided into three phases:

1. the first phase acts like a trigger, the rising between two consecutive samples is evaluated and if it is larger than a certain threshold ($\approx 50keV$) the algorithm identifies a possible high-energy pulse-
2. In the second phase 12 samples (4 before and 8 later) are evaluated and a monotonic trend ($y_0 > y_1 > y_2 > \dots$) is searched.

3. If at least 2 monotonic steps are found the algorithm computes a linear interpolation of the 4 samples before the beginning of the monotonic trend (y_0). The intersection between the two lines gives the t_0 .

The algorithm provides an objective method to estimate the t_0 , without requiring a human-measurement of the t_0 in the $\approx 90\%$ of the cases. When the algorithm fails the t_0 evaluation providing unreliable values, the third phase is executed under human-supervision. Therefore the choice of the samples for the linear interpolation is executed by the human operator.

A.3 Imaging efficiency

It is well known that lightning VHF location systems can easily mislocate or entirely skip locating VHF sources. In this section, we tried to illustrate the different cases and quantify the imaging efficiency of our instruments in particular in the lightning events examined in sections 3.2-4.

The first consideration, the imaging efficiency of the interferometer it is not a constant value, it depends on many factors such as: the signal-to-noise ratio (SNR), the rate of the VHF impulses and the geometry of the flashes. Therefore the imaging efficiency is different for each lightning event and it changes during the evolution of the flash. If two or more VHF sources emit simultaneously (or in less time than the length of the window chosen for the processing), it is possible to identify at least three possible cases that reduce the imaging efficiency of the interferometer: 1) Both VHF sources are skipped, 2) Both VHF sources are mislocated, 3) One VHF source is well located, but the weaker source is missed.

In Figure 2, we show how it is possible to realize and quantify cases 1) and 2) instead is much more difficult to evaluate 3). The black spline shows the amplitude of all the VHF sources A_s reconstructed by the interferometer, while A^{CH2} is the amplitude of the central antenna (channel 2). The VHF source average amplitude A_s is defined as the cluster average amplitude of all the windows that provides a compatible location of the VHF sources.

$$\begin{aligned}
 A_s &= \frac{1}{n_{cl}} \sum_{j=0}^{n_{cl}} \langle A_j \rangle & \langle A_j \rangle &= \sum_{i=0}^{128} \frac{W(i)}{3} \left(|A_i^{CH1}| + |A_i^{CH2}| + |A_i^{CH3}| \right) \\
 t_s &= \frac{1}{n_{cl}} \sum_{j=0}^{n_{cl}} t_j (i = 64)
 \end{aligned} \tag{A.3.1}$$

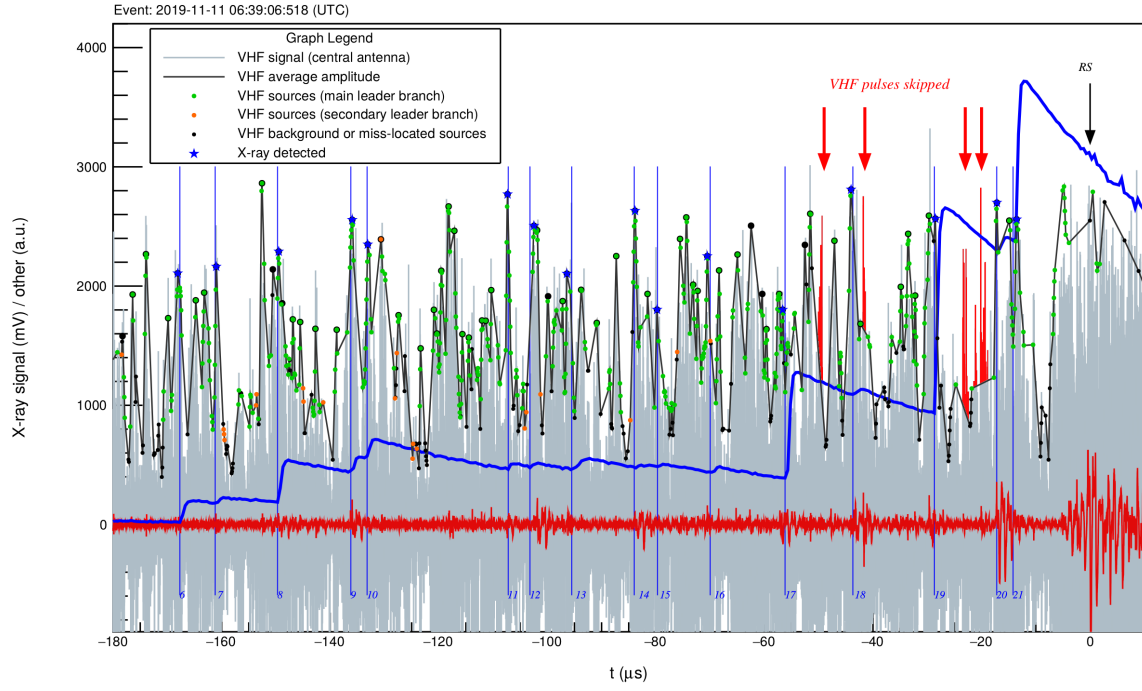


Figure A.2: Graphical evaluation of imaging efficiency. The range selected is particularly relevant for the high-energy emissions analysis. Black spline shows the VHF average amplitude provided by the interferometer, the green and orange sources belong to the lightning leader imaging the black sources are mislocated or due to the noise (case 2), the red VHF pulses are the entirely skipped VHF sources (case 1). Blue stars are the VHF sources associated with the X-ray pulses.

Similarly, the time of the VHF source is the cluster average time calculated at the half of the window ($i=64$) and $W(i)$ is the Hamming window function. Comparing the VHF signal (i.e. of the central antenna) A^{CH2} with the VHF average amplitude A_s of the sources reconstructed by the interferometer it is possible to evaluate when the algorithm entirely skip one or more VHF sources (see in Figure 2, red VHF pulses case 1). It is not easy to quantify exactly how many VHF sources (clusters) are skipped, but it is not difficult to compute how many windows are not reconstructed and this value is about the 1.7% in the last 3 ms of event 2019-11-11 06:39:06 and the about 3.2% in the last 3 ms of event 2019-11-11 06:38:16.

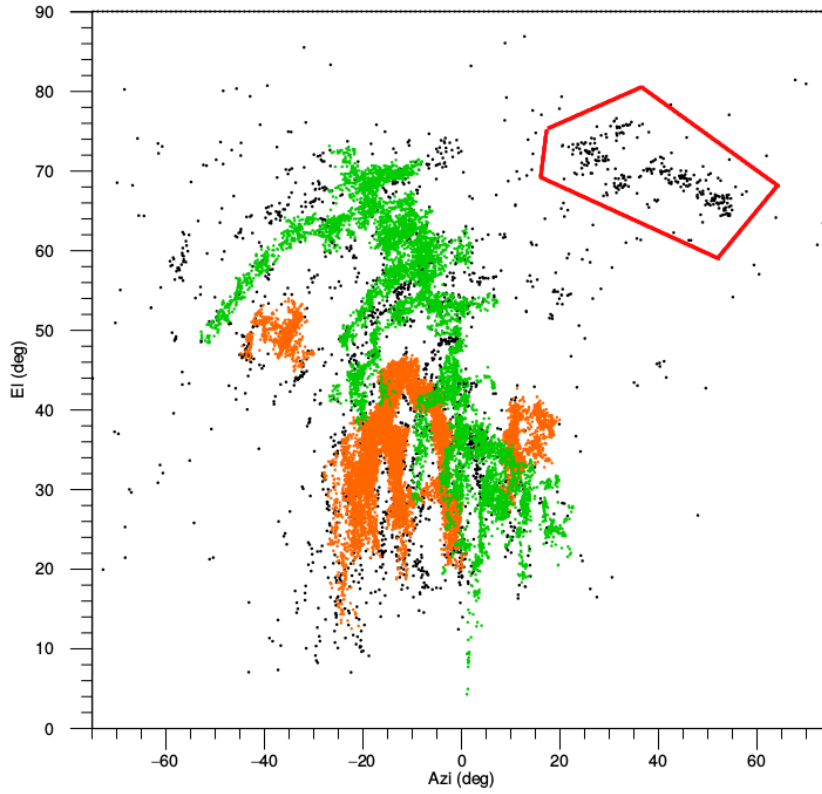


Figure A.3: Graphical evaluation of imaging efficiency. The green and orange sources belong to the lightning leader imaging the black sources are mislocated or due to the noise (case 2). The noise is the 17% of the VHF sources but it is overestimated due to the leader branch in the red box.

Regarding case 2, it is possible to map all the VHF sources and use the noise-reduction techniques (i.e Stock et al. 2014) to identify the mislocated sources. (See Figure 3)

In the last 3 ms of the event 2019-11-11 06:39:06 the noise is the $< 17\%$ of the VHF sources but it is overestimated due to the leader branch in the red box, and in the last 3 ms of the event 2019-11-11 06:38:16 the noise is $< 19\%$ of the VHF sources.

It is more difficult to evaluate case 3), because the cross-correlation algorithm (of our INTF, with 3 antennas) always chooses the dominant VHF pulse, therefore if there are weaker VHF sources they are ignored.

In conclusion, it is possible to evaluate directly from the data the imaging efficiency of the interferometer considering cases 1) and 2) and verified if the high-energy emission can be associated with one of these missing or mislocated VHF sources. In general, it is not possible to exclude case 3), but there are no reasons to think that the high-energy emissions are always associated with weaker VHF sources not detected, actually our data clearly shows the opposite (see section 3).

A.4 Temporal correspondence between high-energy emissions and most intense VHF pulses

In this section, we present the evidence of a temporal correspondence between high-energy emissions and the most intense VHF pulses. We compare the time-of-arrival of the high-energy emissions t_0 , computed by the algorithm described in section 2.2, and the time-of-arrival of the VHF sources, computed by the INTF (equations A.3.1). In particular, we consider a subset of the VHF sources that we call “most intense VHF pulses”. We defined this subset considering a local maximum condition and a threshold condition on the amplitude.

In general, the VHF sources detected by a broadband lightning interferometer can be due to continuously radiating or impulsive events (Stock et al. 2014). The local maximum condition favors the selection of impulsive events, in particular those that are clearly impulsive and of greater magnitude.

An absolute measurement of the VHF amplitude (or power, intensity, energy) is particularly challenging because required a dual-polarization omnidirectional antenna and the 3D location of the VHF source. Not having this information, the analysis performed is based on relative measurements of VHF amplitude (for this reason those are indicated in arbitrary units a.u.).

The VHF amplitude depends on many factors besides the intrinsic intensity of the emission, in particular, by the distance and by the direction with respect to the antenna. For this reason, to compare similar features on VHF pulses amplitude, we adopted a statistical approach. We compute 20-quantiles in every time-window of $200\mu s$ and we define “most intense VHF pulses” those pulses with the local maximum

condition and amplitude greater than the third quartile (top 25%) or more generally, greater than the median (top 50%). This procedure has the great advantage to provide a solid definition of “most intense VHF pulses” and can be used to compare different amplitude values in function of time of the same lightning event or different events.

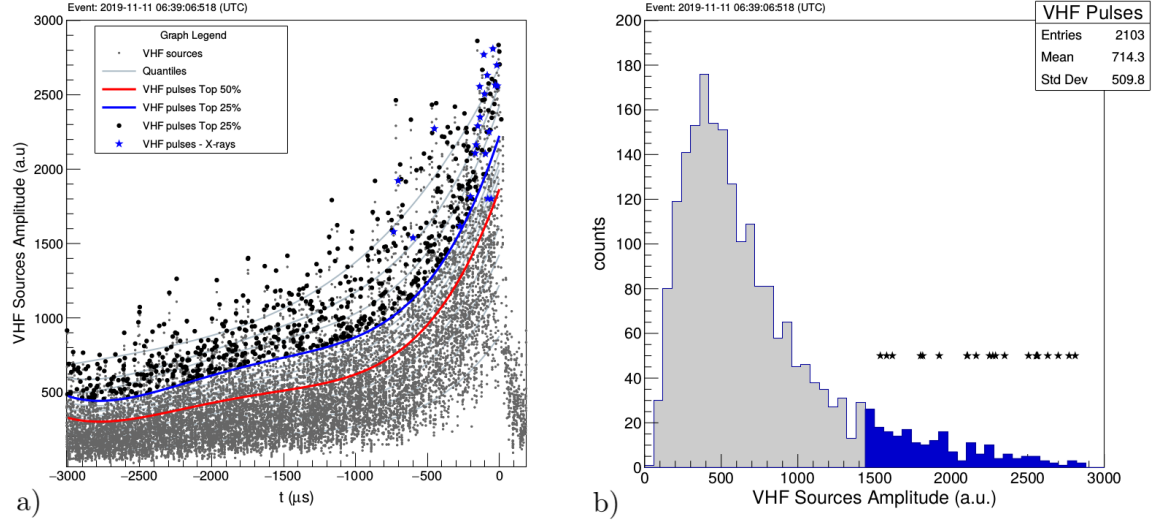


Figure A.4: a) VHF sources and pulses in function of time and a graphical evaluation of the quantiles. The red line is the median (top 50%), blue line corresponds to the top 25% blue stars are the VHF pulses associated with the X-rays emissions. b) VHF pulse distribution of the last 3 ms before the RS, black stars are the VHF pulses associated with the X-rays emissions.

Figure A.4.a) shows an example of this procedure, the red line is the median and the blue line corresponds to the amplitude threshold for the top 25% VHF pulses. Figure A.4.b) shows the pulse distribution of the last 3 ms before the RS, although it clearly reveals the correspondence with high amplitude pulses, the amplitude threshold definition is not robust and changes a lot between different events and the range of time considered.

After these definitions and terminology clarification, we investigate the temporal relation between X-ray pulses detected and the VHF pulses, in particular, the most intense. In order to show this correspondence, we computed a discrete cross-correlation between the time-of-arrival of the VHF pulses and the time-of-arrival of the X-ray emissions t_0 considering an uncertainty of $\pm 0.5\mu s$ (width of t_0). Assuming a good synchronization of the signals, if there is correspondence a peak in zero is expected compatible with the uncertainty range $\pm 0.5\mu s$. Figure A.5 a) shows the cross-correlation peak in zero considering all the VHF pulses in the last 3 ms. The correlation peak

in zero is pretty clear and it is the highest peak. Despite that, there are other peaks due to random association, caused by the high density of VHF pulses. It is possible to separate the contribute in the cross-correlation, computing separately the cross-correlation between the most intense VHF pulses with the rest of the pulses (see Figure A.5 b)).

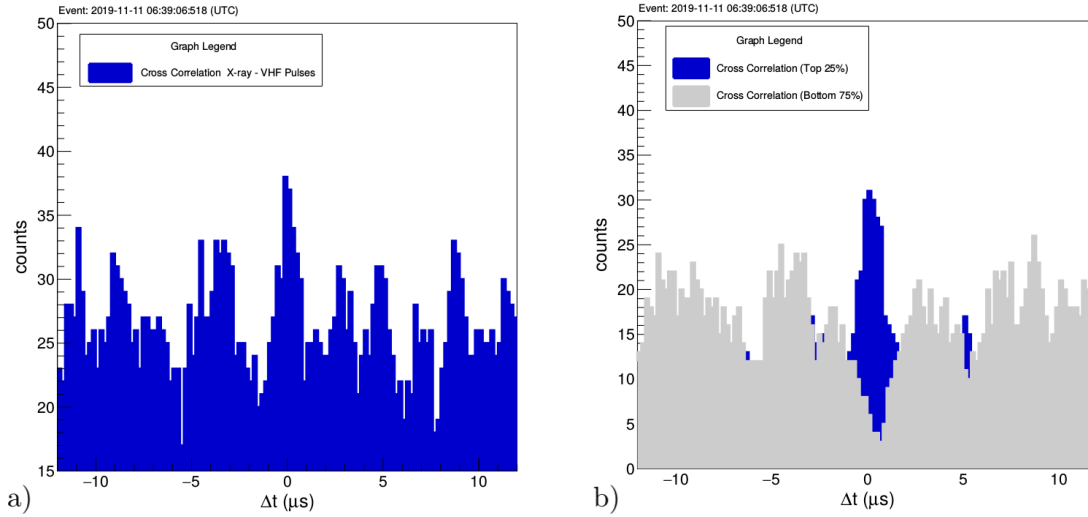


Figure A.5: a) Cross-correlation between VHF pulses and X-ray t_0 considering an uncertainty on t_0 of $\pm 0.5 \mu s$. b) Cross-correlation between the most intense VHF pulses (top 25%) and X-ray t_0 (in blue) and cross-correlation between the less intense VHF pulses (bottom 75%) and X-ray t_0 (in gray) in both cases considering an uncertainty on t_0 of $\pm 0.5 \mu s$.

In conclusion it is possible to state that, in this event, the VHF pulses and the X-ray emissions are temporally cross-correlated and specifically the more intense VHF pulses are correlated, while the lower amplitude VHF emissions seem not to be correlated.

In order to prove that this correlation is not due to a random association, we tried to quantify the p-value in a selected range of the most interesting event with multiple association. In the last $180 \mu s$ of event 2019-11-11 06:39:06 sixteen correspondences between the X-ray emissions time-of-arrival t_0 and the most intense VHF pulses (top 50%), of which fourteen in the top 25% were observed. Figure A.6 a) shows the range of interest and the correspondences. To evaluate the p-value a Monte Carlo simulation was performed on these data to evaluate the probability to have a random association in the uncertainty range ($\pm 0.5 \mu s$). The probability to have one random association is actually quite high $p(k = 1, |\Delta t| < 0.5 \mu s) = 0.366$, but the chance to

have multiple random association decrease rapidly.

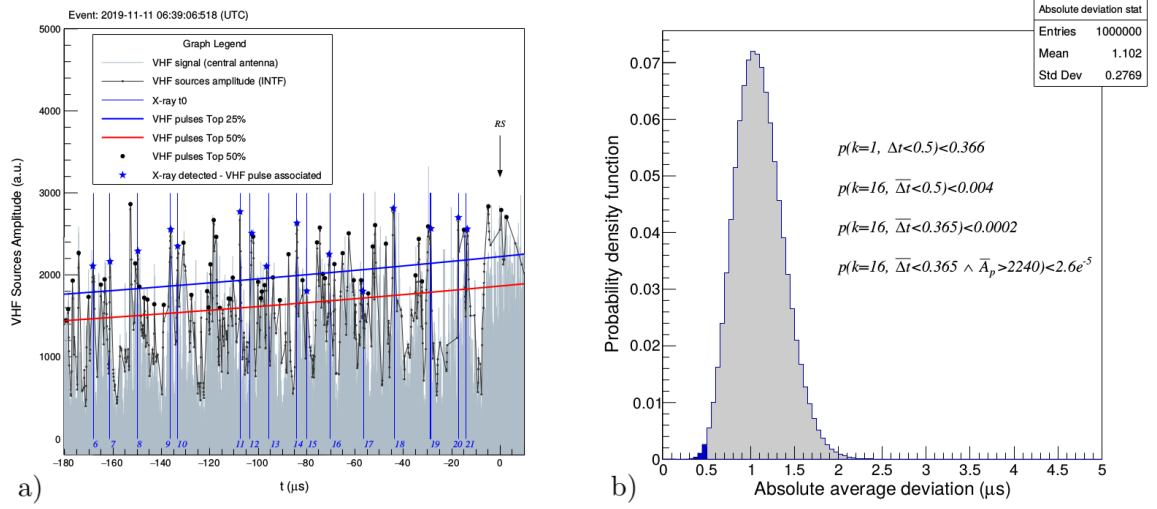


Figure A.6: a) Zoom of the most interesting temporal range of event 2019-11-11 06:39:06. In the last 180 μs , sixteen X-rays pulses can be associated with the most intense VHF pulses (Top 50%) with an average absolute deviation of $\bar{\Delta t} < 0.365 \mu s$. b) Probability density function obtained from a Monte Carlo simulation to evaluate the p-value of the case of study presented in a).

Considering sixteen correspondences the absolute average deviation $\bar{\Delta t}$ can be calculated. The probability density function is shown in Figure A.6 b). The probability for a random correspondence in the uncertainty range is less than 0.4% but the p-value of our event is lower than 0.02% and if we consider the amplitude as well, the probability to have a random association with overall higher VHF amplitude is absolutely low ($p < 2.6 \times 10^{-6}$). We have shown the results for the top 50% definition of VHF pulses, but the results for the top 25% are even better, lower p-values. Therefore, in this event, the correspondence between the most intense VHF pulses and X-ray t0 is statistically significant.

This correspondence between X-ray t0 and the most VHF pulses has been observed in all five of the most intense X-ray burst events.

Finally, in Figure A.7 we have reported the distribution of two relevant quantity related to this temporal correspondence computed for the event 2019-11-11 06:39:06 and all the other X-ray bursts. The time difference $\Delta_t = t_0 - t_{VHF}$ between the X-ray t0 and the VHF pulses associated. This quantity is useful to evaluate the goodness of the temporal correspondence. It is relevant to note that the mean value of the

distribution is compatible with zero and the standard deviation is compatible with our instrumental uncertainty (see Figure A.7.a).

Despite the definition of “most intense VHF pulses” provided is generally clear, we studied more in deep the relation with the VHF amplitude. As previously mentioned, we computed the 20-quantiles in all the X-ray bursts observed in order to compare the relative magnitude of the VHF amplitude of the associated pulses. The overall distribution is shown in Figure A.7.b), the top 50% correspond to more than 96% of the distribution and the top 25% correspond to the 82%.

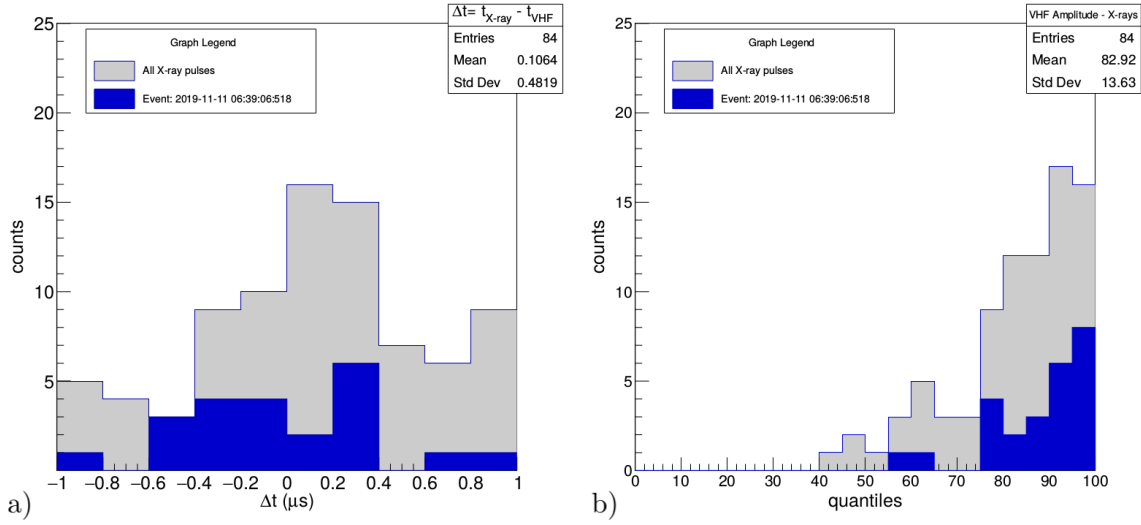


Figure A.7: a) Time difference between the X-ray t_0 and the VHF pulses associated. This quantity was evaluated in all X-ray bursts (gray) and in the X-ray burst 2019-11-11 06:39:06 (blue). b) Distribution of the VHF pulses associated with X-ray emissions. The VHF amplitude is expressed in quantiles to allow comparison between different events.

Finally, in Figure A.7 we have reported the distribution of two relevant quantity related to this temporal correspondence computed for the event 2019-11-11 06:39:06 and for all the other X-ray bursts. The time difference $\Delta t = t_0 - t_{\text{VHF}}$ between the X-ray t_0 and the VHF pulses associated. This quantity is useful to evaluate the goodness of the temporal correspondence. It is relevant to note that the mean value of the distribution is compatible with zero and the standard deviation is compatible with our instrumental uncertainty (see Figure A.7.a).

Despite the definition of “most intense VHF pulses” provided is generally clear, we studied more in deep the relation with the VHF amplitude. As previously mentioned, we computed the 20-quantiles in all the X-ray bursts observed to compare the relative

magnitude of the VHF amplitude of the associated pulses. The overall distribution is shown in Figure A.7.b), the top 50% correspond to more than 96% of the distribution and the top 25% corresponds to the 82%.

A.5 X-ray and gamma-ray spectrum

Figure A.8 shows the X-ray and gamma-ray energy spectrum in fair weather and during thunderstorms. The increase in the gamma activity is basically due to the decay products (^{214}Pb and ^{214}Bi) of the Radon ^{222}Rn related to the rainfall (e.g. Fabró et al., 2016).

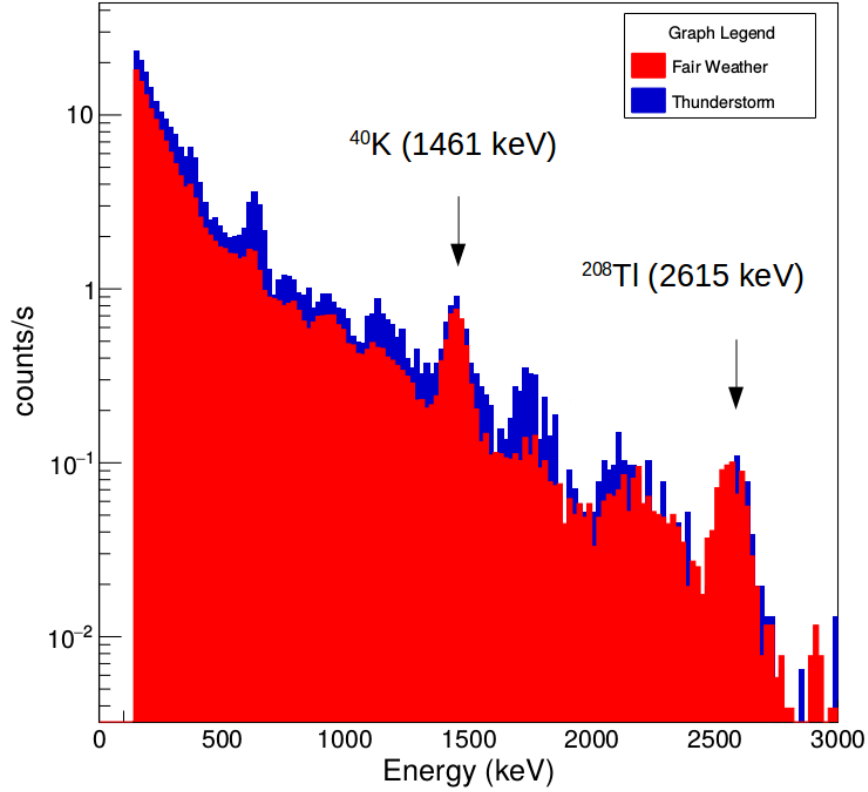


Figure A.8: High-energy spectrum of our NaI(Tl) detector. The figure show the background X-ray and gamma-ray energy spectrum in fair weather and during thunderstorms. (Data from our campaign in Colombia in 2019)

B. Urbani et al (2022): Supporting Information

Supporting Information

1. Charge structure
2. Angular resolution of the VHF broadband interferometer
3. DPL spatial and temporal origin in flash 2019-10-27 11:15:06 (UTC)
4. Spectral power density of the two DPLs
5. Analysis of the first downward positive leader propagation in VHF radio band
6. Quasi-3D conversion
7. Initiation of the second DPL along a previous channel to ground, flash (1)

Additional Supporting Information (Files uploaded separately)

1. Animation S1

Introduction

This Supporting Information document provides additional details requested by reviewers and complementary material useful for other scientists working in the field.

B.1 Charge structure

We reconstructed the thunderstorm evolution and the charge structure in proximity of the events (1) and (2). Figure B.1a shows the flashes recorded by the LMA that intersect the area of interest shown in Figure B.1b. It can be seen that such events take place in the initial dissipation phase of the storm, where usually +CG strokes occur (e.g., Rakov et al. 2003). The multipanel below Figure B.1a shows the charge distribution in a 20 minutes window around the events observed. The technique used to reconstruct the charge structure and the total flash rate is based on the LMA data (e.g., San Segundo et al. (2020), Lopez et al. (2019) and the identification of positive and negative leaders (e.g., Rust et al. 2005, Stock et al. 2014, Lopez et al. 2019).

It is possible to recognize a normal polarity storm, with the upper positive charge region (red) between 6-9 km altitude and a midlevel negative charge region (blue) between 3-6 km altitude. In Figures S1b and S1c it is possible to observe a compact and active cell with a vertical development in proximity of both the flash initiation and the DPL origin. In Figure B.1c, it is indicated that the DPL initiates from the lower altitude location of an intra-cloud negative leader channel in the quasi-neutral region. A similar scenario was observed also in the event (1), although less clearly.

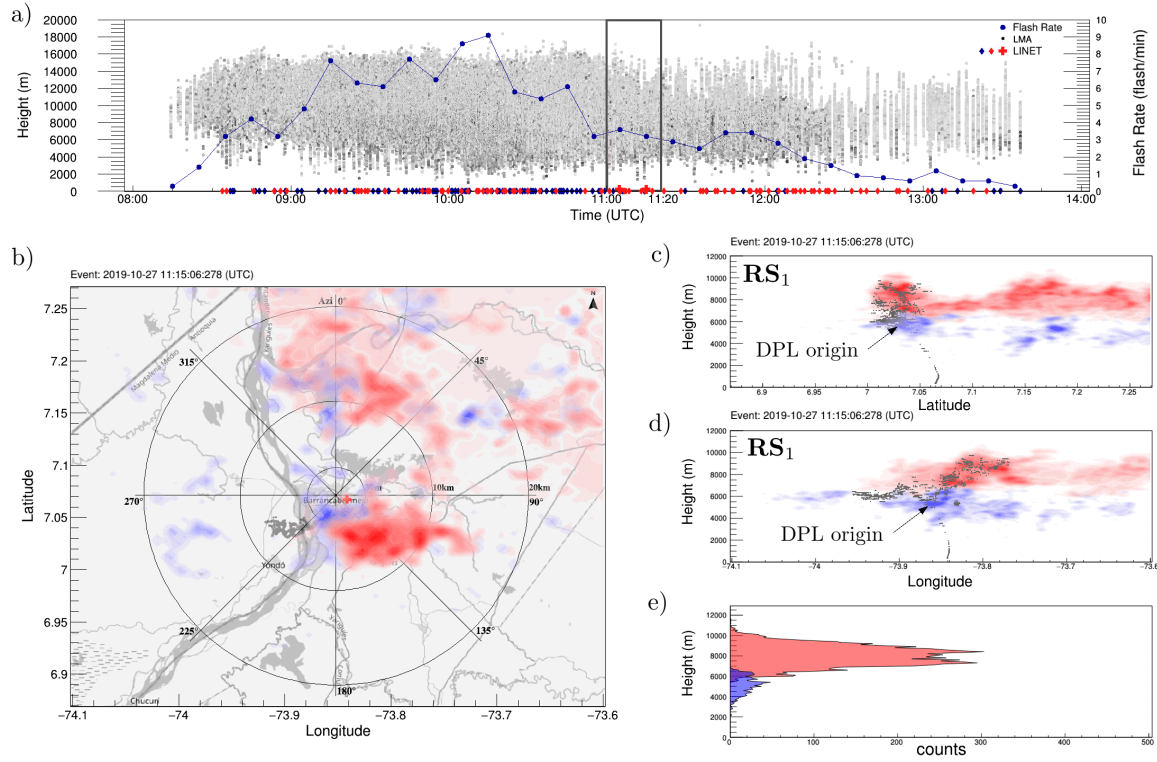


Figure B.1: a) Temporal development of the thunderstorm to which belongs observations of flash 2019-10-27 11:05:10 and flash 2019-10-27 11:15:06. The scatter plot are the VHF sources recorded by the LMA in the area of interest, the total flash rate and the LINET detections of CG strokes are superimposed. The multipanel below (b,c,d,e) shows the charge structure reconstructed by the LMA data in the area of interest, in a temporal range of 20 minutes around the events observed. The positively charged region is colored red and the negatively charged region blue.

B.2 Angular resolution of the VHF broadband interferometer

The VHF broadband interferometer provides a 2D mapping of the VHF sources. The two angular coordinates (elevation and azimuth) are evaluated in its system of reference centered in the central antenna (7.070718, -73.851537). The angular resolution of the VHF broadband interferometer is thoroughly discussed in Stock 2014 (section 4.1) and Tilles et al. 2019. It is function of the elevation angle (El) and it depends essentially by the timing uncertainty σ_τ of the interferometer and how it changes according to the signal-to-noise (SNR) ratio (Stock 2014, equations 4.4 and 4.5).

$$\sigma_{Az} = \frac{c}{d} \frac{1}{\cos(El)} \sigma_\tau \quad \sigma_{El} = \frac{c}{d} \frac{1}{\sin(El)} \sigma_\tau$$

To evaluate the σ_τ of our interferometer we calculate the standard deviation of the closure delay $\tau_{123} = \tau_{12} + \tau_{23} - \tau_{13}$ (Stock 2014, equation 2.9), specifically during the flash (2) reported in the manuscript (Figure B.2a). Using the approximated error propagation formula: $\sigma_{\tau_{123}}^2 \approx \sigma_{\tau_{12}}^2 + \sigma_{\tau_{23}}^2 + \sigma_{\tau_{13}}^2$ we obtain an estimation of timing uncertainty:

$$\sigma_\tau \approx \frac{\sigma_{\tau_{123}}}{\sqrt{3}} = 0.07 \text{ ns}$$

This estimation of σ_τ is consistent with what we expect, timing uncertainty around 0.1 ns are typical in VHF interferometer measurements (Stock 2014). Using this value we calculate the theoretical angular resolution (Figure B.2b) during flash (2).

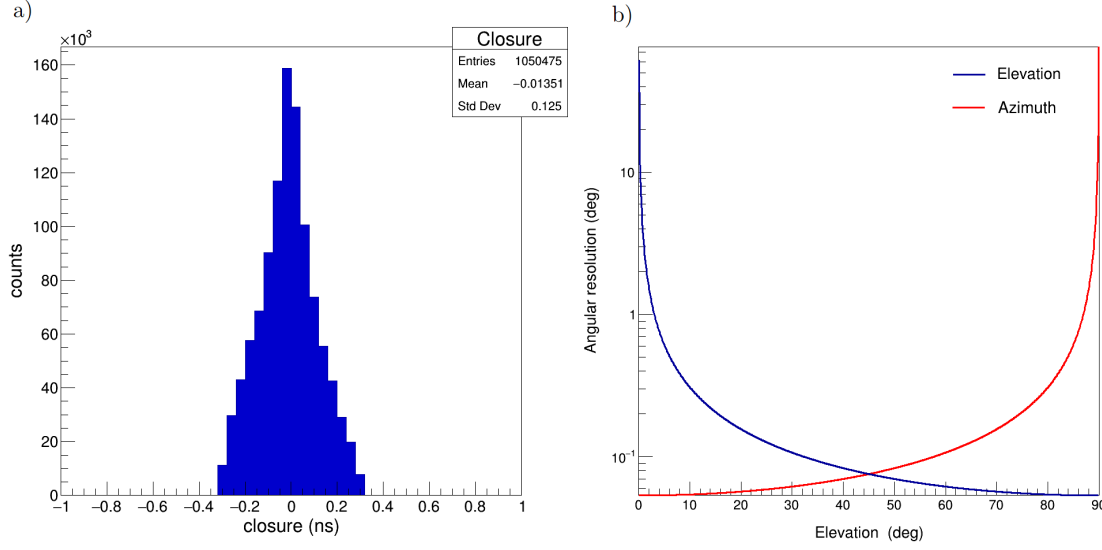


Figure B.2: a) Closure delay during flash 2019-10-27 11:15:06 (UTC), the closure standard deviation is $\sigma_{\tau_{123}} = 0.125$ ns. b) Angular resolution of our interferometer during flash 2019-10-27 11:15:06 (UTC).

B.3 First DPL spatial and temporal origin in flash 2019-10-27 11:15:06 (UTC)

In this section, we provide further details on the spatial and temporal origin of the DPL in flash (2): 2019-10-27 11:15:06 (UTC). According to our best interpretation of the data, the DPL does not seem to originate by the typical bidirectional leader development after the flash initiation, but from the negative horizontal channel in its lowest altitude location (Figure B.3a).

To interpret the lightning processes and evolution correctly, we need to focus in particular on the INTF data because they have the maximum resolution (compared with the LMA) and the minimum amount of mislocated sources and numerical artifacts (compared with the Quasi-3D data). Figure B.3b and Figure B.3c show the INTF data needed to identify the DPL origin. Thanks to the second DPL, which is brighter in VHF radio band (Figure 3, Figure B.4a), it is possible to deduce a first hypothesis on the origin of the first DPL in the elevation-azimuth plane. Then using this first hypothesis as a reference, it is possible to identify in the time domain a weak group of VHF sources that could correspond to the first DPL origin (Figure B.3c). A further clue that seems to support this evidence is the VHF activity detected in that location in the $150\text{--}250\text{ }\mu\text{s}$ after both return strokes.

It is relevant to note in Figure B.3b a recoil leader (RL) retracing a decayed negative

leader simultaneously with the emerging of the DPL. We think that the RL and DPL processes could be related. The RL could have triggered or induced the emergence of the DPL or be evidence of a disconnected channel. This supports the hypothesis that in this flash the DPL is emerging from a negative horizontal channel, a scenario known and reported in literature (e.g., Krehbiel 1981, Saba et al. 2009, Nag & Rakov 2012, Wu et al. 2020 Yuan et al. 2020).

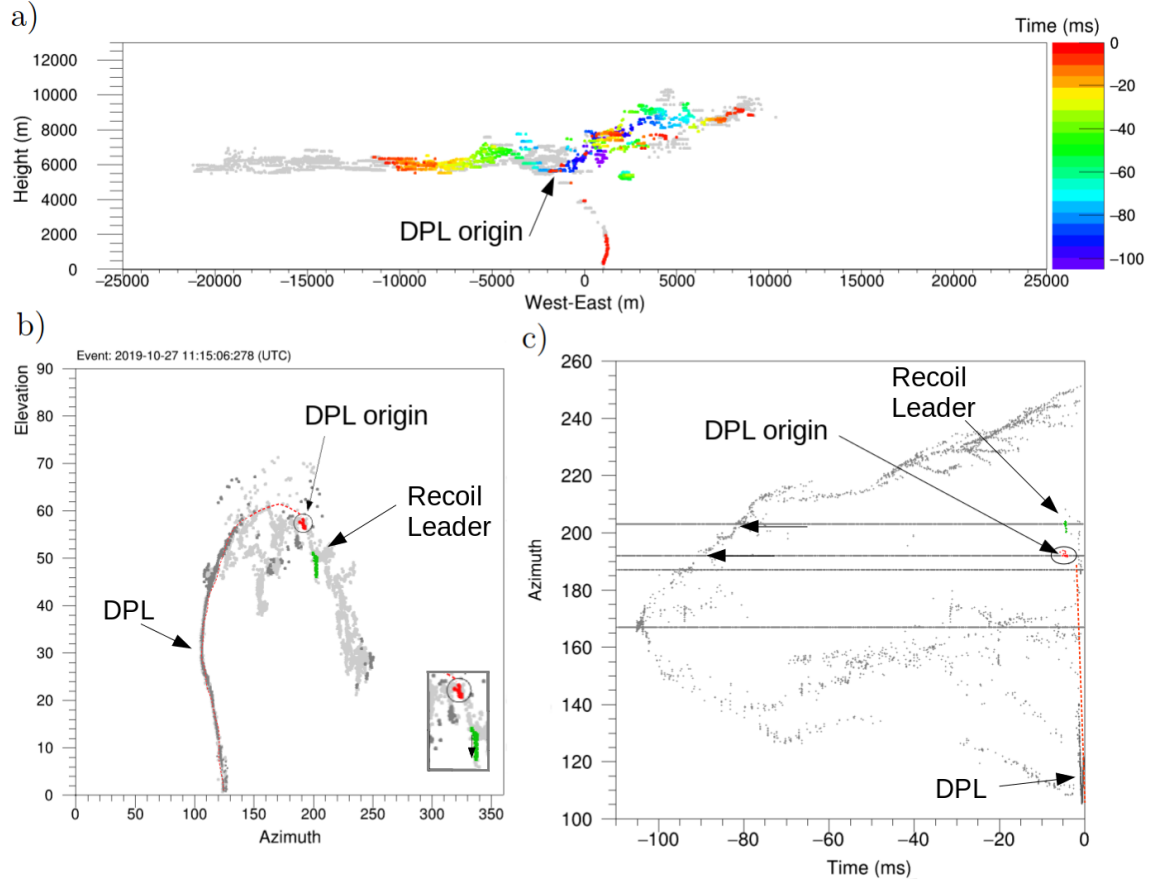


Figure B.3: a) DPL spatial origin along the horizontal negative channel, Quasi-3D data. b) Elevation-azimuth map and c) Azimuth-time map of the beginning of the flash. The DPL origin and a RL are highlighted in red and green respectively.

B.4 Spectral power density of the two DPLs

Figure B.4 shows the spectral power density of the two DPLs of the Multi-stroke +CG flash along the same channel, event: 2019-10-27 11:15:06 (UTC) and for comparison the spectral power density of an intra-cloud negative leader belonging to the same flash. The absolute scale was not calibrated and not normalized neither in time or distance, especially with the negative leader. It is possible to note that DPL_2 is brighter than DPL_1 in the VHF radioband especially at higher frequencies. The power drop below 20 MHz and above 80 MHz is due to the band-pass filters of the interferometer.

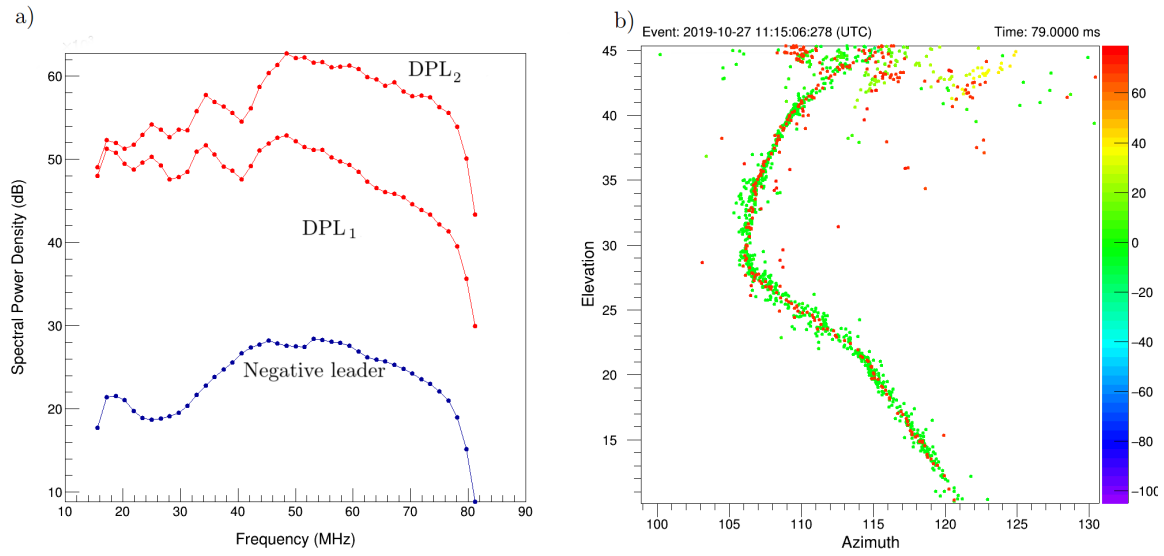


Figure B.4: a) Spectral power density of the two DPLs and an intra-cloud negative leader. N.B. The power spectral density is not normalized between different lightning leader spectra. b) Elevation-azimuth map of the two DPLs. it is possible to appreciate the high angular resolution especially in the azimuth angle.

B.5 Analysis of the first downward positive leader propagation in VHF radio band

The VHF broadband interferometer has a very high temporal resolution, which combined with short range observations (within a few kilometers) allows one the detail study of the DPL temporal and spatial propagation. As anticipated, Figure 4a shows a clearly intermittent VHF pattern. To highlight this pattern we first defined a function (red line) that integrates the absolute value of the VHF waveform in a range of $\pm 10 \mu s$. This function is like an envelope, in which the local maxima of the magnitude identify the bursts of VHF pulses (blue dots). Then using this function as a reference, we manually selected burst by burst and highlighted them in dark gray (see Figure 4a).

In order to study the DPL propagation, we selected a time interval of about $100 \mu s$ (see Figure 4a and Figure B.5a) and mapped its propagation (Figure B.5b). To better describe the propagation we chose to color in an alternate way a burst of VHF pulses (blue) and its subsequent burst (red), the inter-bursts VHF pulses were colored in light gray. Figure B.5a and Figure B.5b show the interval selected and in particular, five bursts of VHF pulses labeled with Latin numbers (I,II,III,IV,V). It is possible to note that although the temporal propagation is clearly intermittent the spatial propagation is quite smooth. There is generally an overlap between the VHF pulses of two subsequent bursts (see e.g., III and IV). This superposition can be seen clearly in Figure B.5d in the right histogram panel, which shows the distribution in elevation of all the VHF pulses belonging to a burst and its subsequent burst. Another two comments can be made about Figure B.5b, the temporal dispersion of the subsequent burst is not relevant; it is just a statistical effect due to the different time elapsed between bursts. The higher fluctuation of the inter-burst pulses is probably due to their lower amplitude (our processing technique usually provides a better accuracy for stronger VHF pulses).

Figure B.5c shows a scatter plot of time residual and elevation residuals. It can be seen that the most intense VHF pulses are usually in the middle of the burst. The linear fit suggests that there is a propagation inside the burst with an average of around -0.56 degrees in elevation per $10 \mu s$.

Finally, we provide an overall temporal analysis of the intermittent bursts of VHF pulses. Figure 4e shows the distribution of the time elapsed between bursts which is about $10\text{-}20 \mu s$ and the burst duration is about $5\text{-}15 \mu s$. A new interesting observation is shown in Figure B.5f, the frequency of the bursts of VHF pulses seems increasing approaching ground of about a factor 2, this observation is verified in the event (1) as well. This new finding, if confirmed in further observations, could be another relevant

aspect to describe the DPL propagation and maybe provide a deeper understanding of this intermittent behavior. Our observations in the VHF band are consistent with previous studies, which report a typical intermittent fast electric field changes in the last 0.5-1.0 ms before the first return stroke (Kong et al. 2008, Wang et al. 2011, Schumann et al. 2013, Saba et al. 2015, Johari et al. 2016). We believe that the VHF bursts we observed and these fast electric field changes are closely related. It was hypothesized that the origin of these impulses could be due to solely the upward negative leader, but although we do not exclude that similar pulses can be also produced by negative upward leaders (Saba et 2015), the data presented in this work and recently by Pu et al. 2021 confirm that such intermittent emissions are typical of the DPL and originates from the streamers activity on the positive leader tip.

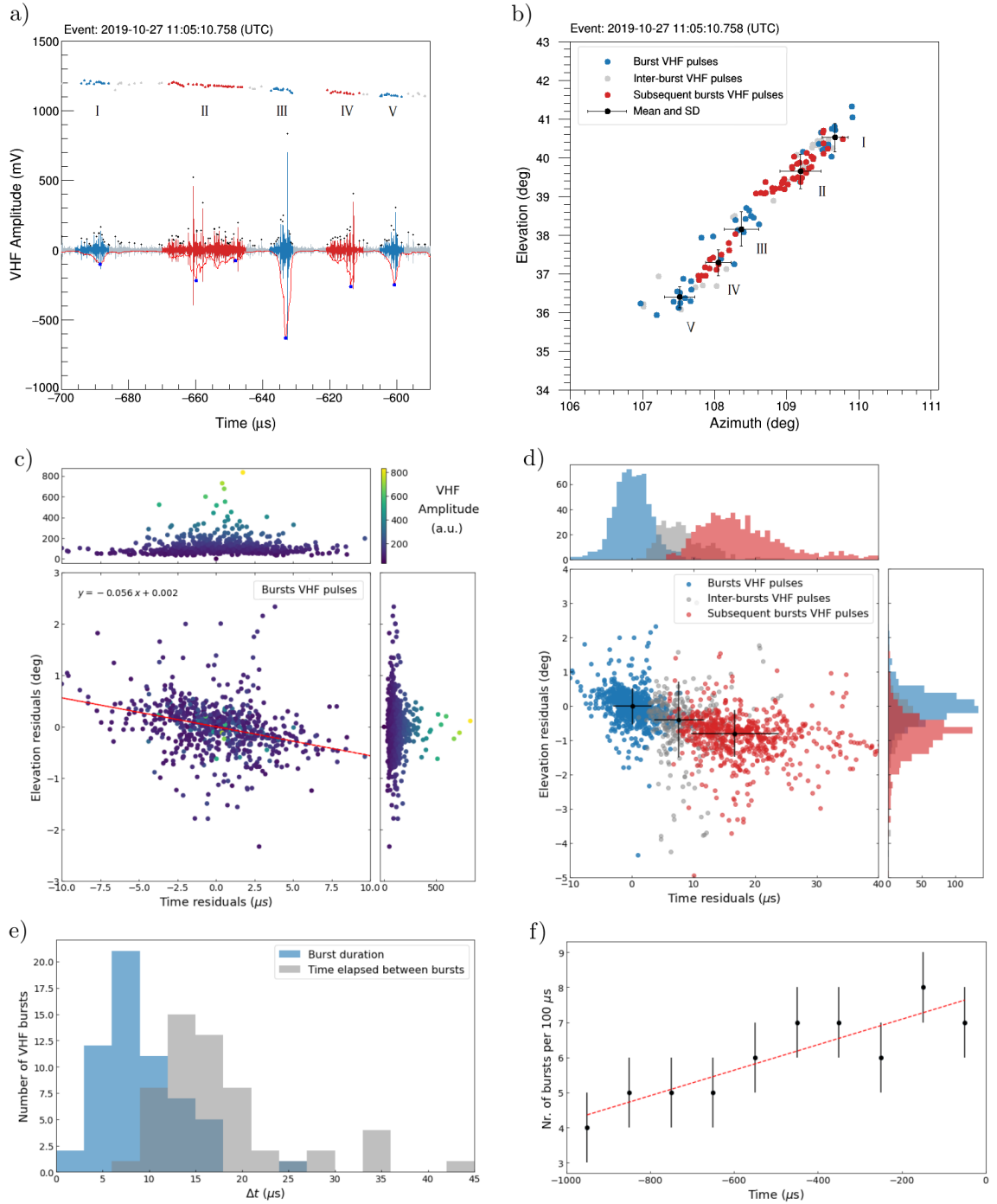


Figure B.5: Analysis of the propagation of the downward positive leader (DPL) in virgin air, the data belong to first +CG stroke of the event: 2019-10-27 11:15:06 (UTC). a) Selected range of Figure 3a. We colored alternately a first VHF burst in blue and the subsequent in red. Inter-burst pulses are colored in gray. b) Elevation-azimuth map of the VHF sources located by the INTF, same data of the left panel. c) Scatter plot of the burst VHF pulses in the last 1 ms before the return stroke (RS). The figure shows the VHF amplitude in function of the time and elevation residuals with respect to the mean burst value. d) Scatter plot of the VHF pulses in the last 1 ms before the RS. e) Burst time duration and time elapsed between two subsequent bursts. f) Frequency of the bursts, trend of the number of bursts per 100 microseconds in the last 1 ms before the RS.

B.6 Quasi-3D conversion

The post-processing technique called “Quasi-3D conversion” was introduced and described by Stock (2014). It consists of an interpolation technique in a few steps: first, the projection of the LMA data on the system of reference of the interferometer; second, a raw approximation of the 3D projection is made for each INTF source by interpolating in the elevation-azimuth plane the projected LMA sources; finally, an iterative procedure using alternately the spatial correlation and successive projections allows an estimation of the radial distance of individual INTF sources.

Figure B.6 shows the superposition of the LMA sources over the INTF data (Figure B.6a and Figure B.6c) and the Quasi-3D imaging (Figure B.6b). A noise reduction technique was applied considering both sets of data (LMA and INTF). The LMA noise can affect the goodness of the Quasi-3D conversion introducing image artifacts.

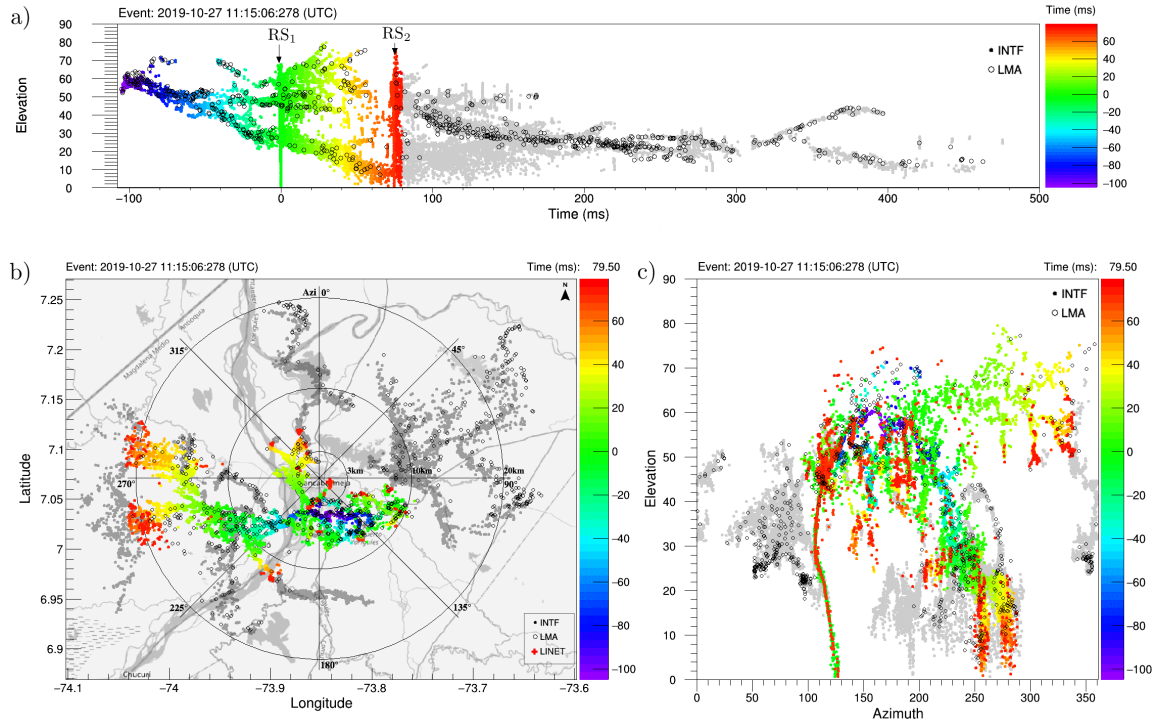


Figure B.6: Multi-stroke +CG flash along the same channel, event: 2019-10-27 11:15:06 (UTC). Quasi-3D conversion of the INTF data and superposition of the LMA sources.

B.7 Initiation of the second DPL along a previous channel to ground, flash (1)

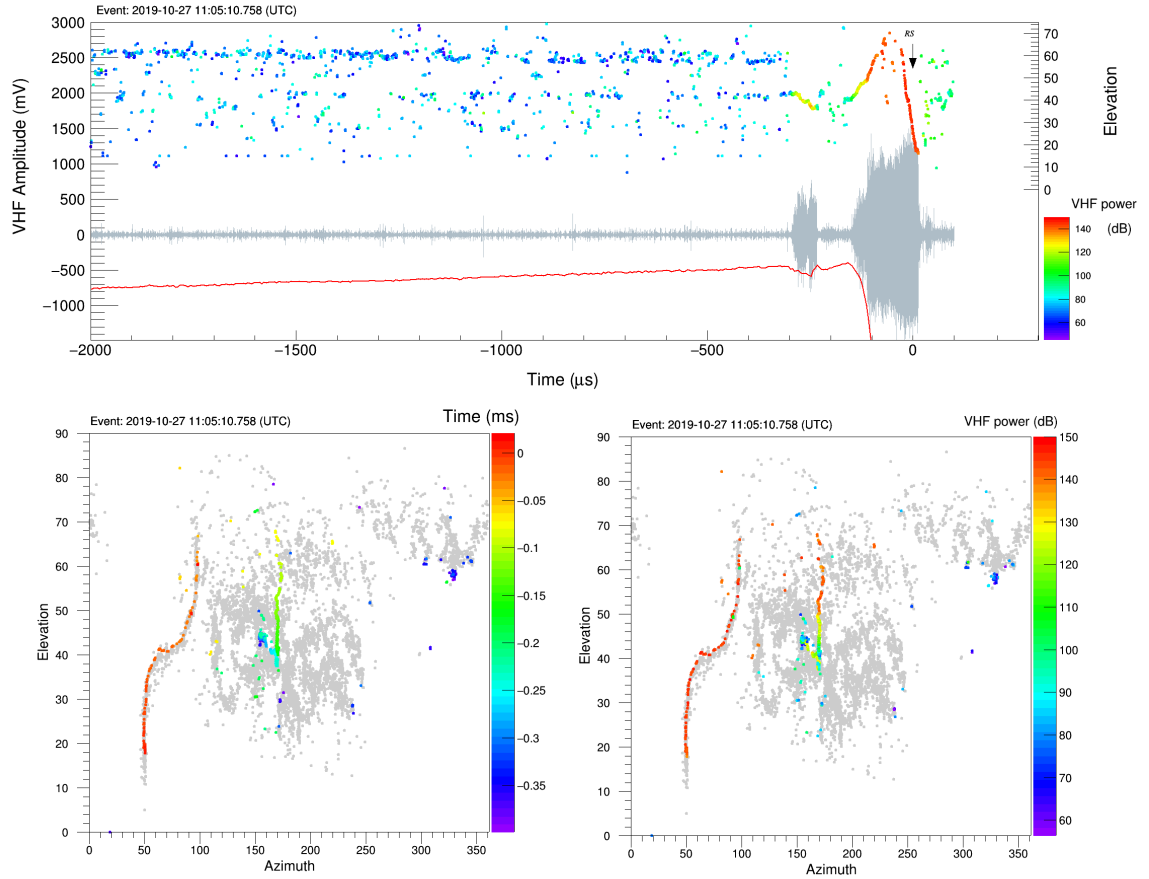


Figure B.7: Initiation of the second DPL along a previous channel to ground, multi-stroke +CG flash along the same channel, event: 2019-10-27 11:05:10 (UTC). Overview of the last 4 ms before RS2. Time-elevation plot of the VHF sources mapped by the INTF. Electric field waveform (red line) recorded by the flat plate antenna and VHF waveform (gray line).

Additional Supporting Information (Files uploaded separately)

Animation S1 shows the multi-stroke +CG flash along the same channel 2019-10-27 11:15:06 (UTC). The real time frame rate is 2kHz. The time evolution of the animation is slowed by a factor of 200 compared to the real time flash development. Animation S1 is described in section 3 of the manuscript.

Bibliography

Abbasi, R., Abe, M., Abu-Zayyad, T., Allen, M., Anderson, R., Azuma, R., ... others (2017). The bursts of high energy events observed by the telescope array surface detector. *Physics Letters A*, 381(32), 2565–2572.

Abbasi, R., Abu-Zayyad, T., Allen, M., Barcikowski, E., Belz, J., Bergman, D., ... others (2018). Gamma ray showers observed at ground level in coincidence with downward lightning leaders. *Journal of Geophysical Research: Atmospheres*, 123(13), 6864–6879.

Abbasi, R., Belz, J., Le Von, R., Rodeheffer, D., Krehbiel, P., Remington, J., & Rison, W. (2019). Ground-based observations of terrestrial gamma ray flashes associated with downward-directed lightning leaders. In *Epj web of conferences* (Vol. 197, p. 03002).

Arabshahi, S., Dwyer, J., Cramer, E., Grove, J., Gwon, C., Hill, J., ... others (2015). The energy spectrum of x-rays from rocket-triggered lightning. *Journal of Geophysical Research: Atmospheres*, 120(20), 10–951.

Aranguren, D., González, J., Cruz, A., Inampué, J., Torres, H., & Pérez-Tobón, P. S. (2017). Lightning strikes on power transmission lines and lightning detection in colombia. In *2017 international symposium on lightning protection (xiv sipda)* (pp. 273–278).

Becerra, M., Long, M., Schulz, W., & Thottappillil, R. (2018). On the estimation of the lightning incidence to offshore wind farms. *Electric power systems research*, 157, 211–226.

Belz, J., Krehbiel, P., Remington, J., Stanley, M., Abbasi, R., LeVon, R., ... others (2020). Observations of the origin of downward terrestrial gamma-ray flashes. *Journal of Geophysical Research: Atmospheres*, 125(23), e2019JD031940.

- Berge, N., & Celestin, S. (2019). Constraining downward terrestrial gamma ray flashes using ground-based particle detector arrays. *Geophysical Research Letters*, *46*(14), 8424–8430.
- Betz, H. D., Schmidt, K., Laroche, P., Blanchet, P., Oettinger, W. P., Defer, E., . . . Konarski, J. (2009). Linet—an international lightning detection network in europe. *Atmospheric Research*, *91*(2-4), 564–573.
- Blouin, K. D., Flannigan, M. D., Wang, X., & Kochtubajda, B. (2016). Ensemble lightning prediction models for the province of alberta, canada. *International journal of wildland fire*, *25*(4), 421–432.
- Boccippio, D. J., Williams, E. R., Heckman, S. J., Lyons, W. A., Baker, I. T., & Boldi, R. (1995). Sprites, elf transients, and positive ground strokes. *Science*, *269*(5227), 1088–1091.
- Bolic, M., Drndarevic, V., & Gueaieb, W. (2009). Pileup correction algorithms for very-high-count-rate gamma-ray spectrometry with nai (tl) detectors. *IEEE Transactions on Instrumentation and Measurement*, *59*(1), 122–130.
- Briggs, M., Fishman, G., Connaughton, V., Bhat, P., Paciesas, W., Preece, R., . . . others (2010). First results on terrestrial gamma ray flashes from the fermi gamma-ray burst monitor. *Journal of Geophysical Research: Space Physics*, *115*(A7).
- Carlson, B., Lehtinen, N. G., & Inan, U. S. (2009). Terrestrial gamma ray flash production by lightning current pulses. *Journal of Geophysical Research: Space Physics*, *114*(A12).
- Celestin, S., & Pasko, V. P. (2011). Energy and fluxes of thermal runaway electrons produced by exponential growth of streamers during the stepping of lightning leaders and in transient luminous events. *Journal of Geophysical Research: Space Physics*, *116*(A3).
- Celestin, S., & Pasko, V. P. (2012). Compton scattering effects on the duration of terrestrial gamma-ray flashes. *Geophysical Research Letters*, *39*(2).
- Celestin, S., Xu, W., & Pasko, V. P. (2015). Variability in fluence and spectrum of high-energy photon bursts produced by lightning leaders. *Journal of Geophysical Research: Space Physics*, *120*(12), 10–712.
- Chanrion, O., & Neubert, T. (2010). Production of runaway electrons by negative streamer discharges. *Journal of Geophysical Research: Space Physics*, *115*(A6).

- Chilingarian, A., Daryan, A., Arakelyan, K., Hovhannisyan, A., Mailyan, B., Melkumyan, L., ... Vanyan, L. (2010). Ground-based observations of thunderstorm-correlated fluxes of high-energy electrons, gamma rays, and neutrons. *Physical Review D*, 82(4), 043009.
- Chmielewski, V., Blair, J., Kennedy, D., MacGorman, D., & Calhoun, K. (2022). A comparison of processing methods for the oklahoma lightning mapping array. *Earth and Space Science*, 9(7), e2021EA002081.
- Cummer, S. A., Lyu, F., Briggs, M. S., Fitzpatrick, G., Roberts, O. J., & Dwyer, J. R. (2015). Lightning leader altitude progression in terrestrial gamma-ray flashes. *Geophysical Research Letters*, 42(18), 7792–7798.
- Cummer, S. A., Zhai, Y., Hu, W., Smith, D. M., Lopez, L. I., & Stanley, M. A. (2005). Measurements and implications of the relationship between lightning and terrestrial gamma ray flashes. *Geophysical Research Letters*, 32(8).
- Dwyer, J. R. (2003). A fundamental limit on electric fields in air. *Geophysical Research Letters*, 30(20).
- Dwyer, J. R. (2004). Implications of x-ray emission from lightning. *Geophysical Research Letters*, 31(12).
- Dwyer, J. R. (2008). Source mechanisms of terrestrial gamma-ray flashes. *Journal of Geophysical Research: Atmospheres*, 113(D10).
- Dwyer, J. R. (2020). Modeling terrestrial gamma-ray flashes observed by asim. *EGU General Assembly 2020, Online*(EGU2020-19320).
- Dwyer, J. R., & Cummer, S. A. (2013). Radio emissions from terrestrial gamma-ray flashes. *Journal of Geophysical Research: Space Physics*, 118(6), 3769–3790.
- Dwyer, J. R., Rassoul, H., Al-Dayeh, M., Caraway, L., Wright, B., Chrest, A., ... others (2004). A ground level gamma-ray burst observed in association with rocket-triggered lightning. *Geophysical Research Letters*, 31(5).
- Dwyer, J. R., Rassoul, H. K., Al-Dayeh, M., Caraway, L., Chrest, A., Wright, B., ... others (2005). X-ray bursts associated with leader steps in cloud-to-ground lightning. *Geophysical Research Letters*, 32(1).
- Dwyer, J. R., Schaal, M., Cramer, E., Arabshahi, S., Liu, N., Rassoul, H., ... Uman, M. (2012). Observation of a gamma-ray flash at ground level in association with a cloud-to-ground lightning return stroke. *Journal of Geophysical Research: Space Physics*, 117(A10).

- Dwyer, J. R., & Smith, D. M. (2005). A comparison between monte carlo simulations of runaway breakdown and terrestrial gamma-ray flash observations. *Geophysical Research Letters*, 32(22).
- Dwyer, J. R., Smith, D. M., & Cummer, S. A. (2012). High-energy atmospheric physics: Terrestrial gamma-ray flashes and related phenomena. *Space Science Reviews*, 173(1-4), 133–196.
- Dwyer, J. R., & Uman, M. A. (2014). The physics of lightning. *Physics Reports*, 534(4), 147–241.
- Dwyer, J. R., Uman, M. A., Rassoul, H. K., Al-Dayeh, M., Caraway, L., Jerauld, J., ... others (2003). Energetic radiation produced during rocket-triggered lightning. *Science*, 299(5607), 694–697.
- Fabró, F., Montanya, J., Pineda, N., Argemí, O., van der Velde, O. A., Romero, D., & Soula, S. (2016). Analysis of energetic radiation associated with thunderstorms in the ebro delta region in spain. *Journal of Geophysical Research: Atmospheres*, 121(16), 9879–9891.
- Fishman, G. J., Bhat, P., Mallozzi, R., Horack, J., Koshut, T., Kouveliotou, C., ... others (1994). Discovery of intense gamma-ray flashes of atmospheric origin. *Science*, 264(5163), 1313–1316.
- Fleenor, S. A., Biagi, C. J., Cummins, K. L., Krider, E. P., & Shao, X.-M. (2009). Characteristics of cloud-to-ground lightning in warm-season thunderstorms in the central great plains. *Atmospheric Research*, 91(2-4), 333–352.
- Fuquay, D., Taylor, A., Hawe, R., & Schmid Jr, C. (1972). Lightning discharges that caused forest fires. *Journal of Geophysical Research*, 77(12), 2156–2158.
- Gurevich, A., Milikh, G., & Roussel-Dupre, R. (1992). Runaway electron mechanism of air breakdown and preconditioning during a thunderstorm. *Physics Letters A*, 165(5-6), 463–468.
- Gurevich, A., Zybin, K., & Medvedev, Y. V. (2007). Runaway breakdown in strong electric field as a source of terrestrial gamma flashes and gamma bursts in lightning leader steps. *Physics Letters A*, 361(1-2), 119–125.
- Hare, B. M., Scholten, O., Dwyer, J., Ebert, U., Nijdam, S., Bonardi, A., ... Winchen, T. (2020, Mar). Radio emission reveals inner meter-scale structure of negative lightning leader steps. *Phys. Rev. Lett.*, 124, 105101. Retrieved from <https://link.aps.org/doi/10.1103/PhysRevLett.124.105101>
doi: 10.1103/PhysRevLett.124.105101

Hare, B. M., Uman, M., Dwyer, J., Jordan, D., Biggerstaff, M., Caicedo, J., ... others (2016). Ground-level observation of a terrestrial gamma ray flash initiated by a triggered lightning. *Journal of Geophysical Research: Atmospheres*, 121(11), 6511–6533.

Hayenga, C. O. (1984). Characteristics of lightning vhf radiation near the time of return strokes. *Journal of Geophysical Research: Atmospheres*, 89(D1), 1403–1410.

Hettiarachchi, P., Cooray, V., Diendorfer, G., Pichler, H., Dwyer, J., & Rahman, M. (2018). X-ray observations at gaisberg tower. *Atmosphere*, 9(1), 20.

Hill, J. D. (2012). *The mechanisms of lightning leader propagation and ground attachment*. University of Florida.

Howard, J., Uman, M. A., Biagi, C., Hill, D., Jerauld, J., Rakov, V. A., ... Rassoul, H. (2010). Rf and x-ray source locations during the lightning attachment process. *Journal of Geophysical Research: Atmospheres*, 115(D6).

Howard, J., Uman, M. A., Dwyer, J. R., Hill, D., Biagi, C., Saleh, Z., ... Rassoul, H. K. (2008). Co-location of lightning leader x-ray and electric field change sources. *Geophysical Research Letters*, 35(13).

Hubbell, J. H., & Seltzer, S. M. (1995). *Tables of x-ray mass attenuation coefficients and mass energy-absorption coefficients 1 kev to 20 mev for elements z= 1 to 92 and 48 additional substances of dosimetric interest* (Tech. Rep.). National Inst. of Standards and Technology-PL, Gaithersburg, MD (United doi: <https://dx.doi.org/10.18434/T4D01F>

Kawasaki, Z., Mardiana, R., & Ushio, T. (2000). Broadband and narrowband rf interferometers for lightning observations. *Geophysical research letters*, 27(19), 3189–3192.

Kochkin, P., van Deursen, A., Marisaldi, M., Ursi, A., de Boer, A., Bardet, M., ... Østgaard, N. (2017). In-flight observation of gamma ray glows by ildas. *Journal of Geophysical Research: Atmospheres*, 122(23), 12–801.

Kochkin, P., van Deursen, A. P., & Ebert, U. (2014). Experimental study on hard x-rays emitted from metre-scale negative discharges in air. *Journal of Physics D: Applied Physics*, 48(2), 025205.

Krehbiel, P. R. (1981). An analysis of the electric field change produced by lightning. *Ph.D. Thesis*.

- Lapierre, J. L., Sonnenfeld, R. G., Stock, M., Krehbiel, P. R., Edens, H. E., & Jensen, D. (2017). Expanding on the relationship between continuing current and in-cloud leader growth. *Journal of Geophysical Research: Atmospheres*, 122(8), 4150–4164.
- Li, S., Qiu, S., Shi, L., & Li, Y. (2020). Broadband vhf observations of two natural positive cloud-to-ground lightning flashes. *Geophysical Research Letters*, 47(11), e2019GL086915.
- López, J. A., Montanyà, J., van der Velde, O., Romero, D., Aranguren, D., Torres, H., ... Martínez, J. (2016). First data of the colombia lightning mapping array—colma. In *2016 33rd international conference on lightning protection (iclp)* (pp. 1–5).
- López, J. A., Montanyà, J., van der Velde, O. A., Pineda, N., Salvador, A., Romero, D., ... Taborda, J. (2019). Charge structure of two tropical thunderstorms in colombia. *Journal of Geophysical Research: Atmospheres*, 124(10), 5503–5515.
- Lyu, F., Cummer, S. A., Krehbiel, P. R., Rison, W., Briggs, M. S., Cramer, E., ... Stanbro, M. (2018). Very high frequency radio emissions associated with the production of terrestrial gamma-ray flashes. *Geophysical Research Letters*, 45(4), 2097–2105.
- Lyu, F., Cummer, S. A., Lu, G., Zhou, X., & Weinert, J. (2016). Imaging lightning intracloud initial stepped leaders by low-frequency interferometric lightning mapping array. *Geophysical Research Letters*, 43(10), 5516–5523.
- Lyu, F., Cummer, S. A., Solanki, R., Weinert, J., McTague, L., Katko, A., ... Wang, W. (2014). A low-frequency near-field interferometric-toa 3-d lightning mapping array. *Geophysical Research Letters*, 41(22), 7777–7784.
- Maiorana, C., Marisaldi, M., Lindanger, A., Østgaard, N., Ursi, A., Sarria, D., ... others (2020). The 3rd agile terrestrial gamma-ray flashes catalog. part ii: Optimized selection criteria and characteristics of the new sample. *Journal of Geophysical Research: Atmospheres*.
- Mallick, S., Rakov, V., & Dwyer, J. R. (2012). A study of x-ray emissions from thunderstorms with emphasis on subsequent strokes in natural lightning. *Journal of Geophysical Research: Atmospheres*, 117(D16).
- Marisaldi, M., Fuschino, F., Labanti, C., Galli, M., Longo, F., Del Monte, E., ... others (2010). Detection of terrestrial gamma ray flashes up to 40 mev by the agile satellite. *Journal of Geophysical Research: Space Physics*, 115(A3).

- Marisaldi, M., Fuschino, F., Tavani, M., Dietrich, S., Price, C., Galli, M., . . . others (2014). Properties of terrestrial gamma ray flashes detected by agile mcal below 30 mev. *Journal of Geophysical Research: Space Physics*, 119(2), 1337–1355.
- Mazur, V. (2002). Physical processes during development of lightning flashes. *Comptes Rendus Physique*, 3(10), 1393–1409.
- Meegan, C., Lichti, G., Bhat, P., Bissaldi, E., Briggs, M. S., Connaughton, V., . . . others (2009). The fermi gamma-ray burst monitor. *The Astrophysical Journal*, 702(1), 791.
- Montanyà, J., Fabró, F., March, V., van der Velde, O., Solà, G., Romero, D., & Argemí, O. (2015). X-rays and microwave rf power from high voltage laboratory sparks. *Journal of Atmospheric and Solar-Terrestrial Physics*, 136, 94–97.
- Montanyà, J., Fabró, F., van der Velde, O., Romero, D., Solà, G., Hermoso, J. R., . . . Pineda, N. (2014). Registration of x-rays at 2500 m altitude in association with lightning flashes and thunderstorms. *Journal of Geophysical Research: Atmospheres*, 119(3), 1492–1503.
- Montanyà, J., Van Der Velde, O., & Williams, E. R. (2014). Lightning discharges produced by wind turbines. *Journal of Geophysical Research: Atmospheres*, 119(3), 1455–1462.
- Montanyà, J., Van der Velde, O. A., March, V., Romero, D., Solà, G., & Pineda, N. (2012). High-speed video of lightning and x-ray pulses during the 2009–2010 observation campaigns in northeastern spain. *Atmospheric research*, 117, 91–98.
- Moore, C. B., Eack, K. B., Aulich, G. D., & Rison, W. (2001). Energetic radiation associated with lightning stepped-leaders. *Geophysical Research Letters*, 28(11), 2141–2144.
- Moss, G. D., Pasko, V. P., Liu, N., & Veronis, G. (2006). Monte carlo model for analysis of thermal runaway electrons in streamer tips in transient luminous events and streamer zones of lightning leaders. *Journal of Geophysical Research: Space Physics*, 111(A2).
- Nag, A., & Rakov, V. A. (2012). Positive lightning: An overview, new observations, and inferences. *Journal of Geophysical Research: Atmospheres*, 117(D8).
- Nemiroff, R. J., Bonnell, J. T., & Norris, J. P. (1997). Temporal and spectral characteristics of terrestrial gamma flashes. *Journal of Geophysical Research: Space Physics*, 102(A5), 9659–9665.

- Neubert, T., Østgaard, N., Reglero, V., Chanrion, O., Heumesser, M., Dimitriadou, K., ... others (2020). A terrestrial gamma-ray flash and ionospheric ultraviolet emissions powered by lightning. *Science*, 367(6474), 183–186.
- Østgaard, N., Gjesteland, T., Hansen, R., Collier, A., & Carlson, B. (2012). The true fluence distribution of terrestrial gamma flashes at satellite altitude. *Journal of Geophysical Research: Space Physics*, 117(A3).
- Østgaard, N., Gjesteland, T., Stadsnes, J., Connell, P., & Carlson, B. (2008). Production altitude and time delays of the terrestrial gamma flashes: Revisiting the burst and transient source experiment spectra. *Journal of Geophysical Research: Space Physics*, 113(A2).
- Østgaard, N., Neubert, T., Reglero, V., Ullaland, K., Yang, S., Genov, G., ... others (2019). First 10 months of tgf observations by asim. *Journal of Geophysical Research: Atmospheres*, 124(24), 14024–14036.
- Proctor, D. E., Uytendogaardt, R., & Meredith, B. M. (1988). Vhf radio pictures of lightning flashes to ground. *Journal of Geophysical Research: Atmospheres*, 93(D10), 12683–12727.
- Pu, Y., Cummer, S. A., & Liu, N. (2021). Vhf radio spectrum of a positive leader and implications for electric fields. *Geophysical Research Letters*, 48(11), e2021GL093145.
- Rakov, V. A., & Kereszy, I. (2022). Ground-based observations of lightning-related x-ray/gamma-ray emissions in florida: Occurrence context and new insights. *Electric Power Systems Research*, 213, 108736.
- Rakov, V. A., & Uman, M. A. (2003). *Lightning: physics and effects*. Cambridge university press.
- Rhodes, C., Shao, X.-M., Krehbiel, P., Thomas, R., & Hayenga, C. (1994). Observations of lightning phenomena using radio interferometry. *Journal of Geophysical Research: Atmospheres*, 99(D6), 13059–13082.
- Richard, P., Delannoy, A., Labaune, G., & Laroche, P. (1986). Results of spatial and temporal characterization of the vhf-uhf radiation of lightning. *Journal of Geophysical Research: Atmospheres*, 91(D1), 1248–1260.
- Rison, W., Thomas, R. J., Krehbiel, P. R., Hamlin, T., & Harlin, J. (1999). A gps-based three-dimensional lightning mapping system: Initial observations in central new mexico. *Geophysical research letters*, 26(23), 3573–3576.

- Saba, M., Ferro, M., Cuadros, E., Custódio, D., Nag, A., Schumann, C., ... others (2019). High-speed video observation of a dart leader producing x-rays. *Journal of Geophysical Research: Space Physics*.
- Saba, M. M., Campos, L. Z., Krider, E. P., & Pinto Jr, O. (2009). High-speed video observations of positive ground flashes produced by intracloud lightning. *Geophysical research letters*, 36(12).
- Saba, M. M., Schulz, W., Warner, T. A., Campos, L. Z., Schumann, C., Krider, E. P., ... Orville, R. E. (2010). High-speed video observations of positive lightning flashes to ground. *Journal of Geophysical Research: Atmospheres*, 115(D24).
- Saleh, Z., Dwyer, J. R., Howard, J., Uman, M., Bakhtiari, M., Concha, D., ... Rassoul, H. (2009). Properties of the x-ray emission from rocket-triggered lightning as measured by the thunderstorm energetic radiation array (tera). *Journal of Geophysical Research: Atmospheres*, 114(D17).
- Schaal, M., Dwyer, J. R., Rassoul, H. K., Hill, J. D., Jordan, D. M., & Uman, M. A. (2013). The angular distribution of energetic electron and x-ray emissions from triggered lightning leaders. *Journal of Geophysical Research: Atmospheres*, 118(20), 11–712.
- Shao, X., & Krehbiel, P. (1996). The spatial and temporal development of intracloud lightning. *Journal of Geophysical Research: Atmospheres*, 101(D21), 26641–26668.
- Shao, X.-M., Hamlin, T., & Smith, D. M. (2010). A closer examination of terrestrial gamma-ray flash-related lightning processes. *Journal of Geophysical Research: Space Physics*, 115(A6).
- Skeie, C., Østgaard, N., Lehtinen, N., Sarria, D., Kochkin, P., de Boer, A., ... Flourens, F. (2020). Constraints on recoil leader properties estimated from x-ray emissions in aircraft-triggered discharges. *Journal of Geophysical Research: Atmospheres*, 125(14), e2019JD032151.
- Skeltved, A. B., Østgaard, N., Carlson, B., Gjesteland, T., & Celestin, S. (2014). Modeling the relativistic runaway electron avalanche and the feedback mechanism with geant4. *Journal of Geophysical Research: Space Physics*, 119(11), 9174–9191.
- Smith, D., Bowers, G., Kamogawa, M., Wang, D., Ushio, T., Ortberg, J., ... Stock, M. (2018). Characterizing upward lightning with and without a terrestrial gamma ray flash. *Journal of Geophysical Research: Atmospheres*, 123(20), 11–321.

- Smith, D., Dwyer, J., Hazelton, B., Grefenstette, B., Martinez-McKinney, G., Zhang, Z., ... others (2011). A terrestrial gamma ray flash observed from an aircraft. *Journal of Geophysical Research: Atmospheres*, 116(D20).
- Smith, D. M., Lopez, L. I., Lin, R. P., & Barrington-Leigh, C. P. (2005). Terrestrial gamma-ray flashes observed up to 20 mev. *Science*, 307(5712), 1085–1088.
- Stock, M. (2014). *Broadband interferometry of lightning*. New Mexico Institute of Mining and Technology.
- Stock, M., Akita, M., Krehbiel, P., Rison, W., Edens, H., Kawasaki, Z., & Stanley, M. (2014). Continuous broadband digital interferometry of lightning using a generalized cross-correlation algorithm. *Journal of Geophysical Research: Atmospheres*, 119(6), 3134–3165.
- Sun, Z., Qie, X., Jiang, R., Liu, M., Wu, X., Wang, Z., ... Zhang, H. (2014). Characteristics of a rocket-triggered lightning flash with large stroke number and the associated leader propagation. *Journal of Geophysical Research: Atmospheres*, 119(23), 13–388.
- Tavani, M., Barbiellini, G., Argan, A., Boffelli, F., Bulgarelli, A., Caraveo, P., ... others (2009). The agile mission. *Astronomy & Astrophysics*, 502(3), 995–1013.
- Thomas, R. J., Krehbiel, P. R., Rison, W., Hunyady, S. J., Winn, W. P., Hamlin, T., & Harlin, J. (2004). Accuracy of the lightning mapping array. *Journal of Geophysical Research: Atmospheres*, 109(D14).
- Tiberia, A., Arnone, E., Ursi, A., Fuschino, F., Virgilli, E., Preziosi, E., ... Dietrich, S. (2022). A joint linet and iss-lis view of lightning distribution over the mt. cimone area within the gamma-flash program. *Remote Sensing*, 14(14), 3501.
- Tierney, H. E., Roussel-Dupré, R. A., Symbalisty, E. M., & Beasley, W. H. (2005). Radio frequency emissions from a runaway electron avalanche model compared with intense, transient signals from thunderstorms. *Journal of Geophysical Research: Atmospheres*, 110(D12).
- Tilles, J. N., Liu, N., Stanley, M. A., Krehbiel, P. R., Rison, W., Stock, M. G., ... Wilson, J. (2019). Fast negative breakdown in thunderstorms. *Nature Communications*, 10(1), 1–12.
- Tran, M., Kereszy, I., Rakov, V., & Dwyer, J. (2019). On the role of reduced air density along the lightning leader path to ground in increasing x-ray production relative to normal atmospheric conditions. *Geophysical Research Letters*, 46(15), 9252–9260.

- Tran, M., & Rakov, V. (2017). A study of the ground-attachment process in natural lightning with emphasis on its breakthrough phase. *Scientific reports*, 7(1), 1–13.
- Tran, M., Rakov, V., Mallick, S., Dwyer, J., Nag, A., & Heckman, S. (2015). A terrestrial gamma-ray flash recorded at the lightning observatory in gainesville, florida. *Journal of Atmospheric and Solar-Terrestrial Physics*, 136, 86–93.
- Urbani, M., Montanyà, J., Van der Velde, O., López, J., Arcanjo, M., Fontanes, P., ... Roncancio, J. (2021). High-energy radiation from natural lightning observed in coincidence with a vhf broadband interferometer. *Journal of Geophysical Research: Atmospheres*, 126(7), e2020JD033745.
- Ursi, A., Rodriguez Fernandez, G., Tiberia, A., Virgili, E., Arnone, E., Preziosi, E., ... Tavani, M. (2022). A study on tgf detectability at 2165 m altitude: Estimates for the mountain-based gamma-flash experiment. *Remote Sensing*, 14(13), 3103.
- Ushio, T.-o., Kawasaki, Z.-I., Ohta, Y., & Matsuura, K. (1997). Broad band interferometric measurement of rocket triggered lightning in japan. *Geophysical research letters*, 24(22), 2769–2772.
- van der Velde, O. A., Montanyà, J., Soula, S., Pineda, N., & Mlynarczyk, J. (2014). Bidirectional leader development in sprite-producing positive cloud-to-ground flashes: Origins and characteristics of positive and negative leaders. *Journal of Geophysical Research: Atmospheres*, 119(22), 12-755.
- Von Kienlin, A., Meegan, C. A., Paciesas, W. S., Bhat, P., Bissaldi, E., Briggs, M. S., ... others (2014). The second fermi gbm gamma-ray burst catalog: the first four years. *The Astrophysical Journal Supplement Series*, 211(1), 13.
- Wada, Y., Enoto, T., Nakamura, Y., Furuta, Y., Yuasa, T., Nakazawa, K., ... others (2019). Gamma-ray glow preceding downward terrestrial gamma-ray flash. *Communications Physics*, 2(1), 1–9.
- Warwick, J. W., Hayenga, C. O., & Brosnahan, J. W. (1979). Interferometric directions of lightning sources at 34 mhz. *Journal of Geophysical Research: Oceans*, 84(C5), 2457–2468.
- Williams, E., Boldi, R., Bor, J., Satori, G., Price, C., Greenberg, E., ... others (2006). Lightning flashes conducive to the production and escape of gamma radiation to space. *Journal of Geophysical Research: Atmospheres*, 111(D16).
- Williams, E., Lyons, W., Hobara, Y., Mushtak, V., Asencio, N., Boldi, R., ... others (2010). Ground-based detection of sprites and their parent lightning flashes over

africa during the 2006 amma campaign. *Quarterly Journal of the Royal Meteorological Society*, 136(S1), 257–271.

Wu, T., Wang, D., & Takagi, N. (2020). Multiple-stroke positive cloud-to-ground lightning observed by the falma in winter thunderstorms in japan. *Journal of Geophysical Research: Atmospheres*, 125(20), e2020JD033039.

Yuan, S., Qie, X., Jiang, R., Wang, D., Sun, Z., Srivastava, A., & Williams, E. (2020). Origin of an uncommon multiple-stroke positive cloud-to-ground lightning flash with different terminations. *Journal of Geophysical Research: Atmospheres*, 125(15), e2019JD032098.

Zhu, Y., Bitzer, P., Rakov, V., Stock, M., Lapierre, J., DiGangi, E., ... Lang, T. (2021). Multiple strokes along the same channel to ground in positive lightning produced by a supercell. *Geophysical Research Letters*, 48(23), e2021GL096714.

Acknowledgments